AD_____

Award Number: W81XWH-12-1-0284

TITLE: Development of Targeted Nanobubbles for Ultrasound Imaging and Ablation of Metastatic Prostate Cancer Lesions

PRINCIPAL INVESTIGATOR: Mohamed El-Sayed

CONTRACTING ORGANIZATION: University of Michigan
 Ann Arbor, MI, 48109-2111

REPORT DATE: August 2013

TYPE OF REPORT: Annual

PREPARED FOR: U.S. Army Medical Research and Materiel Command
                         Fort Detrick, Maryland 21702-5012

DISTRIBUTION STATEMENT: Approved for Public Release;
                         Distribution Unlimited

The views, opinions and/or findings contained in this report are those of the author(s) and should not be construed as an official Department of the Army position, policy or decision unless so designated by other documentation.

REPORT DOCUMENTATION PAGE

Form Approved
OMB No. 0704-0188

Public reporting burden for this collection of information is estimated to average 1 hour per response, including the time for reviewing instructions, searching existing data sources, gathering and maintaining the data needed, and completing and reviewing this collection of information. Send comments regarding this burden estimate or any other aspect of this collection of information, including suggestions for reducing this burden to Department of Defense, Washington Headquarters Services, Directorate for Information Operations and Reports (0704-0188), 1215 Jefferson Davis Highway, Suite 1204, Arlington, VA 22202-4302. Respondents should be aware that notwithstanding any other provision of law, no person shall be subject to any penalty for failing to comply with a collection of information if it does not display a currently valid OMB control number. **PLEASE DO NOT RETURN YOUR FORM TO THE ABOVE ADDRESS.**

1. REPORT DATE	2. REPORT TYPE	3. DATES COVERED
August 2013	Annual	15 July 2012 - 14 July 2013

4. TITLE AND SUBTITLE

Development of Targeted Nanobubbles for Ultrasound Imaging and Ablation of Metastatic Prostate Cancer Lesions

5a. CONTRACT NUMBER

5b. GRANT NUMBER
W81XWH-12-1-0284

5c. PROGRAM ELEMENT NUMBER

6. AUTHOR(S)
Mohamed El-Sayed

5d. PROJECT NUMBER

5e. TASK NUMBER

5f. WORK UNIT NUMBER

7. PERFORMING ORGANIZATION NAME(S) AND ADDRESS(ES)
University of Michigan
Ann Arbor, MI, 48109-2111

8. PERFORMING ORGANIZATION REPORT NUMBER

9. SPONSORING / MONITORING AGENCY NAME(S) AND ADDRESS(ES)
U.S. Army Medical Research and Materiel Command
Fort Detrick, Maryland 21702-5012

10. SPONSOR/MONITOR'S ACRONYM(S)

11. SPONSOR/MONITOR'S REPORT NUMBER(S)

12. DISTRIBUTION / AVAILABILITY STATEMENT
Approved for Public Release; Distribution Unlimited

13. SUPPLEMENTARY NOTES

14. ABSTRACT
We report the synthesis of the amphiphilic PEG-b (PAA)-b-P(HDFMA-co-MMA) copolymers that proved to encapsulate 1%-2% v/v PFP forming nanodroplets. Combining these nanodroplets with histotripsy proved to generate a cavitation bubble cloud with similar behavior but lower pressure compared to histotripsy itself. Moreover, these nanodroplets maintained their average size and concentration upon incubation with BSA for 24 hours at 37 degrees celcius, which prove their promise for cancer cell ablation and warrant their future testing in vivo

15. SUBJECT TERMS- nanodroplets, mechanical cell fractionation, histotripsy, lower pressure threshold.

16. SECURITY CLASSIFICATION OF:			17. LIMITATION OF ABSTRACT	18. NUMBER OF PAGES	19a. NAME OF RESPONSIBLE PERSON USAMRMC
a. REPORT	b. ABSTRACT	c. THIS PAGE			19b. TELEPHONE NUMBER (include area code)
U	U	U	UU		

45

Table of Contents

1. INTRODUCTION

Current tumor ablation methods have limitations like low targetibility, which ma cause killing both cancer and surrounded healthy cells[1] and poor imaging ability as a problem for early stage and micro-metastasis[2]. However, the ideal tumor ablation method would provide noninvasive treatment of cancer cells at all stages without damage to surrounding non-cancerous cells. To overcome this problem different ablation techniques were combined with microbubbles. In this case, microbubbles was too high to penetrate into tumor`s interstitial space. Recently, nanodroplets that can extravasate to a tumor's interstitial space have been developed for targeted imaging[3] and drug delivery,[4] but have yet to be utilized for targeted ablation. To address this point, we started working on combining PFC-encapsulated nanodroplets with histotripsy, which is a new, non-invasive, image-guided, ultrasound ablation method.[5] Histotripsy uses extremely high pressure, microseconds long pulses to generate a cluster of microbubbles (bubble cloud) from pre-existing gas pockets in the tissue where the rapid expansion and collapse of the microbubbles disrupts cells.[5b, 5c, 5e] We hypothesize that PFP-loaded nanodroplets with an average diameter < 500nm can diffuse across tumor's leaky vasculature and accumulate in the cancer lesion when administered into the systemic circulation.[6] Applying specific US pulse sequences to the tumor lesion will deliver the acoustic energy necessary to convert the PFP core from the liquid to the gaseous phase in a process known as acoustic droplet vaporization (ADV),[3a, 6a, 7] which will allow real time US imaging of tumor tissue. Unlike histotripsy that relies on cavitation nuclei derived from rare gas pockets in the tissue and extremely high acoustic pressures to initiate the cavitation process, the gas bubbles formed by ADV can act as cavitation nuclei to generate and maintain the cavitation bubble cloud at a significantly reduced pressure. The significantly reduced cavitation threshold will allow us to deliver histotripsy to the tumor tissue "tagged" with the nanodroplets resulting in selective fractionation of cancer cells while sparing the surrounding normal tissue.

2. BODY

Task 1. Formulation and characterization of targeted nano-bubble contrast agents: *To develop a strategy to formulate nano-bubble contrast agents with tunable size, PFP content, and shell flexibility to obtain stable and echogenic nano-bubbles.*

A. _Synthesis and characterization of amphiphilic block copolymer:_ A series of amphiphilic block copolymer was synthesized to be able to formulate nano-bubble contrast agents with tunable size, PFP content, and shell flexibility to obtain stable and echogenic nano-bubbles. The effect of the molar ratio of hydrophilic and hydrophobic monomers and polymer`s molecular weight on the size of nano-bubble were investigated. The results indicated that there are two compositions (ABC-1 and ABC-2 in **Table 1**) better than others in terms of nanodroplets stability and loading capacity. Based on these prescreen we focused on these two compositions in order to optimize conditions for cell ablation. To be able to obtain well-defined amphiphilic block copolymers, individual blocks were prepared separately and combined via one-pot click reaction (**Figure 1**). 2 and 5 KDa PEG with alkyne functionality were prepared through esterification to incorporate into ABC block copolymers and conjugation efficiency was confirm by ¹H NMR as > 95 % for both case. Crosslinkable block obtained via atom transfer radical polymerization (ATRP) has a constant length (10 units) for both copolymer compositions in order to eliminate possible effect of shell thickness on phase transition. This length ideally forms a thin cross-linked shell that stabilizes nanodroplets while allowing phase transition. It was initially synthesized as anthracene functional poly(*tert*-butyl acrylate)-Br (Anth-P*t*BA-Br) which not only carries the functionality for DA "click" reaction, but also carries bromine group that can be easily

Figure 1. Synthesis of amphiphilic block copolymer

transferred into azide group for azide-alkyne click reaction. It is a common strategy to obtain hydrophilic poly(acrylic acid) (PAA) from P*t*BA by simply hydrolysis of *tert*-butyl groups using trifluoroacetic acid (TFA).
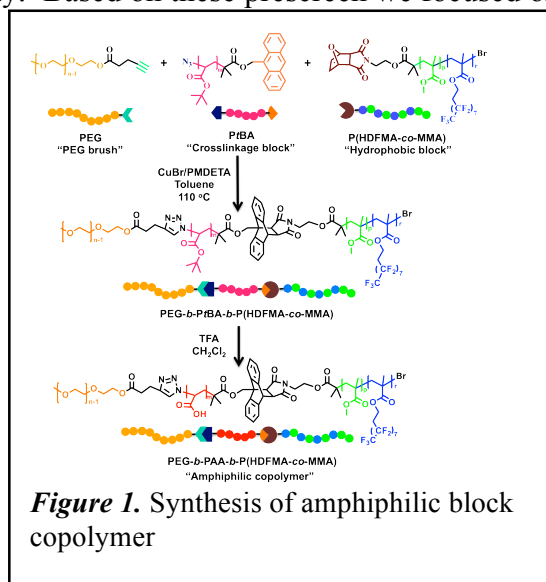
Table 1. Composition of amphiphilic PEG-*b*-PAA-*b*-P(HDFMA-*co*-MMA) copolymers.

Polymer	$M_{n,PEG}$ (g/mol) (# of units)	$M_{n,PtBA}$[a,b] (g/mol) (# of units)	$M_{n,P(MMA-co-HDFMA)}$[a] (g/mol) (# of units)	M_{nHP}/M_{nHF}[c]	# of HP/# of HF units[d]	$M_{n,ABC}$[a] (g/mol)	$M_{n,ABC}$[e] (g/mol)	PD[e]
ABC-1	2000 (45)	1640 (10)	6720 (29)	1.84	**0.53**	10370	9613	1.11
ABC-2	5000 (113)	1640 (10)	11390 (52.5)	1.71	**0.42**	18040	17510	1.12

[a] Calculated from ^{1}H NMR spectra. [b] *Tert*-butyl groups were efficiently hydrolyzed into acid group to obtain the final ABC block copolymer. [c] M_{nHP}/M_{nHF}: Molecular weight of hydrophobic block (HP)/molecular weight of hydrophilic blocks (HF). [d] # of HP/# of HF units: The number of hydrophobic units (HP)/the number of hydrophilic units. [e] Determined by gel permeation chromatography (GPC) using Styragel HR 4E column compared to a series of PMMA standards (PolyAnalitik Inc, Canada) using THF as a mobile phase at a flow rate of 1 ml/min at 35 °C. Data were analyzed using Viscotek OmniSEC Omni-

Therefore, middle block was kept as P*t*BA until ABC block (PEG-*b*-P*t*BA-*b*-P(HDFMA-*co*-MMA) was purified and characterized in order to obtain desired triblock copolymers. In order to investigate the effect of the number of fluorinated monomer units and molecular weight of fluorinated block on loading capacity, P(HDFMA-*co*-MMA) copolymers were designed with two different molecular weight and the number of HDFMA units. Since, most of the fluorinated monomer`s homopolymer has a solubility problem[8], MMA was used as a co-monomer to solubilize HDFMA containing copolymer and copolymerized with HDFMA to obtain fluorinated hydrophobic block with two different degree of polymerization via ATRP using DA reactive protected maleimide functional initiator. The copolymer characteristics like composition and the number of each monomer in the copolymer were calculated using ^{1}H NMR spectrum. The number of HDFMA units in the copolymer were calculated by

Figure 2. Optical absorption spectra of PEG-*b*-PAA-*b*-P(HDFMA-*co*-MMA) (ABC-1) block copolymer and its

integration of methylene protons of HDFMA based on initiator protons as 8 units for ABC-1 and 13.5 units for ABC-2, while the number of MMA units in the copolymer were calculated using the ratio of methyl protons of MMA to initiator protons as 21 units for ABC-1 and 39 units for ABC-2, respectively. HDFMA and MMA were used 20/80 feed ratios and calculated as 27/73 and 26/74 in copolymer, which is enough to have sufficient amount of heptadecafluorodecyl units while maintaining solubility of polymer chains.

Figure 3. GPC results of PEG-*b*-PAA-*b*-P(HDFMA-*co*-MMA) ABC-1(A) and ABC-2 (B) block copolymer and its precursors.

Once well-defined individual blocks were prepared, they were coupled via one-pot "click reaction" in the presence of copper catalyst at 110 °C in toluene for 48 h (*Figure 1*). Copper catalyzed azide-alkyne cycloaddition (CuCAAC) between alkyne functional PEG and azide functional P*t*BA was took placed in the presence of CuBr/PMDETA, while retro DA reaction between furan protected maleimide functional P(HDFMA-*co*-MMA) and anthracene functional P*t*BA was occurred at 110 °C in toluene using slightly excess amount of P*t*BA and PEG which they were simply purified by precipitation. The successful coupling was initially confirmed by ^{1}H NMR spectroscopy. Aromatic protons of anthracene (7.4-8.6 ppm) were completely disappeared while new Diels-Alder cycloadduct protons were appeared with triazole ring proton as an indication of successful dual click reactions. Also, bridgehead protons of cycloadduct were
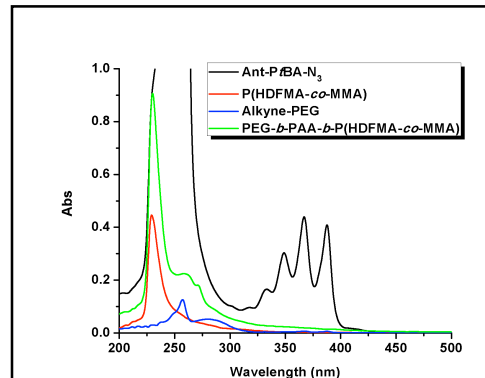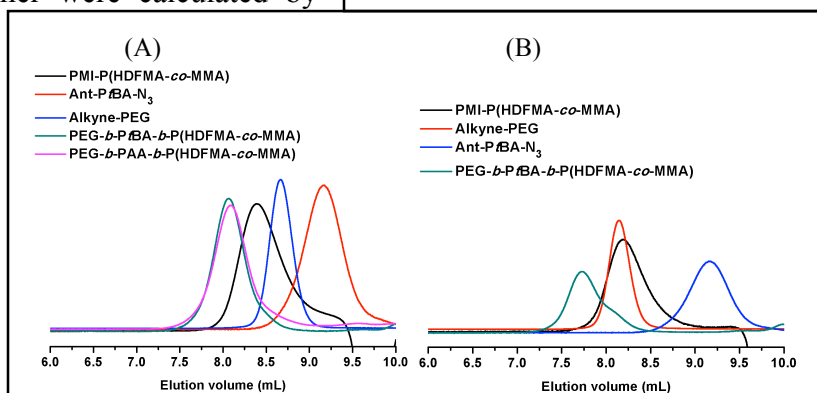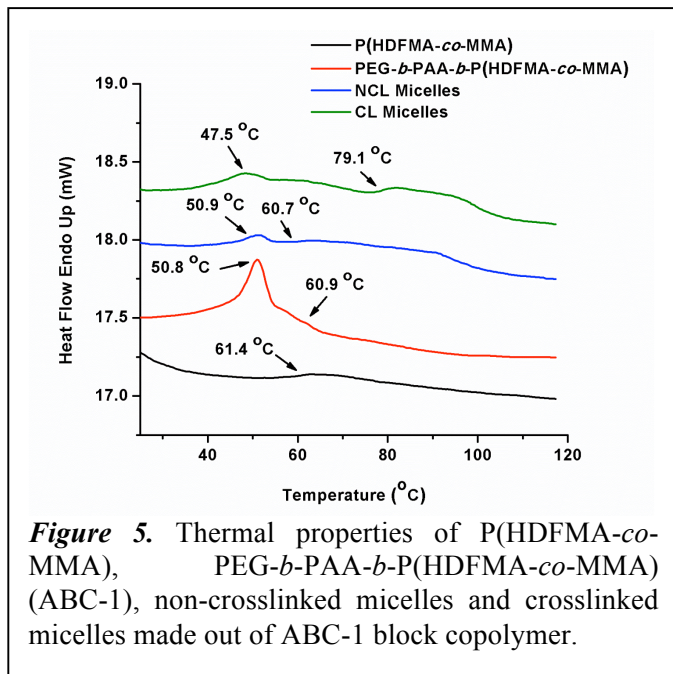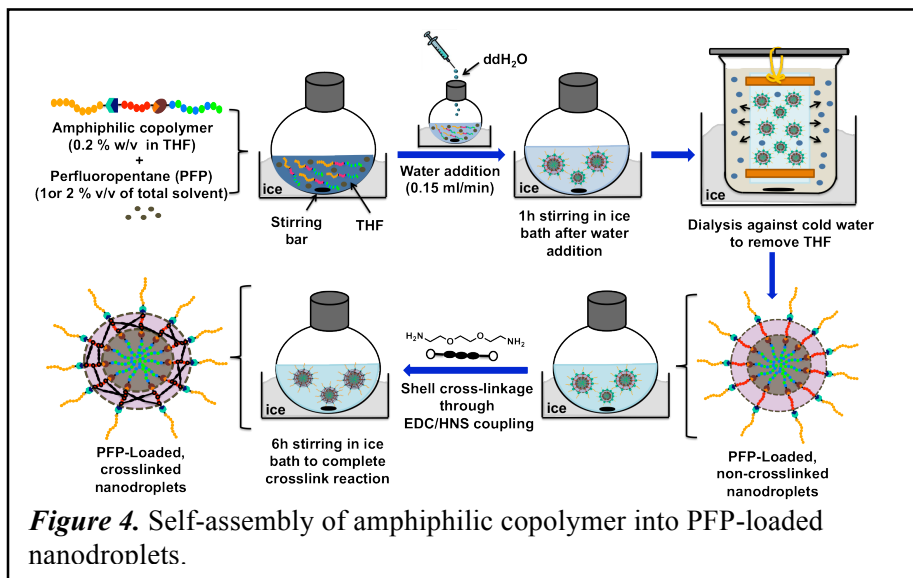
appeared at 4.7 ppm and methylene protons linked to the cycloadduct and CH proton of P*t*BA next to triazole ring were appeared in the region of 5.2-5.6 ppm. DA cycloadduct formation is also monitored by UV spectrophotometer (*Figure 2*). Although, Anth-PtBA-N$_3$ displayed characteristic five-finger absorbance in the range of 300-400 nm, PEG-*b*-P*t*BA-*b*-P(HDFMA-*co*-MMA) triblock copolymer showed no absorbance in this region indicating that DA reaction occurred quantitatively. CuCAAC was further confirmed by FTIR spectroscopy, which did not show any azide or alkyne peaks indicating only existence of triblock copolymer without precursors. Molecular weight and molecular weight distribution of PEG-*b*-

P*t*BA-*b*-P(HDFMA-*co*-MMA) copolymers were also measured using gel permeation chromatography (GPC). A clear shift to low elution volume was observed with narrow polydispersity for both polymer compositions (*Figure 3*). Finally, PEG-*b*-P*t*BA-*b*-P(HDFMA-*co*-MMA) copolymers were hydrolyzed using TFA in order to obtain COOH functionality that can react with diamine functional crosslinker to form a crosslinked shell after self-assembly of block copolymer into nanodroplets. The success of reaction was monitored

Figure 4. Self-assembly of amphiphilic copolymer into PFP-loaded nanodroplets.

using ^{1}H NMR which showed complete reduction on methyl protons of *tert*-butyl groups at 1.43 ppm for PEG-*b*-PAA-*b*-P(HDFMA-*co*-MMA) copolymers (ABC-1 and ABC-2) (*Figure 1*).

B. Preparation and Chacterization of Shell Cross-linked Nanodroplets: Once we obtained well-defined triblock copolymers (ABC-1 and ABC-2) where the molecular weight of the P(HDFMA-*co*-MMA) (6.5kDa and 11.5kDa) and PEG (2kDa and 5kDa), we prepared different amounts of PFP (1% and 2% v/v) nanodroplets to examine their encapsulation efficiency and overall droplets stability. *Figure 4* describes the self-assembly of amphiphilic ABC-1 and ABC-2 polymers around the PFP core with variable PFP content

(0%, 1%, and 2% v/v). ABC-1 and ABC-2 copolymers were dissolved in tetrahydrofuran (THF) followed by cooling down the polymer solution in an ice bath and adding different volumes of PFP (0%, 1%, or 2% v/v) while mixing. An equal amount of water was slowly added to the polymer/PFP mixture to initiate polymers self-assembly into nano-sized micelles that will encapsulate the hydrophobic PFP solution forming nanodroplets. This solution mixture was kept stirring on an ice bath for 1 hour before transferring to a dialysis bag and dialyzing against ice cold water for 12 hours to yield a homogenous milky solution indicating nanodroplets formation. We used 2,2`-(ethylenedioxy)-bis(ethylamine) linker to crosslink the polymer chains via standard NHS/EDC coupling reactions with the central PAA units.[9] Cross-linked nanodroplets were further purified by dialysis against ice-cold water before their characterization and subsequent use in ablation studies.

Figure 5. Thermal properties of P(HDFMA-*co*-MMA), PEG-*b*-PAA-*b*-P(HDFMA-*co*-MMA) (ABC-1), non-crosslinked micelles and crosslinked micelles made out of ABC-1 block copolymer.

We confirmed the cross-linkage of the central PAA block by examining the thermal behavior of the amphiphilic polymer (e.g. ABC-1), the hydrophobic P(HDFMA-*co*-MMA) block, cross-linked droplets, and non-cross-linked droplets when heated between 20-120°C using a differential scanning calorimeter. The P(HDFMA-*co*-MMA) block with an average molecular weight of 6.7 kDa has a glass transition temperature (T_g) of 61.4°C, which increased to 76.5°C with the increase in molecular weight to 11.4 KDa (***Figure 5 & Table 2***). Since the

Table 2. Thermal properties of nanodroplets and its precursors.

Polymer	1st Transition (T_m for PEG) °C[a]	2nd Transition (T_g) °C[a]
P(HDFMA-*co*-MMA)-1	-	61.4
P(HDFMA-*co*-MMA)-2	-	76.5
ABC-1	50.8	60.9
ABC-2	57.2	62.5
NCL-ND-ABC-1[b]	50.9	60.7
CL-ND-ABC-1[b]	47.5	79.1
NCL-ND-ABC-2[b]	55.5	63.9
CL-ND-ABC-2[b]	54.2	65.0

[a] Determined by Differential Scanning Calorimetry (DSC). [b] PFP encapsulated nanodroplets were lypholized before DSC measurement.

PEG and P(HDFMA-*co*-MMA) blocks are not miscible, the thermograph of ABC-1 polymer shows two transitions at 50.8°C and 60.9°C corresponding to the PEG melting point and T_g of the P(HDFMA-*co*-MMA) block, respectively (***Figure 5***). Increasing the molecular weight of the PEG and P(HDFMA-*co*-MMA) blocks increased their melting point and T_g, respectively (***Table 2***). The restricted mobility of the polymer chains in cross-linked droplets prepared using ABC-1 polymer caused an increase in the T_g compared to the parent polymer and non-cross-linked droplets. However, the insignificant difference in the T_g between cross-linked and non-cross-linked droplets prepared using ABC-2 is due to the increase in PEG content (38%) compared to ABC-1
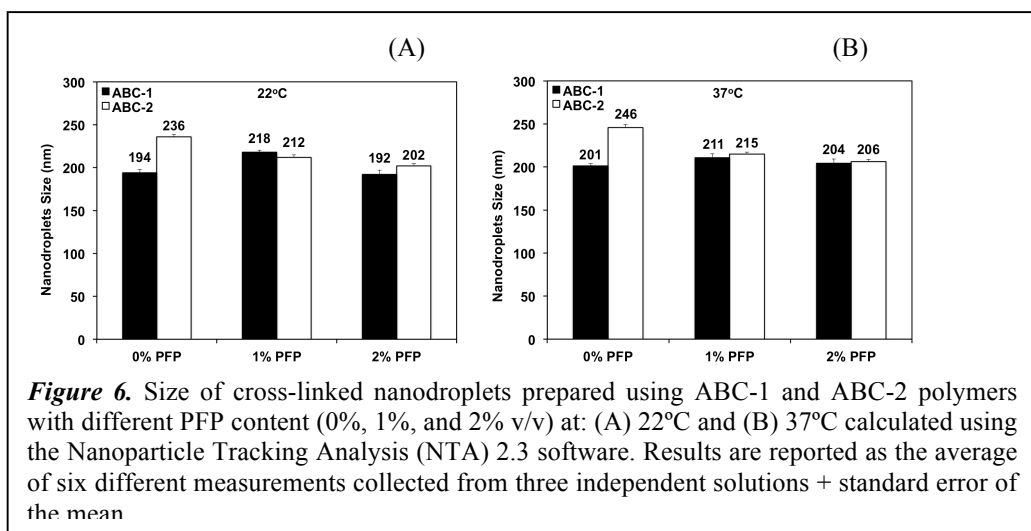

Figure 6. Size of cross-linked nanodroplets prepared using ABC-1 and ABC-2 polymers with different PFP content (0%, 1%, and 2% v/v) at: (A) 22°C and (B) 37°C calculated using the Nanoparticle Tracking Analysis (NTA) 2.3 software. Results are reported as the average of six different measurements collected from three independent solutions + standard error of the mean

(24%), which acts as a plasticizer and reduce the observed T_g as shown in previous reports.[10]

We used Nanosight NS500 (NanoSight Limited, Amesbury, United Kingdom) equipped with a sample

Table 3. Properties of the nanodroplets prepared using ABC-1 and ABC-2 polymers.

Nanodroplets Code	Mode Size at 22°C (nm)[a]	Concentration at 22°C (10^{10}Particles/mL)[a]	Mode Size at 37°C (nm)[a]	Concentration at 37°C (10^{10}Particles/mL)[a]	Zeta Potential (mV)[b]
ND-ABC-1-0% PFP	164.5±8.5	2.31±0.08	162.0±6.5	2.96±0.07	0.1±0
ND-ABC-1-1% PFP	117.5±9.7	2.50±0.05	111.9±6.8	2.58±0.04	0.0±0
ND-ABC-1-2% PFP	126.3±8.0	3.07±0.11	135.3±7.1	3.00±0.12	0.0±0
ND-ABC-1-0% PFP	178.9±7.4	2.98±0.10	187.3±10.8	2.98±0.09	0.0±0
ND-ABC-2-1% PFP	163.0±11.1	3.59±0.09	167.0±9.0	4.09±0.11	0.0±0
ND-ABC-2-2% PFP	159.1±6.2	4.41±0.11	166.8±4.3	4.85±0.12	0.0±0

[a] Mode size represents the most abundant fraction in the nanodroplets solution calculated using Nanoparticles Tracking Analysis (NTA) and NTA 2.3 build 127 software. Results are the average of 6 measurements of a minimum of 3 independent experiments ± standard error of the mean (SEM). [b] Measured using 90Plus particle size analyzer with Zeta PALS capability at room temperature.

chamber with a 640nm laser and a fluoroelastomer O-ring to measure the size and concentration (i.e. number of nanodroplets/mL) of cross-linked (CL) nanodroplets formulated using ABC-1 and ABC-2 polymers as a function of PFP loading (0%, 1%, and 2% v/v) at room (22°C) and body (37°C) temperatures. We relied on the Nanoparticle Tracking Analysis (NTA) 2.3 software to capture and analyze images of

different nanodroplets solutions and calculate the average size of each formulation (*Figure 6*). Results show that nanodroplets formulated using ABC-1 polymer have average diameter of 192±4.7-218±2.1nm at 22ºC, which slightly increased to 201±2.61-211±4.7nm at 37ºC (*Figure 6*). Nanodroplets formulated using ABC-2 polymer have average diameter of 202±2.7-236±2.6nm at 22ºC, which also slightly increased to 206±2.9-246±3.4nm at 37ºC. Results show that the increase in PFP loading from 0%-2% v/v did not influence the average size of all the formulated nanodroplets. It is important to note that NTA software identified the

major fraction in each formulation and calculated its average mode size and concentration (*Table 3*). Results show that the average "mode size" for ND-ABC-1-1% and ND-ABC-1-2% droplets at 37ºC is 111.9±6.8nm and 135.3±7.1nm, respectively. Similarly, the average mode size for ND-ABC-2-1% and ND-ABC-2-2% droplets at 37ºC is 167.0±9.0nm and 166.8±4.3nm, respectively. These results clearly show that the average size of cross-linked (CL) nanodroplets prepared using ABC-1 and ABC-2 polymers with different PFP content is much smaller than the size cutoff (~500nm) of the tumor vasculature.[11] Furthermore, the concentration of cross-linked ND-ABC-1 and ND-ABC-2 nanodroplets did not decrease upon increasing the solution temperature from 22ºC to 37ºC, which indicates droplets resistance to dissolution and stability at body temperature (*Table 3*). These results collectively indicate the promise of these nanodroplets in future *in vivo* evaluation.
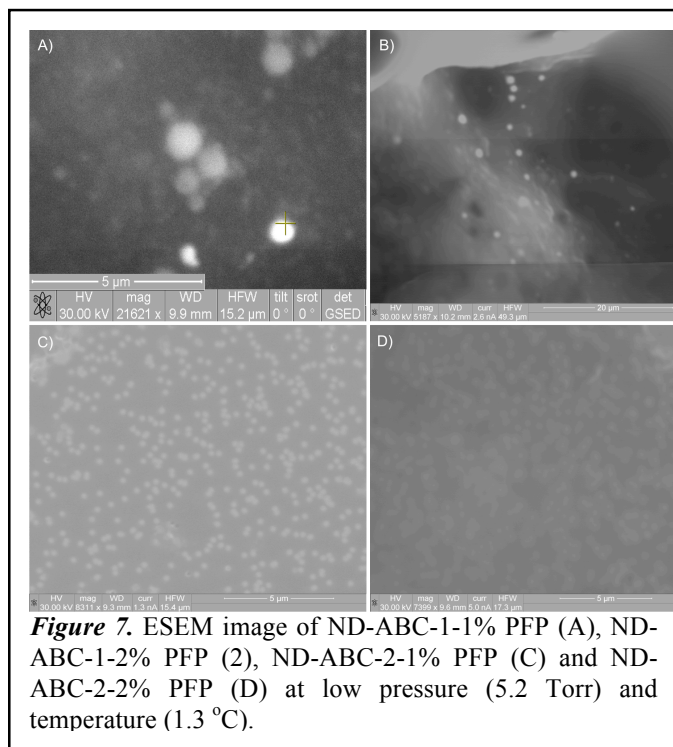

Figure 7. ESEM image of ND-ABC-1-1% PFP (A), ND-ABC-1-2% PFP (2), ND-ABC-2-1% PFP (C) and ND-ABC-2-2% PFP (D) at low pressure (5.2 Torr) and temperature (1.3 ºC).
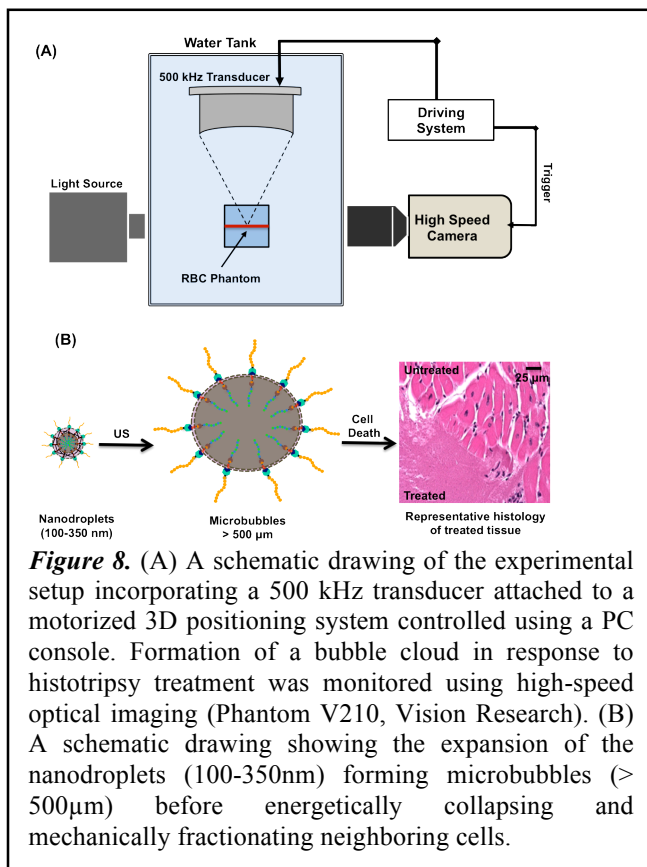
We visualized different nanodroplets formulations using a FEI Quanta 3D Dual-Beam Environmental Scanning Electron Microscope (FEI Co., Oregon, USA) under low pressure (5.2 Torr) and temperature (1.3ºC) to examine droplets morphology. Images of all PFP-loaded formulations show spherical nanodroplets (*Figure 7*) with average size of 316±49nm, 342±11nm, 310±10nm, and 333±9nm for ND-ABC-1-1% PFP, ND-ABC-1-2% PFP, ND-ABC-2-1% PFP, and ND-ABC-2-2% PFP, respectively. The higher average size observed with scanning electron microscopy analysis is a result of the small number of droplets manually analyzed compared to NTA, which measures the size of each droplet in the solution. We used 90Plus particle size analyzer with ZetaPALS capability (Brookhaven Instruments Corporation, Holtsville, NY) to measure the zeta potential of nanodroplets formulations, which was ~0 mV indicating a neutral droplets surface (*Table 3*).

C. Measurement of Histotripsy Threshold in Agarose Tissue Phantoms:
Agarose tissue phantoms (1% w/v) have been used as model tissue phantoms to investigate the ablative effects of histotripsy therapy.[12] To compare the effects of our nanodroplet-mediated ablation to histotripsy alone at higher pressure, we treated agarose tissue phantoms

Figure 8. (A) A schematic drawing of the experimental setup incorporating a 500 kHz transducer attached to a motorized 3D positioning system controlled using a PC console. Formation of a bubble cloud in response to histotripsy treatment was monitored using high-speed optical imaging (Phantom V210, Vision Research). (B) A schematic drawing showing the expansion of the nanodroplets (100-350nm) forming microbubbles (> 500µm) before energetically collapsing and mechanically fractionating neighboring cells.

(1% w/v) containing each of our nanodroplet formulations (*Figure 8*). Briefly, the agarose phantom was

6

placed in the focal zone of a 32 element, 500 kHz, transducer inside a degassed water tank at 37°C (**Figure 8, Panel A**). A high-speed, 1 megapixel CCD camera (Phantom V210, Vision Research) was positioned to image the plane of the RBCs layer throughout the histotripsy treatment using a flash lamp as a backlight for the phantom to record the bubble cloud formed from the expansion of the embedded nanodroplets into microbubbles. We hypothesized that ultrasound treatment of the embedded nanodroplets will trigger acoustic droplet vaporization forming microbubbles, which will expand reaching an average size > 50μm before they violently collapse causing disruption of the neighboring RBCs (**Figure 8, Panel B**). Disruption of the translucent RBCs layer renders the agarose gel more transparent, which provides visual evidence of cell ablation. Previous work has demonstrated that damage to the RBC tissue phantoms directly correlates to the tissue damage formed by histotripsy therapy.[12] The pressure threshold to vaporize the nanodroplets and

expand the resulting bubbles >50 μm was measured in tissue-mimicking agarose phantoms with and without nanodroplets. Based on the analysis of high-speed images, results demonstrated a significant decrease in the histotripsy threshold with nanodroplets compared to histotripsy only controls. The minimum pressure level at which cavitation bubbles >50 μm was observed by high speed images to be 3.02±2.49 MPa for phantoms containing nanodroplets and 15.60±2.35 MPa for histotripsy only controls without nanodroplets (**Figure 9**).

D. Ablation of Red Blood Cell in Tissue Phantom: Agarose tissue phantoms (1% w/v) with an embedded layer of red blood cells (RBCs) have been used as model tissue phantoms to investigate the ablative effects of histotripsy therapy. We tested our hypothesis by applying histotripsy pulses to the center of the agarose gels at the RBC layer using a pulse repetition frequency of 10Hz at a peak negative pressure of

Figure 9. A plot showing the histotripsy threshold in agarose tissue phantoms with and without nanodroplets. Results demonstrated a significant decrease in the pressure threshold to generate cavitation bubbles >50 μm with nanodroplets compared to control conditions (histotripsy only).

20.7MPa. We embedded an equal number of nanodroplets (2.36 x 10^8 droplets/mL) in the agarose gel to eliminate the effect of droplets concentration on the observed ablation behavior but rather focus on investigating the effect of polymer composition (ABC-1 versus ABC-2) and PFP content (0%, 1%, and 2%
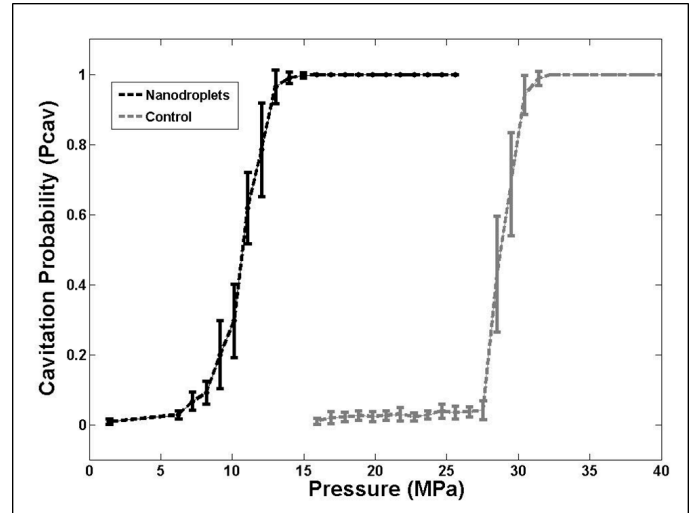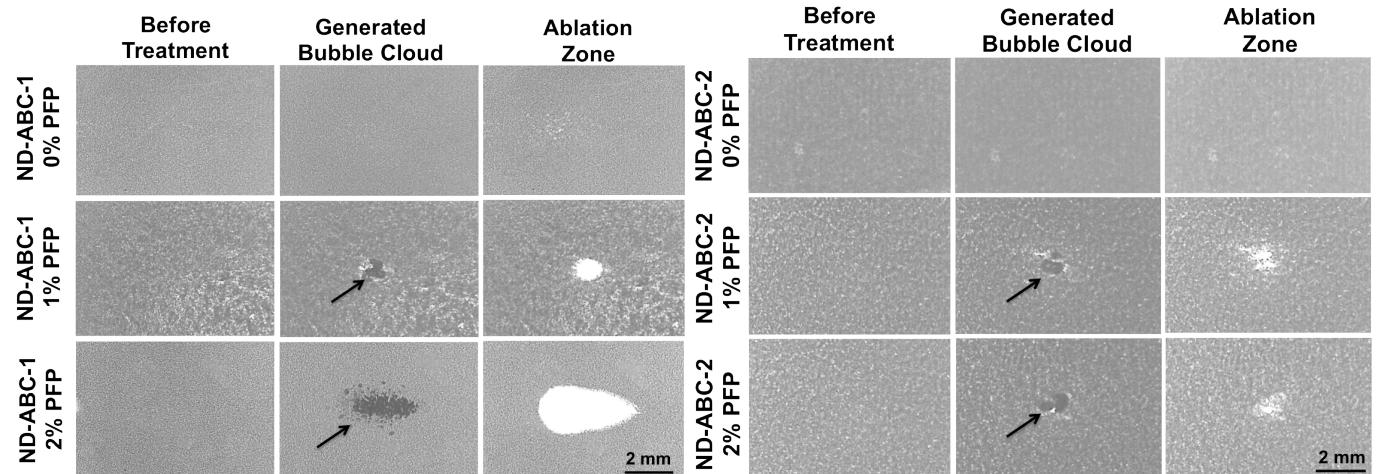

Figure 10. (A) Effect of 2-cycle histotripsy pulse (20.7MPa) with a pulse repetition frequency of 10MHz on the nanodroplets prepared using ABC-1 and ABC-2 polymers with different PFP loading and embedded with RBCs in agarose gels. Images were captured using high-speed, 1 megapixel CCD camera (Phantom V210, Vision Research) capable of a maximum frame rate of 2000 fps and show the generated bubble cloud and the corresponding transparent ablation zone.

v/v) on ablation capacity to identify the most effective formulation. Results show that histotripsy application could not initiate a bubble cloud from empty nanodroplets (i.e. 0% PFP loading) prepared using ABC-1 and

ABC-2 polymers at the applied acoustic pressure (20.7MPa) and no damage was observed in the RBCs layer (***Figure 10***). A similar histotripsy application to tissue phantoms containing nanodroplets prepared using ABC-1 polymer loaded with 1% and 2% v/v PFP resulted in the formation of a bubble cloud in the center of the gel and formation of a corresponding transparent zone confirming the ablation of the RBCs (***Figure 10***). The nanodroplets prepared using ABC-2 polymer and loaded with 1% and 2% v/v PFP also resulted in cavitation and lesion formation in response to the histotripsy treatment.

We measured the surface area of the lesions formed in each tissue phantom and plotted it against nanodroplets composition and PFP content (***Figure 11***). Results show that empty nanodroplets (i.e. 0% PFP loading) caused no ablation to RBCs regardless of the polymer composition used to formulate the nanodroplets. This demonstrates that the loading of PFP in the droplets' core is critical for bubble formation in response to histotripsy treatment. Increasing PFP content from 1% to 2% v/v caused an increase in the surface area of the ablation lesion from $0.67\pm0.23mm^2$ to $5.60\pm0.52mm^2$ (8.4 folds) for nanodroplets prepared using ABC-1 polymer. Similarly, increasing PFP content in the nanodroplets prepared using ABC-2 polymer from 1% to 2% v/v increased the surface area of the ablation lesion from $0.37\pm0.17mm^2$ to $1.59\pm1.86mm^2$ (4.3 folds). It is interesting to note that nanodroplets prepared using ABC-1 polymer exhibit higher ablation capacity compared to those prepared using ABC-2 polymer, which can be attributed to difference in polymer's capacity to encapsulate and retain the loaded PFP. Specifically, ABC-2 polymer has an average of 13.5 units of the fluorinated monomer with the heptadecafluorodecyl groups distributed along a long hydrophobic backbone, which results in strong interaction of the hydrophobic block in the droplets core that limits PFP loading and encapsulation.

Our results are supported by previously published results showing that the number of fluorinated monomers plays a critical role in PFC loading and encapsulation by a polymeric shell.[13] For example, Yokoyama and coworkers synthesized a series of amphiphilic PEG-*b*-poly(fluoroheptyl aspartate) copolymers with a variable number of fluorinated alkyl chains and investigated their ability to encapsulate PFC forming nanodroplets.[13] Results
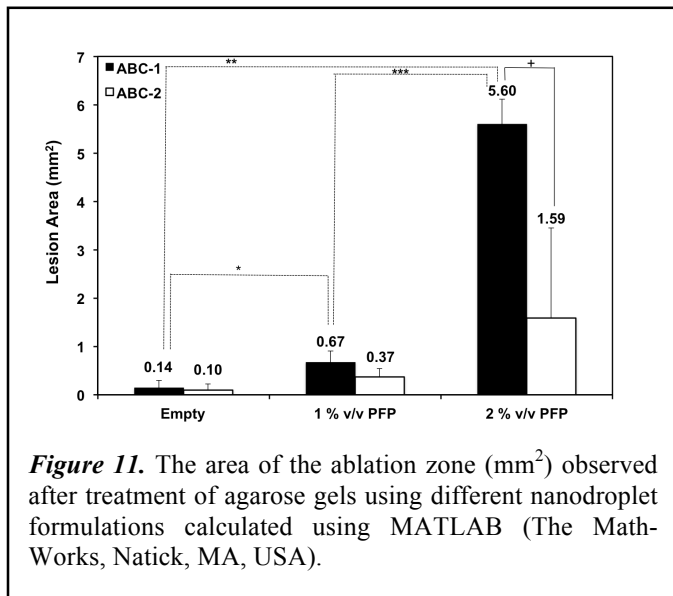

Figure 11. The area of the ablation zone (mm^2) observed after treatment of agarose gels using different nanodroplet formulations calculated using MATLAB (The Math-Works, Natick, MA, USA).
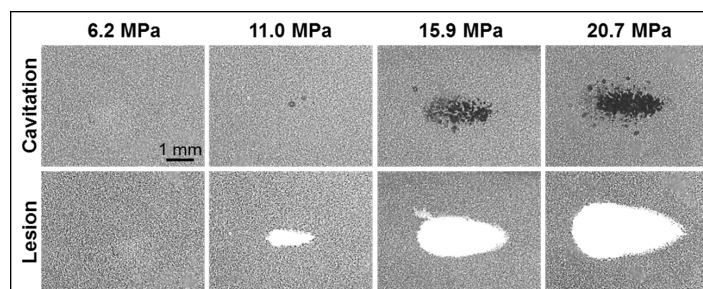

Figure 12. Optical images of nanodroplet-mediated cell fractionation. Images of cavitation bubble cloud (dark) and lesions (white) generated in the RBC agarose gel (grey) using nanodroplet-mediated histotripsy at different pressure levels. A total of 2000 2-cycle pulses at 10 Hz PRF were used for each treatment.
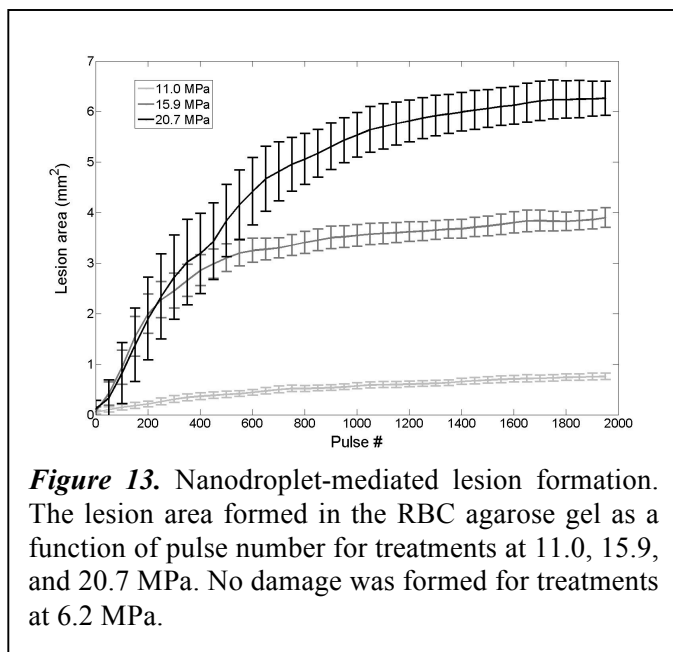

Figure 13. Nanodroplet-mediated lesion formation. The lesion area formed in the RBC agarose gel as a function of pulse number for treatments at 11.0, 15.9, and 20.7 MPa. No damage was formed for treatments at 6.2 MPa.

show that introducing 10% of fluoroheptyl units in the polymer backbone was sufficient to encapsulate the loaded PFP (45.5 mg/mL) forming nanodroplets. Incorporation of higher or lower percentages of fluoroheptyl units in the polymer backbone reduced PFP encapsulation by the polymer and negatively affected droplets stability. Further, the increase in the number of fluorinated carbon atoms in the fluoroalkyl chain above 9 decreases the encapsulation of PFP. These results collectively show that the nanodroplets formulated using ABC-1 polymer and loaded by 2% PFP exhibit the highest ablation capacity among all formulations.

Once we determined the best composition and loaded PFP %, a detail investigation was performed using this composition. At peak negative pressure below 10 MPa, no microbubbles were observed and no lesions were visualized. At peak negative pressure of 11.0 MPa and greater, when cavitation bubbles were generated, well-defined lesions were formed in the RBC phantoms using nanodroplets combined with histotripsy (*Figure 12*). Nanodroplet-mediated histotripsy fractionated the RBC phantom with similar efficiency to histotripsy at higher pressure with all RBCs within the focal volume completely fractionated within 2,000 pulses, resulting in transparent lesions with no intact RBCs remaining. The area of lesion in the RBC layer increased with increasing pressure. For example, the lesion areas for RBC phantoms containing nanodroplets (n=6) were 0.77 ± 0.09 mm^2, 3.92 ± 0.41 mm^2, and 6.27 ± 0.86 mm^2 for peak negative pressures of 11.0 MPa, 15.9 MPa, and 20.7 MPa, respectively (*Figure 12*). Furthermore, lesion area was plotted as a function of pulse number demonstrating >75% of the focal region was fractionated within the first 1,000 pulses and >95% of the focal region fractioned after 1,500 pulses at all pressure levels treated (*Figure 13*). In comparison, in control gels without nanodroplets, no lesions were formed at any treatments in this pressure range. These results are important to show that nanodroplet-mediated cavitation can indeed create cell disruption with the same effectiveness (i.e., the same number of pulses) as using histotripsy alone but at a significantly lower pressure. This is an important validation of our hypothesis confirming that the cavitating microbubbles generated via nanodroplets are destructive to use for ablation.

E. Selective Cavitation in Composite Agarose Phantom:

Based on the reduced histotripsy threshold using nanodroplets, cavitation should be selectively generated in multi-tumor nodules with nanodroplets inside the focal zone, whereas no cavitation should be formed at normal tissue without nanodroplets. The feasibility of using nanodroplets to generate selective cavitation was investigated using a composite agarose tissue phantom. Histotripsy pulses were applied inside the composite agarose tissue phantom containing inclusions with nanodroplets. Using 2-cycle pulses at a peak negative pressure of 17.3 MPa, which is above the histotripsy threshold using nanodroplets and below the intrinsic
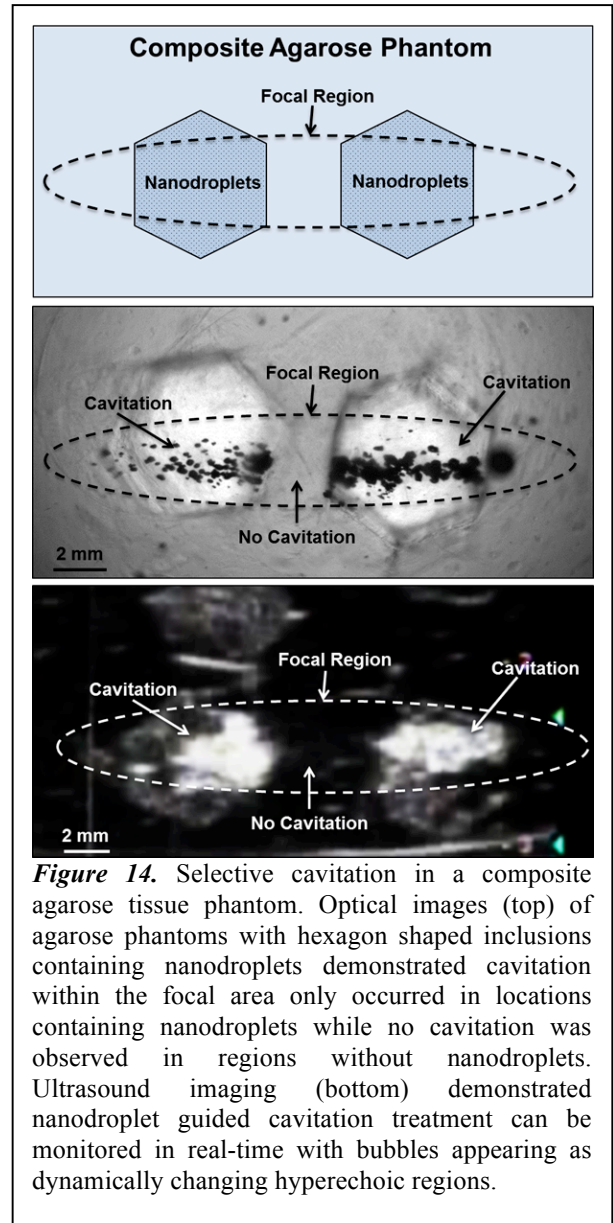

Figure 14. Selective cavitation in a composite agarose tissue phantom. Optical images (top) of agarose phantoms with hexagon shaped inclusions containing nanodroplets demonstrated cavitation within the focal area only occurred in locations containing nanodroplets while no cavitation was observed in regions without nanodroplets. Ultrasound imaging (bottom) demonstrated nanodroplet guided cavitation treatment can be monitored in real-time with bubbles appearing as dynamically changing hyperechoic regions.
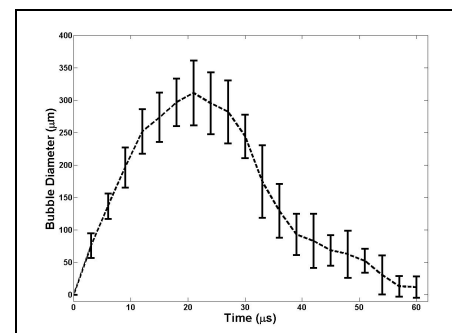

Figure15. A plot of bubble behavior in agarose tissue phantoms. The diameter of bubble generated using a 2-cycle 500kHz pulse at 15MPa as a function of time. At each time point, the average bubble diameter and standard deviation are plotted.

9

threshold using histotripsy alone, cavitation bubble clouds were formed only in the inclusions containing nanodroplets located within the focal volume of the 500 kHz transducer (***Figure 14, top***). Optical images indicated two separate dense cavitation clouds inside the nanodroplet-containing inclusions inside the focal region throughout the 2000 pulses while no bubbles were observed outside the inclusions within the focal region (***Figure 14 middle***). Correspondingly, ultrasound imaging showed two dynamically changing hyperechoic zones inside the hexagon inclusions, while no bubbles were observed elsewhere (***Figure 14, bottom***). As these cavitation bubbles generated in the process are viewed clearly on ultrasound imaging, the histotripsy therapy process can be monitored and guided by ultrasound imaging in real-time.

F. Bubble Behavior: The bubble expansion and collapse observed in histotripsy is substantially more energetic than traditionally defined inertial cavitation where the maximal bubble diameter becomes equal or greater than twice the initial bubble size.[14] In histotripsy, microbubbles formed from preexisting nuclei <10 nm grow to over 50 μm before violently collapsing, all occurring within 100 μs. This bubble behavior is critical to achieve cell disruption. To study the behavior of cavitation bubbles generated by nanodroplet-mediated histotripsy, optical images of bubbles were recorded by the high-speed camera at different time delays after the arrival of the histotripsy pulse. The peak negative pressure of 15.6 MPa was used, because it is the lowest pressure at which a cavitation cloud was always generated (P_{cav}=1) using nanodroplets. In agarose gel, the bubble diameter increased to the maximum diameter of 311.2±49.9 μm at 21 μs (***Figure 15***). The average bubble lifespan from the arrival of the histotripsy pulse to when the bubble became too small to be observed on the optical image was measured to be ~60 μs (***Figure 14***). This level of bubble expansion and collapse is similar to the behavior of bubbles formed using histotripsy alone at higher pressures and is anticipated to create cell disruption.

G. Stability of PFP-Loaded Nanodroplets: We investigated the stability of nanodroplets prepared using ABC-1 and ABC-2 polymers and loaded with 2% v/v PFP upon incubation for 24 hours at 37ºC in presence and absence of bovine serum albumin (20 μg/ml) as a model serum protein. Using NTA software, we measured the mode and mean size for each formulation at the beginning of the incubation time (0hr) and after 24 hours along with droplets concentration. Results show that the nanodroplets prepared using ABC-1 polymer have an initial mode size and mean size of 131.3±10.9nm and 237.35±6.1nm, respectively (***Table 4 & Figure 16, Panel A***). Incubating the droplets at 37ºC for 24 hours caused a slight shift in mode size and mean size to 142.0±10.5nm
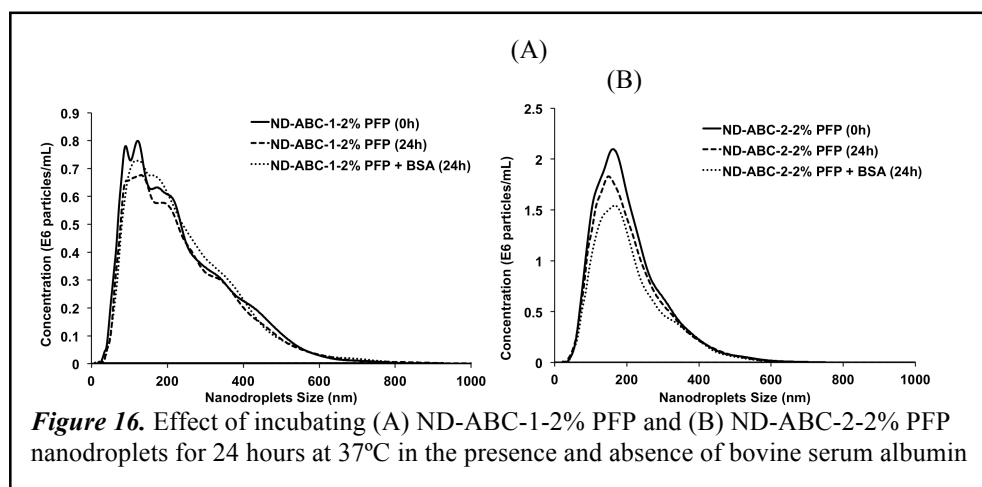

Figure 16. Effect of incubating (A) ND-ABC-1-2% PFP and (B) ND-ABC-2-2% PFP nanodroplets for 24 hours at 37ºC in the presence and absence of bovine serum albumin

and 243.9±6.0nm, respectively.
Incubating the nanodroplets with BSA did not affect nanodroplets mode size (144.5±13.9nm) and mean size (242.6±4.1nm), which indicates the success of the PEG brush displayed on droplets surface in

Table 4. Effect of incubating nanodroplets at 37ºC for 24 hours in presence and absence of bovine serum albumin on droplets size and concentration.

Nanodroplets Code	Mode Size (nm)[a,b]	Mean Size (nm)[a]	Concentration (10[10]Particles/mL)[a,c]
ND-ABC-1-2% PFP (0h)	131.3±10.9	237.35±6.1	1.98±0.09
ND-ABC-1-2% PFP (24h)	142.0±10.5	243.9±6.0	1.81±0.06
ND-ABC-1-2% PFP+BSA (24h)	144.5±13.9	242.6±4.1	1.93±0.07
ND-ABC-2-2% PFP (0h)	160.0±4.4	207.6±3.2	3.87±0.17
ND-ABC-2-2% PFP (24h)	152.6±4.3	207.0± 3.3	3.45±0.16
ND-ABC-2-2% PFP+BSA (24h)	159.0±7.8	209.6±2.5	2.94± 0.12

[a]Results are the average of 6 measurements of a minimum of 3 independent experiments ± standard error of the mean (SEM). [b] Mode size represents the most abundant fraction in the nanodroplets solution. [c] Nanoparticles concentration is calculated using Nanoparticles Tracking Analysis (NTA) and NTA 2.3 build 127 software.

suppressing BSA adsorption. Results also show that nanodroplets concentration did not change throughout the 24 hours incubation time in presence or absence of BSA, which indicates their stability against dissolution and aggregation. Analysis of mode and mean size of the nanodroplets prepared using ABC-2 and encapsulate 2% v/v PFP show that they maintained their size throughout the incubation time and in presence of BSA (***Table 4 & Figure 16, Panel B***). However, there was a 25% reduction in droplets concentration upon incubation with BSA for 24 hours, which is probably due to droplets dissolution or poor PFP encapsulation indicated by the low ablation capacity of these droplets shown in ***Figure 10***. These results show that ND-ABC-1-2% PFP nanodroplets resist the adsorption of serum proteins and are suited for *in vivo* testing.

H. Cytotoxicity of Nanodroplets: Finally, we investigated the toxicity of ABC-1 and ABC-2 polymers towards PC-3 prostate cancer cells as a function of polymer concentration using the MTT assay (ATCC, Manassas, VA) following manufacturer's specifications. Briefly, we incubated PC-3 cells with ABC-1 and ABC-2 polymers formulated as empty nanodroplets (i.e. 0% loaded PFP) for 24 hours under normal culture conditions and compared the percentage of viable cells at each polymer concentration (0.3-75 µg/mL) to that observed for PC-3 cultured in normal culture medium (0 µg/mL polymer). Results show that the nanodroplets did not affect the viability of PC-3 cells at any of the tested concentrations (***Figure 17***) indicating their biocompatibility. We did not evaluate the toxicity of the PFP given that it is commonly used in FDA-approved ultrasound contrast agents and its concentration in the blood circulation drops by 90% within 10 minutes of its administration.[13a13a]

Figure16. Evaluation of *in vitro* cytotoxicity of nanodroplets by MTT assay. PC-3 prostate cancer cells were incubated with different concentration of nanodroplets for 24 h.

To summarize, we have designed and synthesized two amphiphilic PEG-*b*-(PAA)-*b*-P(HDFMA-*co*-MMA) polymers (ABC-1 & ABC-2) that proved to encapsulate 1%-2% v/v PFP forming nanodroplets. Combining histotripsy pulses with nanodroplets formulated using ABC-1 and ABC-2 polymers proved to generate a cavitation bubble cloud that ablates neighboring RBCs at reduced acoustic pressure compared to histotripsy alone. The increase in PFP content from 1% to 2% v/v proved to increase the ablation lesion induced by the nanodroplets. Further, the nanodroplets formulated using ABC-1 appear to better encapsulate the loaded PFP and exhibit higher ablation capacity compared to those formulated by ABC-2 polymer at equal PFP loading. Based on the surface area of the ablation zone, ND-ABC-1-2% PFP nanodroplets exhibit effective ablation of RBCs at 2.5-fold lower acoustic pressure than the intrinsic threshold required initiating the bubble cloud using the same 2-cycle histotripsy pulses alone. Further, these nanodroplets maintained their average size and concentration upon incubation with BSA for 24 hours at 37ºC, which prove their promise for cancer cell ablation and warrant their future testing *in vivo*.

All these finding that we have got related to Task 1 has been either published or submitted to be published, see Appendix A and B.

Task 2. Investigate the feasibility of using targeted nano-bubbles for contrast-enhanced US imaging of prostate cancer cells *in vitro* and *in vivo*

When PFP encapsulated in such a small nanodroplets, using them as contrast agent becomes challenging task since their transition from liquid to gas becomes harder. However, our selective ablation experiment (***Figure 14, bottom***) showed that they could be visible when they accumulated on a certain region. Once we prepare the targeted nanodoplets that will specifically go to the prostate cancer cell, there is a possibility to image them using nanodroplets as contrast agent right before cell ablation. This aim will be revisit during *in vivo* experiment.

Task 3. Investigate the feasibility of using targeted nano-bubbles coupled with histotripsy for precise and efficient multi-foci prostate cancer cell ablation

Progress on aim 3 will be presented in next report term.
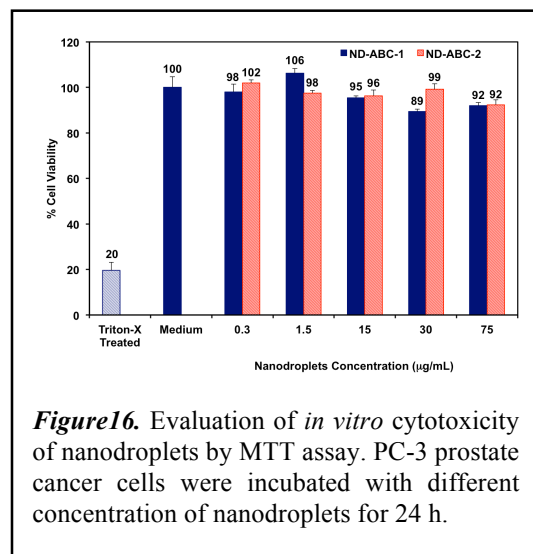
3. KEY RESEARCH ACCOMPLISHMENTS

- A series of amphiphilic block copolymers was synthesized and prescreened to be able to formulate nanodroplets contrast agents with tunable size, PFP content, and shell flexibility to obtain stable and echogenic nanobubbles.

- Self-assembly of most effective two amphiphilic, ABC-1 and ABC-2, polymers around the PFP core with variable PFP content (0%, 1%, and 2% v/v) resulted PFP-loaded nanodroplets in the size range of 100-350 nm.

- Significant decrease in the histotripsy threshold with PFP-loaded nanodroplets (3.10±2,49 MPa) was observed compared to histotripsy alone (15.60±2.35 MPa).

- The similar level of bubble expansion and collapse with histotripsy was observed in agarose gel, the bubble diameter increased to the maximum diameter of 311.2±49.9 μm at 21 μs.

- We were able to ablate Red Blood Cell layer at lower pressure threshold combining nanodroplets with histotripsy.

- Nanodroplets made by ABC-1 with 2% PFP is the most effective composition based on calculated damaged area in the agarose phantom.

- Selective ablation of PFP-Loaded nanodroplets proved that cavitation should be selectively generated in multi-tumor nodules with nanodroplets inside the focal zone, whereas no cavitation should be formed at normal tissue without nanodroplets.

- These nanodroplets have a potential to be used as imaging agent in-vivo

- These nanodroplets maintained their average size and concentration upon incubation with BSA for 24 hours at 37ºC, which prove their promise for cancer cell ablation and warrant their future testing *in vivo*.

- They are not toxic at the level of tested concentration.

4. REPORTABLE OUTCOMES
- A manuscript has been published in Theranostic (Appendix A)

Nanodroplet-Mediated Histotripsy for Image-guided Targeted Ultrasound Cell Ablation, E. Vlaisavljevich, Y. Y. Durmaz, A. Maxwell, M.E.H. ElSayed, Zhen Xu, *Theranostics*, 2013, 3(11), 802-815.

- Another one is under review (Appendix B)

Development of Nanodroplets for Histotripsy-Mediated Cell Ablation, Y. Y. Durmaz, E. Vlaisavljevich, Z. Xu, M.E.H ElSayed, *Angewandte Chemie International Edition*, 2013 Submitted.

5. CONCLUSION

To summarize, we have designed and synthesized several amphiphilic PEG_x-b-$(PAA)_y$-b-$P(HDFMA_z$-co-$MMA_w)$ copolymers that proved to encapsulate 1%-2% v/v PFP forming nanodroplets. Combining histotripsy pulses with nanodroplets formulated using these copolymers proved to generate a cavitation bubble cloud that ablates neighboring RBCs at reduced acoustic pressure compared to histotripsy alone. The increase in PFP content from 1% to 2% v/v proved to increase the ablation lesion induced by the nanodroplets. Further, the nanodroplets formulated using PEG_{45}-b-$(PAA)_{10}$-b-$P(HDFMA_8$-co-$MMA_{21})$ appear (ND-ABC-1) to better encapsulate the loaded PFP and exhibit higher ablation capacity compared to those formulated by PEG_{113}-b-$(PAA)_{10}$-b-$P(HDFMA_{13.5}$-co-$MMA_{52})$ polymer at equal PFP loading. Based on the surface area of the ablation zone, ND-ABC-1-2% PFP nanodroplets exhibit effective ablation of RBCs at 2.5-fold lower acoustic pressure than the intrinsic threshold required initiating the bubble cloud using the same 2-cycle histotripsy pulses alone. Nanodroplet-mediated histotripsy was shown capable of creating microbubble expansion and collapse as well as well-defined ablation similar to histotripsy but at significantly lower pressure. Further, these nanodroplets maintained their average size and concentration upon incubation with BSA for 24 hours at 37ºC, which prove their promise for cancer cell ablation and warrant their future testing *in vivo*.

6. References

[1]   a) M. Mendizabal, K. R. Reddy, *Med Clin North Am* **2009**, *93*, 885-900, b) M. Kudo, *Oncology.* **2010**, *78*, 113-124. Epub 2010 Jul 2018.

[2]   a) G. S. Gazelle, S. N. Goldberg, L. Solbiati, T. Livraghi, *Radiology.* **2000**, *217*, 633-646, b) R. O. Illing, J. E. Kennedy, F. Wu, G. R. ter Haar, A. S. Protheroe, P. J. Friend, F. V. Gleeson, D. W. Cranston, R. R. Phillips, M. R. Middleton, *Br J Cancer* **2005**, *93*, 890-895.

[3]   a) P. S. Sheeran, V. P. Wong, S. Luois, R. J. McFarland, W. D. Ross, S. Feingold, T. O. Matsunaga, P. A. Dayton, *Ultrasound in Medicine and Biology* **2011**, *37*, 1518-1530, b) K. Wilson, K. Homan, S. Emelianov, *Nature communications* **2012**, *3*, 618 (610 pp.), c) N. Rapoport, K. H. Nam, R. Gupta, Z. Gao, P. Mohan, A. Payne, N. Todd, X. Liu, T. Kim, J. Shea, C. Scaife, D. L. Parker, E. K. Jeong, A. M. Kennedy, *Journal of controlled release : official journal of the Controlled Release Society* **2011**, *153*, 4-15, d) K. i. Kawabata, R. Asami, T. Azuma, S. i. Umemura, *Japanese Journal of Applied Physics* **2010**, *49*, 07HF18 (09 pp.).

[4]   a) N. Y. Rapoport, K. H. Nam, Z. Gao, A. Kennedy, *Acoustical Physics* **2009**, *55*, 594-601, b) N. Rapoport, K.-H. Nam, R. Gupta, Z. Gao, P. Mohan, A. Payne, N. Todd, X. Liu, T. Kim, J. Shea, C. Scaife, D. L. Parker, E.-K. Jeong, A. M. Kennedy*, Vol. 153*, 1 ed., Elsevier, P.O. Box 211, Amsterdam, 1000 AE, Netherlands, **2011**, pp. 4-15.

[5]   a) K. Kieran, T. L. Hall, J. E. Parsons, J. S. Wolf, Jr., J. B. Fowlkes, C. A. Cain, W. W. Roberts, *J Urol* **2007**, *178*, 672-676, b) F. Winterroth, Z. Xu, T. Y. Wang, J. E. Wilkinson, J. B. Fowlkes, W. W. Roberts, C. A. Cain, *Ultrasound Med Biol* **2011**, *37*, 78-86, c) Z. Xu, Z. Fan, T. L. Hall, F. Winterroth, J. B. Fowlkes, C. A. Cain, *Ultrasound Med Biol* **2009**, *35*, 245-255, d) Z. Xu, J. B. Fowlkes, C. A. Cain, *IEEE Trans Ultrason Ferroelectr Freq Control* **2006**, *53*, 1412-1424, e) Z. Xu, J. B. Fowlkes, E. D. Rothman, A. M. Levin, C. A. Cain, *J Acoust Soc Am* **2005**, *117*, 424-435.

[6]   a) Z. Gao, A. M. Kennedy, D. A. Christensen, N. Y. Rapoport, *Ultrasonics* **2008**, *48*, 260-270. Epub 2007 Nov 2019, b) K. i. Kawabata, R. Asami, H. Yoshikawa, T. Azuma, S. i. Umemura, *Japanese Journal of Applied Physics* **2010**, *49*, 07HF20 (04 pp.), c) P. S. Sheeran, S. Luois, P. A. Dayton, T. O. Matsunaga, *Langmuir* **2011**, *27*, 10412-10420.

[7]   Kripfgans Od, Fowlkes Jb, Miller Dl, Eldevik Op, Carson Pl, *Ultrasound Med. Biol.* **2000**, *26*, 1177-1189.

[8]   S. Perrier, S. G. Jackson, D. M. Haddleton, B. Ameduri, B. Boutevin, *Tetrahedron* **2002**, *58*, 4053-4059.

[9]   a) X. K. Sun, R. Rossin, J. L. Turner, M. L. Becker, M. J. Joralemon, M. J. Welch, K. L. Wooley, *Biomacromolecules* **2005**, *6*, 2541-2554, b) K. Nam, T. Kimura, A. Kishida, *Macromol. Biosci.* **2008**, *8*, 32-37.

[10]   A. A. Deschamps, D. W. Grijpma, J. Feijen, *Polymer* **2001**, *42*, 9335-9345.

[11]   a) Z. Gao, A. M. Kennedy, D. A. Christensen, N. Y. Rapoport, *Ultrasonics* **2008**, *48*, 260-270, b) P. S. Sheeran, S. Luois, P. A. Dayton, T. O. Matsunaga, *Langmuir* **2011**, *27*, 10412-10420.

[12]   A. D. Maxwell, T. Y. Wang, L. Q. Yuan, A. P. Duryea, Z. Xu, C. A. Cain, *Ultrasound Med. Biol.* **2010**, *36*, 2132-2143.

[13]   a) K. Shiraishi, R. Endoh, H. Furuhata, M. Nishihara, R. Suzuki, K. Maruyama, Y. Oda, J. Jo, Y. Tabata, J. Yamamoto, M. Yokoyama, *Int. J. Pharm.* **2011**, *421*, 379-387, b) M. Nishihara, K. Imai, M. Yokoyama, *Chem. Lett.* **2009**, *38*, 556-557.

[14]   T. G. Leighton, *The Acoustic Bubble*, Academic Press **1994**.

7. APPENDICES

Research Paper

Nanodroplet-Mediated Histotripsy for Image-guided Targeted Ultrasound Cell Ablation

Eli Vlaisavljevich[1], Yasemin Yuksel Durmaz[1], Adam Maxwell[2], Mohamed ElSayed[1,3✉], Zhen Xu[1,4✉]

1. Department of Biomedical Engineering, University of Michigan, Ann Arbor, MI, USA;
2. Department of Urology, University of Washington School of Medicine, Seattle, WA, USA;
3. Macromolecular Science and Engineering Program, University of Michigan, Ann Arbor, MI, USA;
4. Department of Pediatrics and Communicable Diseases, Division of Pediatric Cardiology, University of Michigan, Ann Arbor, MI, USA.

✉ Corresponding author: Mohamed E.H. ElSayed, Ph.D. University of Michigan, Department of Biomedical Engineering, 1101 Beal Avenue, 2150 Lurie Biomedical Engineering Building, Ann Arbor, MI 48109, USA. Phone: + 1 (734) 615-9404 Fax: + 1 (734) 647-4834 E-mail: melsayed@umich.edu Web: www.bme.umich.edu/centlab.php OR Zhen Xu, Ph.D. University of Michigan, Department of Biomedical Engineering, 2107 Carl A. Gerstacker Building, 2200 Bonisteel Boulevard, Ann Arbor, MI 48109, USA. Phone: + 1 (734) 647-4961 Fax: + 1 (734) 939-1905 E-mail: zhenx@umich.edu Web: www.bme.umich.edu/labs/xulab.

Abstract

This paper is an initial work towards developing an image-guided, targeted ultrasound ablation technique by combining histotripsy with nanodroplets that can be selectively delivered to tumor cells. Using extremely short, high-pressure pulses, histotripsy generates a dense cloud of cavitating microbubbles that fractionates tissue. We hypothesize that synthetic nanodroplets that encapsulate a perfluoropentane (PFP) core will transition upon exposure to ultrasound pulses into gas microbubbles, which will rapidly expand and collapse resulting in disruption of cells similar to the histotripsy process but at a significantly lower acoustic pressure. The significantly reduced cavitation threshold will allow histotripsy to be selectively delivered to the tumor tissue and greatly enhance the treatment efficiency while sparing neighboring healthy tissue. To test our hypothesis, we prepared nanodroplets with an average diameter of 204±4.7 nm at 37°C by self-assembly of an amphiphilic triblock copolymer around a PFP core followed by cross-linkage of the polymer shell forming stable nanodroplets. The nanodroplets were embedded in agarose tissue phantoms containing a sheet of red blood cells (RBCs), which were exposed to 2-cycle pulses applied by a 500 kHz focused transducer. Using a high speed camera to monitor microbubble generation, the peak negative pressure threshold needed to generate bubbles >50 μm in agarose phantoms containing nanodroplets was measured to be 10.8 MPa, which is significantly lower than the 28.8 MPa observed using ultrasound pulses alone. High speed images also showed cavitation microbubbles produced from the nanodroplets displayed expansion and collapse similar to histotripsy alone at higher pressures. Nanodroplet-mediated histotripsy created consistent, well-defined fractionation of the RBCs in agarose tissue phantoms at 10 Hz pulse repetition frequency similar to the lesions generated by histotripsy alone but at a significantly lower pressure. These results support our hypothesis and demonstrate the potential of using nanodroplet-mediated histotripsy for targeted cell ablation.

Key words: Histotripsy, nanodroplets, cavitation, therapeutic ultrasound, targeted cell ablation.

Introduction

Many tumor types exhibit characteristically permeable vasculature with average endothelial gaps typically between 200-600 nm and show poor lymphatic drainage, which is collectively known as the enhanced permeation and retention (EPR) effect [1-4]. To take advantage of the EPR effect, phase change

nanodroplets have been shown to extravasate across tumor's leaky vasculature and enter the interstitial space to directly target cancer cells [5-11]. Nanodroplets encapsulate a perfluorocarbon (PFC) core that is stabilized by albumin, lipid, or polymer shells [5-8]. The PFC core typically has a boiling point lower than 37°C, but nanodroplets remain in the liquid form at body temperature [12-14]. After passing through the leaky microvasculature to a tumor's interstitial space, these nanodroplets can be vaporized by ultrasound to form gas bubbles through acoustic droplet vaporization (ADV) [12-14]. Attachment of optimal targeting ligands allows nanodroplets to specifically bind to cancer cells [12, 14, 15]. Research has shown the use of nanodroplets and ADV for targeted imaging [10, 14-17], drug delivery [10, 11, 14-17], and induce cavitation to enhance ultrasound thermal therapy [18-20].

One of the biggest limitations for current nanodroplet-mediated drug delivery or ultrasound thermal therapy is that nanodroplets (100–600 nm in diameter) cannot penetrate deep into the tumor tissue to reach the core after permeating across tumor's leaky vasculature. Therefore, their therapeutic utility in facilitating drug delivery or ultrasound thermal therapy by forming gas bubbles is greatly limited.

To overcome this major limitation, we started working on combining PFC-encapsulated nanodroplets with histotripsy, which is a new, non-invasive, image-guided, ultrasound ablation method [21-25]. Histotripsy uses extremely high pressure, microseconds long pulses to generate a cluster of microbubbles (bubble cloud) from pre-existing gas pockets in the tissue where the rapid expansion and collapse of the microbubbles disrupts cells [22, 23, 25]. We hypothesize that combining histotripsy with PFC-encapsulated nanodroplets will cause the ultrasound pulses to vaporize the nanodroplets delivered to the surface of the tumor nodules and form gas bubbles. Using the resulting gas bubbles as cavitation nuclei will significantly reduce the pressure threshold needed to generate and maintain the cavitation bubble cloud, which will fractionate the tumor nodules layer by layer until the entire tumor is destroyed. Whereas, the surrounding normal tissue without the nanodroplets will have a higher threshold and will be preserved from the histotripsy-induced fractionation. As such, even with nanodroplets diffusing only to regions next to tumor vasculature, targeted histotripsy will destroy the tumor core, overcoming the limitation caused by the shallow penetration depth of nanodroplets. This hypothesis is supported by our previous studies showing that once the cavitation bubble cloud is initiated, the histotripsy process can be maintained at a much

lower pressure than that needed for initiation [24]. The ability of histotripsy alone to erode a tissue layer by layer has been demonstrated in excised tissue samples [26] and *in vivo* large animal models [27, 28]. Further, the resulting gas bubbles can function as ultrasound contrast agents, which will allow the tumor sites to be seen on ultrasound imaging and allow the histotripsy treatment to be guided and monitored in real-time by ultrasound imaging. By employing an ultrasound transducer with a large focal zone, this technique could also achieve efficient treatment of tumors with multiple nodules.

Before a nanodroplet-mediated histotripsy approach can be investigated *in vivo*, nanodroplets must be synthesized with an optimum size (< 500 nm) that allows them to diffuse through the tumor vasculature [5-11]. Furthermore, these nanodroplets must be capable of reducing the pressure threshold to generate histotripsy bubbles and fractionate tissue. The goal of this study is to demonstrate the initial feasibility of nanodroplet-mediated histotripsy to set the foundation for future studies aimed at extending this technology to tumor ablation *in vivo*. We have synthesized an amphiphilic triblock copolymer that encapsulates PFC forming nanodroplets with an average diameter of ~200 nm. This ABC triblock copolymer is composed of a hydrophilic poly(ethylene glycol) (PEG) block, a central poly(acrylic acid) (PAA) block, and a random copolymer of heptadecafluorodecyl methacrylate (HDFMA) and methyl methacrylate (MMA) as the hydrophobic block. Nanodroplets are formulated using the PEG_{45}-*b*-PAA_{10}-*b*-$P(HDFMA_8$-*co*-$MMA_{21})$ copolymer that encapsulates perfluoropentane (PFP, boiling temperature 29°C) in the droplet's core. The PAA block is chemically cross-linked to "stitch" adjacent polymer chains forming a flexible polymer shell, which increases the stability of the formed nanodroplets. We hypothesized that our nanodroplets will remain stable at body temperature (37 °C) in the presence of serum proteins without an increase in their diameter above the size cutoff of tumor vasculature, which will allow them to extravasate into the tumor tissue *in vivo*.

In this report, we describe initial studies examining the ability to combine our nanodroplets with histotripsy to achieve efficient cell ablation in tissue-mimicking phantoms. We first simulated the peak negative pressure threshold needed to form a gas microbubble of 50 μm in diameter using an initial bubble nucleus of 5-500 nm in diameter and a single 2-cycle pulse with different frequencies. In previous histotripsy studies, microbubbles were generated and expanded to >50μm in diameter to produce cell disruption. This microbubble dynamic is different from other nanodroplet studies for targeted imaging and

drug delivery, and therefore requires substantially different acoustic parameters. Based on the simulation results, a 500 kHz focused transducer was used to apply a single 2-cycle ultrasound pulse, and the pressure threshold to acoustically vaporize the PFP encapsulated in the nanodroplet`s core and expand the resulting gas bubble to >50 μm was measured. We also examined the feasibility of using this technique to produce cavitation in selected regions and image the resulting bubbles with ultrasound imaging. Finally, we evaluated the ability of nanodroplets to fractionate red blood cells embedded in tissue-mimicking agarose gels when combined with a histotripsy pulse.

Experimental Section

Formulation and Characterization of Nanodroplets

We synthesized an ABC triblock copolymer composed of a hydrophilic poly(ethylene glycol) (PEG) block, a central poly(acrylic acid) (PAA) block, and a random copolymer of heptadecafluorodecyl methacrylate (HDFMA) and methyl methacrylate (MMA) as the hydrophobic block via a one-pot "click" reaction [29-31]. PEG_{45}-*b*-PAA_{10}-*b*-P(HDFMA$_8$-*co*-MMA$_{21}$) copolymers were used to prepare PFP-loaded nanodroplets following the procedure shown in **Figure 1**. Briefly, PEG_{45}-*b*-PAA_{10}-*b*-P(HDFMA$_8$-*co*-MMA$_{21}$) copolymers were dissolved in tetrahydrofuran (THF) (0.2% w/v) and cooled down to 0°C before the addition of PFP (2% v/v) while vigorously stirring the reaction mixture. An equal amount of water was slowly added to this solution mixture to trigger micelle formation and the mixture was stirred for 1h in an ice bath. The micelles solution was transferred into a dialysis bag (MWCO of 1 kDa) and dialyzed against ice-cold 2-(*N*-morpholino) ethanesulfonic acid (MES) solution or water to remove the THF. After 12 hours of dialysis, a slightly milky solution of PFP-loaded nanodroplets was observed. The PAA block was chemically cross-linked using 2,2`-(ethylenedioxy)-bis(ethylamine) as a cross-linker via NHS/EDC coupling chemistry [32-34] to form a flexible polymer shell that stabilizes the nanodroplets but allows acoustic droplet vaporization to form microbubbles. Selection of ideal polymer composition and PFP content used in this study has been optimized in a separate investigation [30, 31].
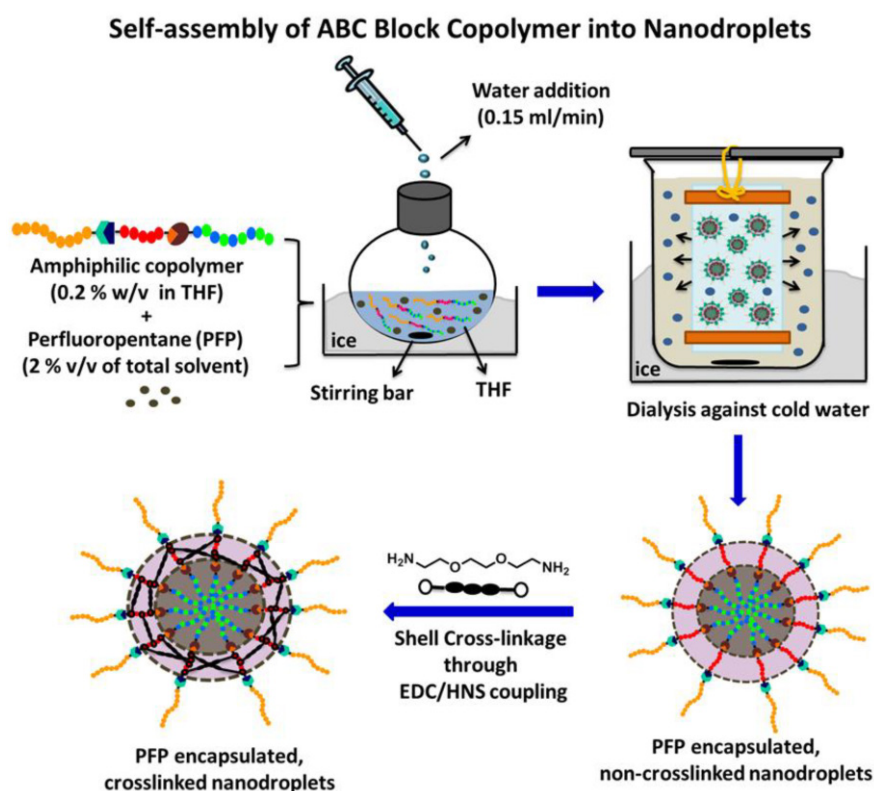

Fig 1. Formulation of PFP-loaded nanodroplets by self-assembly of amphiphilic triblock PEG_{45}-*b*-PAA_{10}-*b*-P(HDFMA$_8$-*co*-MMA$_{21}$) copolymer around the PFP core followed by shell cross-linkage via EDC/HNS coupling reactions.

Nanodroplet concentration and size distribution were characterized using Nanoparticle Tracking Analysis (NTA). Measurements were obtained using a NanoSight NS500 (NanoSight Ltd., Amesbury, United Kingdom), equipped with an LM14 (405 nm laser), high sensitivity EMCCD Andor Luca camera and a syringe pump. Upon dilution to the appropriate NTA concentration with DI Water (MilliQ, 18MΩ), both capture and analysis were carried out using the NTA software (Version 2.3, Build 0027) at 22°C and 37°C. The samples were measured by capturing 60 s videos (6 videos per each sample). The error bars represent the standard deviation of the repeat measurements of each sample. The mean size and standard deviation values obtained by the NTA software correspond to arithmetic values calculated with the sizes of all particles analyzed for each sample (n = 6).

Biocompatibility of Nanodroplets

Toxicity of the PEG$_{45}$-*b*-PAA$_{10}$-*b*-P(HDFMA$_8$-*co*-MMA$_{21}$) copolymer used to formulate the nanodroplets was investigated as a function of polymer concentration using the MTT assay (EMD Millipore, Billerica, MA). Briefly, human prostate cancer cells (PC-3) were seeded at a seeding density of 1×10^5 cells/well in 96-well plates and allowed to adhere overnight before replacing the culture medium with phenol red-free RPMI 1640 medium solution containing 0.3, 1.5, 15, 30 and 75 µg/mL of the PEG$_{45}$-*b*-PAA$_{10}$-*b*-P(HDFMA$_8$-*co*-MMA$_{21}$) copolymer formulated into PFP-loaded nanodroplets with an average diameter of ~200 nm, which corresponds to droplets concentrations of 2.06x10^8, 1.03x10^9, 1.03x10^{10}, 2.06x10^{10}, 5.15x10^{10} particles/mL, respectively. The nanodroplets solution was aspirated after incubating for 24 hours under normal culture conditions followed by adding 10 µL of the MTT reagent to each well and incubating for 2 hours according the manufacturer's guidelines to allow enough time for the formation of the purple formazan precipitate. A 100 µL of the detergent solution was added to each well and incubated for 3 hours in the dark at room temperature before measuring the UV absorbance at 570 nm using a Multiskan microplate reader (Thermo Fisher Scientific Inc., Waltham, MA). PC-3 cells incubated with blank RPMI1640 culture medium and 5% v/v Triton X-100 solution were used as negative and positive controls, respectively. The statistical difference in UV absorbance between RPMI1640-treated cells (negative control) and those incubated with different concentrations of the copolymer was evaluated using student's *t*-test where p < 0.05 indicated a statistically significant difference in cell viability.

Threshold Simulation for Nanodroplet-Mediated Cavitation

A numerical simulation based on a modified Keller-Miksis equation for soft-tissue bubble dynamics [35, 36], was performed to estimate the relationship between frequency and bubble expansion for nanodroplet-mediated histotripsy with nanodroplets of 5-500 nm diameter. The peak negative pressure to expand initial bubbles of 5-500 nm diameters into 50 µm diameter bubbles was determined. Vaporization was not accounted for in this simulation, but the P-thresholds to achieve this bubble expansion are expected to be sufficiently high to vaporize the nanodroplets based on the literature [12, 37].

The simulation computed the bubble radius vs. time in response to a driving pressure waveform by

$$\left(1-\frac{\dot{R}}{c}\right)R\ddot{R}+\left(1-\frac{\dot{R}}{3c}\right)\frac{3}{2}\dot{R}^2 = \left(1+\frac{\dot{R}}{c}\right)\frac{p_w(\dot{R},R,t)}{\rho}+\frac{R}{\rho c}\frac{\partial p_w}{\partial t}$$

…(1)

where R is the bubble radius, the dot indicates a derivative with respect to time, c is the sound speed, ρ is the medium density, and p_w is the pressure at the bubble wall in the medium surrounding the bubble, defined as

$$p_w\left(\dot{R},R,t\right)=\left(p_0 - p_v + \frac{2\sigma}{R_0}\right)\left(\frac{R_0}{R}\right)^{3\kappa} - p_0 - \frac{2\sigma}{R} - \frac{4G}{3R^3}\left(R^3 - R_0^{\ 3}\right) - \frac{4\mu\dot{R}}{R} - p_a(t)$$

…(2)

In Eq. 2, p_0 and p_v are the ambient and vapor pressure, respectively, σ is surface tension, R_0 is the initial bubble radius, κ is the polytropic index, G is the shear modulus, μ is the dynamic viscosity, and $p_a(t)$ is the acoustic driving pressure. The tissue Young's modulus ($E \sim 3G$) and μ were chosen to match the agarose tissue phantom properties used in this study (E = 38 kPa and μ = 0.05 Pa-s), which were within the property range of hepatocellular carcinoma (E = 20.4–75 kPa), metastatic liver tumors (E = 23.6–75 kPa), and prostate cancer tissue (E = 24 kPa) [38, 39]. The surface tension (σ) was estimated for soft tissue as σ = 54 mN/m [40]. Other properties were selected to match values for water at 20°C.

The pressure waveform for the simulation employed an analytical pulse model [41] to create a 2-cycle, asymmetric pulse with a similar P_+/P_- to that in Figure 2. The pressure is given as

$$p_a(t) = p_f \sum_{k=1}^{\infty}\left[\frac{\sin\left(k\omega(t-\tau)+\phi\right)}{k}\right]\cdot\exp\left[-\left(\frac{t-\delta}{\xi}\right)^2\right]$$

…(3)

where p_f is the fundamental pressure amplitude, ω is the radial frequency, τ is the starting phase, ϕ is a phase shift to create waveform asymmetry, δ is the

time delay to the center of the pulse, and ξ defines pulse duration. The waveform at 0.5 MHz, $\omega = 3.14 \times 10^6$ rad/s, $\tau = 1.25 \, \pi \, / \, \omega$, $\phi = -\pi/4$, $\delta = 6.3$ µs, and $\xi = 2.6$ µs. The simulation was also performed at $f = 0.2$ and 1.1 MHz, scaling the above parameters to maintain the same waveform shape.

Ultrasound Setup

Ultrasound pulses were generated by two 500 kHz focused ultrasound transducers built in house. The two transducers were fabricated using rapid prototyping technology and contained 32 and 7 elements, respectively. Each module consists of a 2 inch (50.8 mm) diameter lead zirconate titanate (PZT) disc element coupled to an elliptical acoustic lens through a quarter wavelength matching layer. Transducer shells contained threaded receptacles populated with individual element modules. The 32 element transducer had an aperture diameter of 300 mm, a focal distance of 150 mm, and a focal zone (Measured -6 dB Pressure) of 1.8 x 3.9 mm. The 7 element transducer had an aperture diameter of 200 mm, a focal distance of 150 mm, and a focal zone (Measured 6 dB Pressure) of 3.4 x 20.7 mm. A field-programmable gate array (FPGA) was used as a custom pulse generator to electronically control each channel (Altera Corp., San Jose, CA). The FPGA was connected to a 32-channel bank of high voltage pulsers developed in-house.

Acoustic waveforms produced by the 500 KHz therapeutic transducer (**Figure 2A**) were obtained using a fiber optic probe hydrophone built in house [42]. Pressure wave measurements were recorded in free-field in degassed water at room temperature. At higher pressures above the histotripsy cavitation threshold, pressure could not be accurately measured due to instantaneous cavitation at the fiber tip. These higher pressure levels were estimated as a summation of the pressures generated by the individual elements, which were sparsely distributed without a significantly overlapping beam and closely matched the predicted values using a linear extrapolation of the lower pressure values measured with all elements. The 7 element transducer was used for the selective cavitation generation experiment, because the larger focal region of this transducer was needed for that experiment set. The 32 element transducer was used for all other experiments, as it is capable of generating high pressure beyond the intrinsic threshold. Cavitation bubbles were optically imaged using a high-speed, 1 megapixel CCD camera, (Phantom V210 - Vision Research, Wayne, New Jersey, USA) (**Figure 2B**). The camera was focused through a macro lens (Tominon 105 mm f/4.5 Kyocera Corp., Japan) and folding optical bellows (Nikon Corp., Japan).
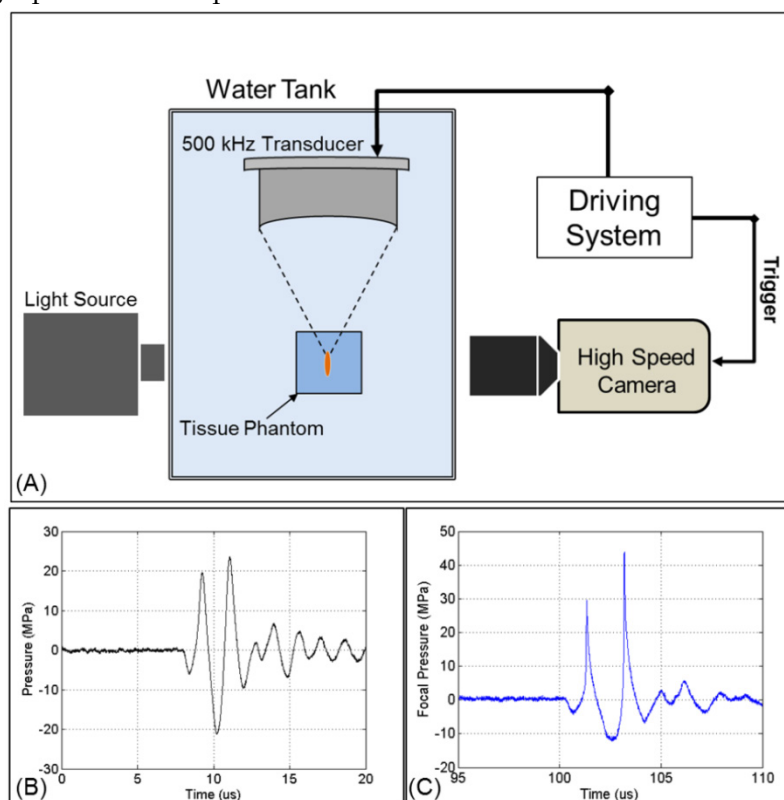

Fig 2. Acoustic waveform and experimental setup. (A) The focus of one of the 500 kHz transducers was aligned inside tissue phantoms containing nanodroplets. Cavitation was monitored using high speed optical imaging. Example of a 2-cycle histotripsy pulse generated by the (B) 32 element and (C) 7 element transducers.

Preparation of Tissue Phantoms

Agarose phantoms were used to provide a well-controlled viscoelastic medium for this study, as histotripsy-induced damage is highly dependent on the tissue mechanical properties. Tissue phantoms containing 1% agarose w/v were prepared by slowly mixing agarose powder (Agarose Type VII, Sigma-Aldrich, St. Louis, MO) into saline solution (0.9% sodium chloride, Hospira) heated to above 70°C while stirring until the gel became completely transparent. Agarose solutions were degassed under a partial vacuum of 20.5 mmHg for 30 minutes before allowing the agarose solutions to cool down to 37°C. Phantoms containing nanodroplets were prepared by slowly adding the nanodoplets (2.36×10^8 particles/mL) into the agarose solution while stirring. The agarose mixtures were poured into rectangular polycarbonate holders and placed in a refrigerator at 4°C to allow the solution to solidify forming tissue phantoms with embedded nanodroplets (test) or without nanodroplets (control). The Young's modulus of the tissue phantom was 38kPa [43], which is within the range of the Young's modulus of hepatocellular carcinoma tumors (20.4–75 kPa), metastatic liver tumors (23.6–75 kPa), and prostate tumors (24 kPa) [38, 39]. Tissue phantoms were warmed prior to use and maintained at 37°C for the duration of all experiments performed in this work.

For cell fractionation experiments, tissue phantoms with a red blood cell (RBC) layer were prepared using canine RBCs in 0.9% isotonic saline and 1% agarose solutions with and without nanodroplets. Fresh canine blood was obtained from adult research subjects in an unrelated study and added to an anticoagulant solution of citratephosphate-dextrose (CPD) (Sigma-Aldrich Co., St. Louis, MO) with a CPD-to-blood ratio of 1:9 mL. Whole blood was separated in a centrifuge at 3000 rpm for 10 min. The plasma and white buffy coat were removed, and the RBCs were saved for addition to the phantom. To prepare the RBC phantom, an initial layer of 1% agarose mixture (with and without nanodroplets) was poured into a rectangular polycarbonate housing to fill half of it at 37°C. The housing was placed in a refrigerator at 4°C to allow the agarose to cool and solidify. The remaining solution was kept at 37°C. A small amount of agarose solution was mixed with the RBCs (5% RBCs v/v). The frame with solidified agarose was removed from refrigeration, and a thin layer of the RBC-agarose solution was poured onto the gel surface to allow the entire surface to coat in a thin layer. After 5 min, the RBC-agarose layer was solidified, and the remaining agarose solution without RBCs was poured to completely fill the frame. This procedure created a thin layer of RBCs suspended in the center of the agarose phantom.

Measurement of Histotripsy Threshold in Agarose Tissue Phantoms

The pressure threshold to form and expand microbubble to >50 μm diameter using a single 2-cycle ultrasound pulse was recorded in agarose tissue phantoms with and without nanodroplets. To determine the cavitation threshold, the ultrasound pulse was applied to the center of tissue phantoms with and without nanodroplets using the 32 element 500 kHz transducer at pressures ranging from 2–40 MPa. The sample size was 100 pulses for each pressure level by applying 100 pulses separated by 10 sec between pulses (i.e., pulse repetition frequency (PRF) of 0.1 Hz), to provide adequate time for any residual nuclei from the bubble collapse by the previous pulse to dissolve. In this way, each of the 100 pulses was expected to generate cavitation independently without influence from the previous pulses. To evaluate the threshold variation using different nanodroplet formulations in different phantoms, this process was repeated using nanodroplets synthesized on 3 different occasions each evaluated using two tissue phantoms (total n=6) using 100 pulses at each pressure level.

Cavitation was monitored using high-speed optical imaging (**Figure 2**). A high-speed V210 camera (Vision Research, Wayne, NJ) was used to capture images of the focal zone directly after the propagation of each pulse through the focus in the phantoms. The camera was focused with a macro-bellows lens (Tominon, Kyocera, Kyoto, Japan) through the optical window of the chamber to observe the focal region. The camera was backlit by a continuous light source to produce shadowgraphic images of cavitation bubbles. The camera was triggered to record one image for each pulse applied, 10–40 μs after the beginning of the pulse reached the focal center. The timing was actively adjusted at each pressure level to coincide with the maximal bubble expansion occurrence. This process ensured that the pressure pulse had passed over the entire focal volume at the time of capture and the bubbles were imaged at the point of maximal expansion. The camera exposure time was 2 μs for all images. After acquisition, images were converted from grayscale to binary by an intensity threshold determined based on the background intensity of the shadowgraphs in image-processing software (Matlab; The Math-Works, Natick, MA, USA). The events when a bubble was expanded to >50μm within the focus were analyzed and recorded for each pressure level because such bubble expansion was shown in histotripsy to achieve tissue fractionation. The num-

ber of pulses (out of 100) in which one or more such cavitation events was observed to occur was recorded for each sample as the cavitation probability (P_{cav}). The average cavitation probability at each pressure level for the six samples was plotted for tissue phantoms containing nanodroplets as well as control phantoms without nanodroplets with the error bars representing the standard deviation. An interpolation fit was performed on the plot in Matlab to calculate the P- threshold, which was considered to be the point at which 50% of the pulses generated cavitation bubbles >50 um (i.e. P_{cav}=0.50). The P- threshold was calculated for each sample (n=6) and reported as the mean ± the standard deviation. The minimum pressure level at which any cavitation bubbles >50 μm were observed was similarly analyzed and reported as the mean ± the standard deviation. Finally, the difference between P_{cav}=0.15 and P_{cav}=0.85, a relative measure of the steepness of the transition from P_{cav}=0 to P_{cav}=1 was calculated and reported as the mean ± the standard deviation for phantoms containing nanodroplets as well as histotripsy only controls.

Selective Cavitation in Composite Agarose Phantom

Using a focal zone covering multiple sub-regions loaded with the nanodroplets adjacent to other sub-regions without the nanodroplets, we hypothesized that cavitation can be selectively generated only in the sub-regions containing the nanodroplets by applying ultrasound at an acoustic pressure that is above the cavitation threshold with nanodroplets but below the cavitation threshold using histotripsy alone. To test this hypothesis, we prepared agarose phantoms containing hexagonal inclusions that were the only regions within the gel loaded with the nanodroplets. Briefly, composite tissue phantoms were prepared by pouring 1% agarose solution into a rectangular polycarbonate housing before submerging and fixing eight 6.5 mm thick hexagonal inclusions inside the phantom. The phantom with the inclusions was placed in a refrigerator at 4°C to allow the agarose to solidify. After the agarose solution solidified, the hexagon inclusions were removed from the tissue phantom leaving hexagonal voids that were then filled with 1% agarose solution containing the nanodroplets at a concentration of 3.0×10^8 particles/mL. This procedure created a tissue phantom with hexagonal "islands" containing nanodroplets surrounded by an agarose gel without nanodroplets. Subsequently, the focus of the 7 element transducer was aligned to cover two of the nanodroplets-containing hexagons and the agarose gel without nanodroplets between them. Histotripsy pulses were applied to the focus at a PRF of 10 Hz at a peak nega-

tive pressure of 17.3 MPa. The resulting cavitation bubbles were monitored by high-speed optical imaging. Additionally, cavitation bubble generation was monitored by a clinical ultrasound imaging system (HDI 5000 Ultrasound system).

Bubble Behavior

To determine if nanodroplet-mediated cavitation bubbles exhibited similar expansion and collapse behavior to histotripsy bubbles, optical images of the growth and collapse of bubbles were recorded by the high-speed camera. Nanodroplet-mediated cavitation bubbles were generated by the 32 element 500 kHz transducer at a peak negative pressure of 15.6 MPa. This pressure level was selected because it is lowest pressure at which a cavitation cloud was always generated using a 2-cycle ultrasound pulse in tissue phantoms with nanodroplets. The expansion and collapse behavior of bubbles was reconstructed from a series of bubble clouds imaged at different time delays after the pulse. Ten pulses were applied to agarose tissue phantoms containing nanodroplets at each time delay at a PRF of 1 Hz. The focus was then moved to a different location within the tissue phantom and camera delay was increased 3 μs. Delay intervals of 0–60 μs were used to reconstruct a sequence of bubble images covering the entire period of bubble expansion and collapse. Shadowgraph images were converted from grayscale to binary by an intensity threshold determined by the background intensity using image processing software (Matlab, The Mathworks). Bubbles were indicated by black regions >5 pixels. The minimum resolvable diameter of a bubble using this minimum 5-pixel area was approximately 15 μm. The average diameter of 10 bubbles visible within the focus was measured for each pulse at each time delay. A sample size of 10 pulses was used for each time delay and the average bubble size ± the standard deviation was plotted as a function of time.

Ablation of Red Blood Cells in Tissue Phantom

Agarose gel phantoms with an embedded RBC layer were used to characterize cell fractionation induced by nanodroplet-mediated histotripsy. Fractionation of the RBCs turns the color of the embedded cell layer from opaque red to translucent as the RBCs were lysed, which allows direct visualization of the histotripsy-induced fractionation process [44]. Previous studies have also shown that the lesion visualized in RBC phantoms is similar to the lesion generated in tissue identified by histology [44]. The focus of the 32 element 500 kHz transducer was aligned with the center of the red blood cell phantom layer and 2000 histotripsy pulses were applied at a PRF of 10 Hz at

peak negative pressures of 6.2 MPa, 11.0 MPa, 15.9 MPa, and 20.7 MPa with and without nanodroplets (n=6). The bubble cloud and resulting cell fractionation was recorded by high-speed optical imaging after each pulse (**Figure 2**). The high-speed camera (Phantom V211, Vision Research) was focused to the red blood cell layer and backlit by a continuous light source. The camera was triggered to record two images for each applied pulse, one 10 μs after the pulse reached the focus to visualize the bubble activity and another frame between pulses, 50 ms after each pulse, to assess tissue damage. The camera exposure time was 10 μs. The bubbles appeared as black regions in the shadowgraphic image and RBC fractionation was visualized as RBCs turn transparent after fractionation. Cell fraction was compared between RBC phantoms with nanodroplets and control RBC phantoms without nanodroplets. Shadowgraph images were converted from grayscale to binary by an intensity threshold determined by the background intensity using image processing software (MATLAB, The Mathworks) and the lesion area after 2000 pulses was calculated by summing the pixels within the fractionated region.

Results and Discussion

Nanodroplets Formulation and Biocompatibility

Results show that PEG$_{45}$-*b*-PAA$_{10}$-*b*-P(HDFMA$_8$-*co*-MMA$_{21}$) copolymer successfully encapsulated PFP (2% v/v) forming nanodroplets with an average diameter of 192±4.6 nm and 204±4.7 nm at 22°C and 37°C, respectively. **Figure 3A** is a representative image showing the size distribution for a single sample of nanodroplets in the range of 100–400 nm with >99% of the nanodroplets smaller than 400 nm and <0.01% larger than 600 nm. The peak of the size distribution is 128.5 ± 9.1 nm and 138.5 ± 8.0 nm at 22°C and 37°C, respectively. The similar size distribution at 22°C and 37°C indicates that the encapsulated PFP core remained as a liquid at the body temperature (37°C) and did not change into a gas, which is consistent with previous studies [12-14]. The observed control over the size and shape of the formed nanodroplets is a result of the fine control over the length, molecular weight, and composition of the amphiphilic polymer used to formulate these nanodroplets [45, 46]. Specifically, the PAA and P(HDFMA-*co*-MMA) blocks in the amphiphilic PEG$_{45}$-*b*-PAA$_{10}$-*b*-P(HDFMA$_8$-*co*-MMA$_{21}$) copolymer were synthesized via atom transfer radical polymerization (ATRP), which allows fine control over the length, composition, and functionality of the formed blocks [45] [47].
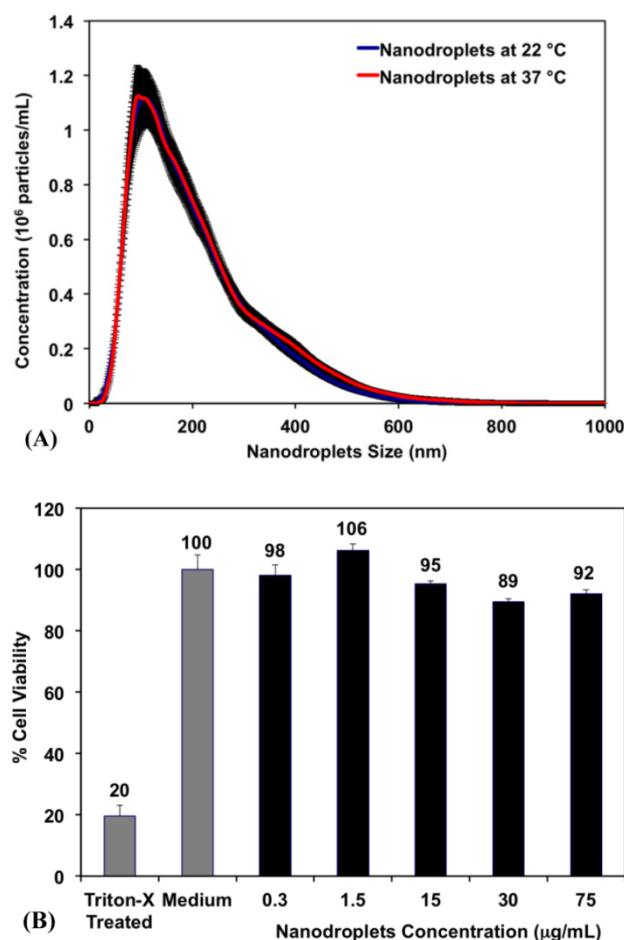

Fig 3. (A) A representative image showing the size distribution of PFP-loaded nanodroplets. Results show an average nanodroplet size of approximately 200 nm with the peak of the size distribution at 128.5 ± 9.1 nm and 138.5 ± 8.0 nm at 22°C and 37°C, respectively. (B) MTT results show no significant change in the viability of PC-3 cells incubated with 0.3, 1. 5, 15, 30 and 75 μg/mL of the triblock copolymer used to formulate the PFP-loaded nanodroplets compared to PC-3 cells incubated with blank culture medium.

Research showed that self-assembled polymeric micelles tend to disassemble at higher temperatures and upon dilution to concentrations below their critical micelle concentration [45]. Nanodroplets with polymer, lipid, and protein shells have also been shown to coalesce forming larger microbubbles, which limits their ability to diffuse across tumor vasculature *in vivo* [48]. Therefore, we relied on covalent chemical cross-linkage of the polymer shell to increase nanodroplets stability against physiological shear stress *in vivo* and maintain the size, shape and concentration of the nanodroplets. Our results show that nanodroplets' concentration at 22°C (3.07 x 10^{10} particles/mL) did not change upon increasing the solution temperature to 37°C (3.00 x 10^{10} particles/mL) (**Figure 3A**), which is critical for the success of the envisioned ablation approach as the number of cavitation nuclei is directly proportional to the number of stable nanodroplets present at tumor site. The initial testing

of stability and biocompatibility of these nanodroplets is promising. Further, the size range of our nanodroplets should allow them to preferentially diffuse through the leaky tumor vasculature while preventing diffusion through normal blood vessels [1-4]. In addition, this nanodroplet design allows the covalent attachment of different targeting ligands to the free end of the PEG block allowing the incorporation of a "tunable" number of targeting motifs on the droplets surface. These targeted nanodroplets will allow selective binding to cancer cells, which should increase droplets concentration and retention in the tumor tissue.

Research shows that 90% of the PFP concentration in the blood can be eliminated from the body within 10 minutes after their administration, which diminishes the risk of toxicity [49]. Therefore, we investigated the toxicity of the PEG$_{45}$-*b*-PAA$_{10}$-*b*-P(HDFMA$_8$-*co*-MMA$_{21}$) polymer used to formulate the nanodroplets as a function of polymer concentration using the MTT assay. Results show that there was no change in the number of viable PC-3 cells upon incubation with the PFP-loaded nanodroplets for 24 hours up to a polymer concentration of 75 µg/mL (5.15x10^{10} droplets/mL) compared to the negative control (p>0.05) (**Figure 3B**). This is a significant finding given that the highest reported nontoxic concentration of nanodroplets that were formulated using PEG-lipid conjugates is 2.5x10^8 droplets/mL[50], which is 200-fold lower than the nanodroplets concentration used in our study. These results collectively indicate the ability to reproducibly formulate stable nanodroplets that are nontoxic to mammalian epithelial cells at high concentrations up to 5.15x10^{10} particles/mL.

Threshold Simulation for Nanodroplet-Mediated Cavitation

In a previous histotripsy study, the threshold to generate cavitation using a single, µs-length pulse in multiple tissues and tissue-mimicking media was measured to be 26–30 MPa peak negative pressure [36]. At the high pressure above 26 MPa, cavitation bubbles are generated from pre-existing gas pockets in the tissue <10 nm in size and expanded to >50 µm followed by energetic collapse, all within a hundred µs. This energetic bubble activity disrupts adjacent cells and eventually produces complete fractionation of cells in the target tissue into a liquefied homogenate. To determine the effects of nanodroplets on reducing the peak negative pressure (P-) threshold to generate and expand microbubbles to >50 µm, a numerical simulation based on a modified Keller-Miksis equation for soft-tissue bubble dynamics as outlined in a previous study [36] was performed using initial

gas bubbles 5–500 nm in diameter. We will refer to this threshold as the "histotripsy threshold" in this paper to distinguish from cavitation threshold commonly referred in the literature, which is often observed to be at much lower pressure levels with the presence of nuclei on the order of microns and/or using much longer pulses [51, 52]. The simulation used a 2-cycle pulse and compared frequencies of 0.2, 0.5, and 1.1MHz. The simulation showed that the histotripsy threshold increased substantially with increasing frequency (**Figure 4**). For example, the histotripsy threshold using an initial 200 nm bubble was 1.7, 6.3, and 21.3 MPa at 0.2, 0.5, and 1.1 MHz, respectively. Using an initial gas bubble at a diameter of 200 nm and above, there was no significant change in the threshold for the same frequency, whereas using a 100 nm initial nucleus, the histotripsy threshold was higher. The initial bubble size mattered little in the 200–500 nm range because the pressure amplitude to achieve 50 µm max radius is much larger than the inertial cavitation threshold for bubbles this size. In this case the bubble motion is dominated by inertia, which leads to bubbles expanding to approximately the same size regardless of initial radius. Nanodroplet vaporization was not accounted for in this simulation, but P- thresholds are expected to be sufficiently high to vaporize the nanodroplets based on the literature [12, 37].
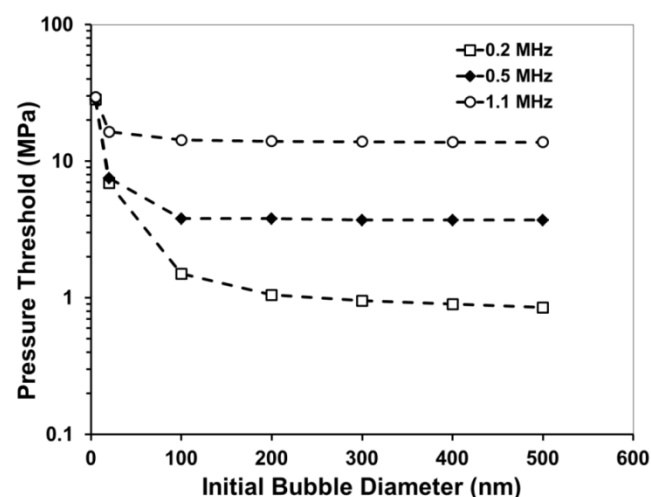

Fig 4. A plot showing the simulated peak negative pressure (P-) threshold to expand a bubble from an initial diameter of 5–500 nm to 50 µm in tissue.

These results suggest that a lower frequency (≤500kH) would be better suited to use for nanodroplet-mediated histotripsy, as it results in a significantly lower histotripsy threshold. This dependence is opposite to a previous study by Kripfgans et al. using micron-sized droplets, where they found the pressure threshold to vaporize the droplets decreased with increasing frequency [13]. In compari-

son, we used much smaller droplets and measured the threshold to expand the bubbles resulting from vaporized droplets to >50µm. It is likely that a different mechanism is responsible for our study. The trend of decreasing threshold with decreasing frequency is consistent with the frequency dependency in inertial cavitation, which we plan to investigate as a potential mechanism for nanodroplet-mediated histotripsy.

Using a lower frequency offers multiple advantages for ablation therapy. First, as the transducer focal zone scales with the wavelength, a low frequency transducer will yield a large focal zone, allowing histotripsy to be applied simultaneously to cover multi-nodule tumors seeded with our nanodroplets, thus increasing the treatment efficiency for multiple tumor nodules. With the reduced threshold at the tumor nodules with nanodroplets, only tumors will be treated while preserving surrounding normal tissue. Lower frequency is also more resistant to acoustic aberration and attenuation from bone obstruction and long overlying tissue, resulting in deeper penetration depth.

Measurement of Histotripsy Threshold in Agarose Tissue Phantoms

In order to validate the simulation results, the pressure threshold to vaporize the nanodroplets and expand the resulting bubbles >50 µm was measured in tissue-mimicking agarose phantoms with and without nanodroplets. Based on the analysis of high-speed images, results demonstrated a significant decrease in the histotripsy threshold with nanodroplets compared to histotripsy only controls. The minimum pressure level at which cavitation bubbles >50 µm was observed by high speed images to be 3.02±2.49 MPa for phantoms containing

nanodroplets and 15.60±2.35 MPa for histotripsy only controls without nanodroplets (**Figure 5**). The pressure level at which 50% of the 100 pulses generated cavitation bubbles >50 µm, P_{cav} = 0.50, was found to be 10.77±0.32 MPa with nanodroplets compared to 28.79±0.47 MPa without nanodroplets (n=6). The difference between P_{cav}=0.15 and P_{cav}=0.85 was found to be 3.17±0.65 MPa and 2.14±0.41 MPa for phantoms with and without nanodroplets, respectively. At pressures ≥15.9 MPa, cavitation microbubbles were always observed (P_{cav} = 1). At pressure greater than 11MPa, the area of the bubble cloud increased with increasing pressure (**Figure 6**). For example, the lateral width of the bubble cloud was 1.1 mm, 2.0 mm, and 2.4 mm at peak negative pressures of 13.9 MPa, 15.9 MPa, and 20.7 MPa, respectively. These widths match closely with the lateral width of the focal zone where the pressure was above 11 MPa.
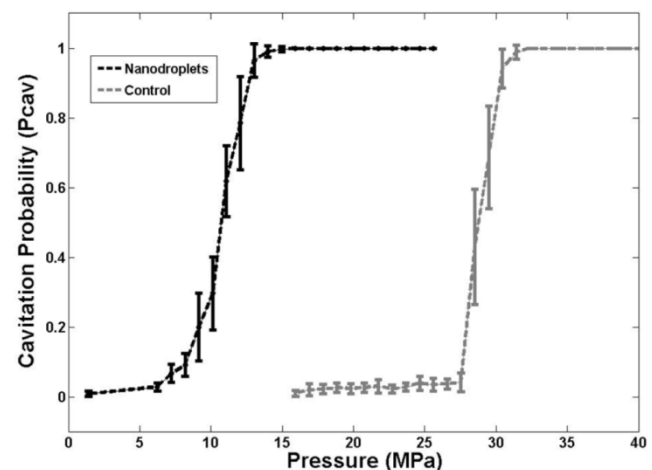

Fig 5. A plot showing the histotripsy threshold in agarose tissue phantoms with and without nanodroplets. Results demonstrated a significant decrease in the pressure threshold to generate cavitation bubbles >50 µm with nanodroplets compared to control conditions (histotripsy only).
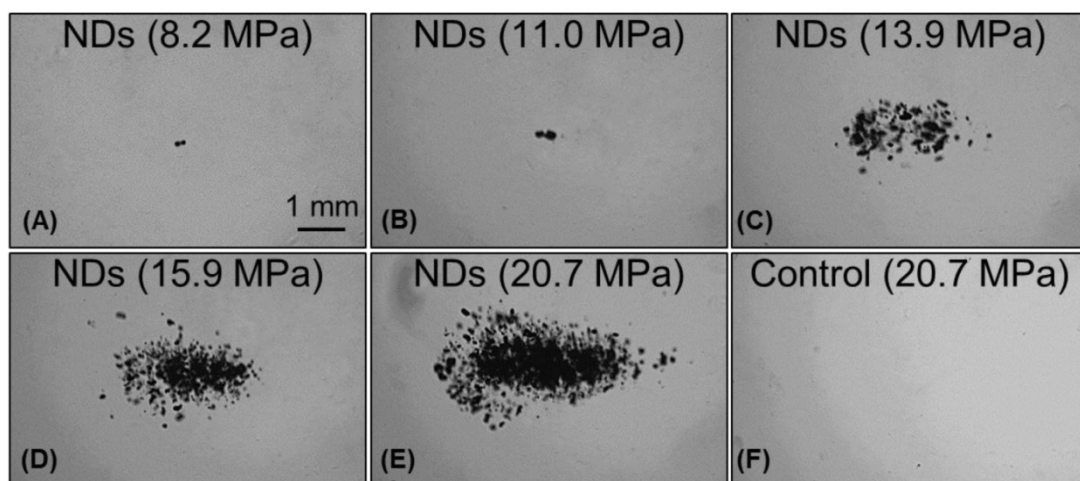

Fig 6. Images of nanodroplet-mediated cavitation in agarose tissue phantoms at increasing acoustic pressures. Images of cavitating bubble clouds (dark) generated using agarose phantoms containing nanodroplets at the pressure of 8.2–20.7 MPa (A–E). With increasing pressure, the area of the bubble cloud increased. In comparison, cavitation wasn't observed in control samples in this pressure range MPa (F).

The experimental results further support our hypothesis that histotripsy-induced cavitation bubble cloud can be formed at a significantly reduced pressure using nanodroplets, which is the basis to achieve selective tumor ablation using nanodroplet-mediated histotripsy. These experimental results also match well with the simulation. The simulation results showed a 200 nm initial nucleus and a single 500 kHz ultrasound pulse results in a histotripsy threshold of 6.3 MPa. Measured with the 500 kHz transducer and 200 nm nanodroplets, the histotripsy threshold was 9.01 ± 0.62 MPa at $P_{cav} = 0.15$ and 10.8 ± 0.3 MPa at $P_{cav} = 0.5$. The measured threshold was higher likely because droplet vaporization and the effects of the cross-linked polymer shell were not included in the simulation. Although the vaporization threshold wasn't measured in this work, the pressures used here are higher than the ADV threshold using similar sized nanodroplets reported in the literature [12-14]. While the pressure required to generate histotripsy bubbles using these nanodroplets was significantly lower than histotripsy alone, it is possible that the histotripsy threshold could be further reduced by using a lower boiling temperature PFC core, such as decafluorobutane (boiling temperature -1°C), which have been shown to vaporize at significantly lower pressure [14].

Selective Cavitation in Composite Agarose Phantom

Based on the reduced histotripsy threshold using nanodroplets, cavitation should be selectively generated in multi-tumor nodules with nanodroplets inside the focal zone, whereas no cavitation should be formed at normal tissue without nanodroplets. The feasibility of using nanodroplets to generate selective cavitation was investigated using a composite agarose tissue phantom. Histotripsy pulses were applied inside the composite agarose tissue phantom containing inclusions with nanodroplets. Using 2-cycle pulses at a peak negative pressure of 17.3 MPa, which is above the histotripsy threshold using nanodroplets and below the intrinsic threshold using histotripsy alone, cavitation bubble clouds were formed only in the inclusions containing nanodroplets located within the focal volume of the 500 kHz transducer (**Figure 7A**). Optical images indicated two separate dense cavitation clouds inside the nanodroplet-containing inclusions inside the focal region throughout the 2000 pulses while no bubbles were observed outside the inclusions within the focal region (**Figure 7B**). Correspondingly, ultrasound imaging showed two dynamically changing hyperechoic zones inside the hexagon inclusions, while no bubbles were observed elsewhere (**Figure 7C**). As these cavitation bubbles generated in the process are viewed clearly on ultra-

sound imaging, the histotripsy therapy process can be monitored and guided by ultrasound imaging in real-time.
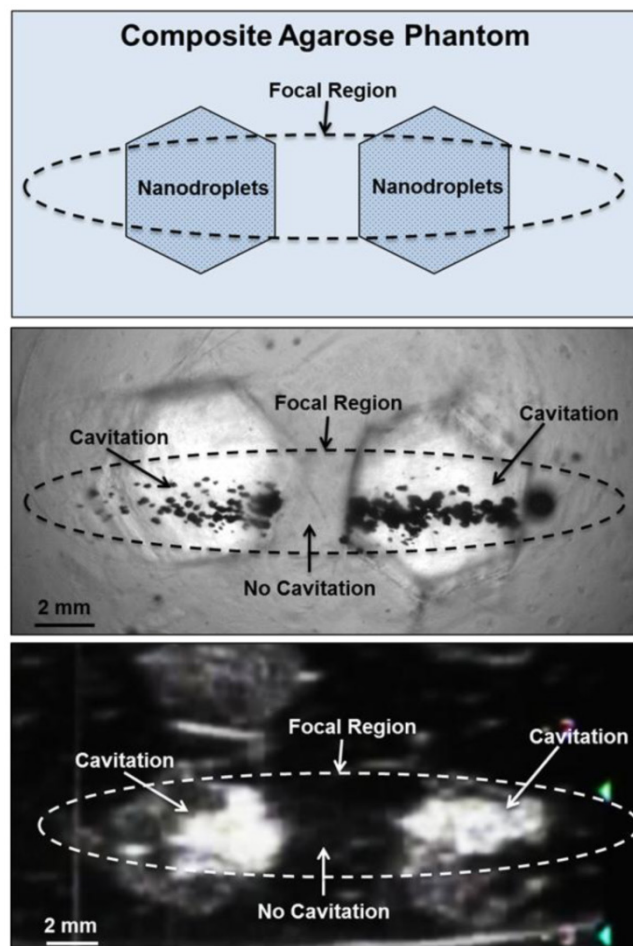

Fig 7. Selective cavitation in a composite agarose tissue phantom. Optical images (top) of agarose phantoms with hexagon shaped inclusions containing nanodroplets demonstrated cavitation within the focal area only occurred in locations containing nanodroplets while no cavitation was observed in regions without nanodroplets. Ultrasound imaging (bottom) demonstrated nanodroplet guided cavitation treatment can be monitored in real-time with bubbles appearing as dynamically changing hyperechoic regions.

Bubble Behavior

The bubble expansion and collapse observed in histotripsy is substantially more energetic than traditionally defined inertial cavitation where the maximal bubble diameter becomes equal or greater than twice the initial bubble size [53]. In histotripsy, microbubbles formed from preexisting nuclei <10 nm grow to over 50 μm before violently collapsing, all occurring within 100 μs. This bubble behavior is critical to achieve cell disruption. To study the behavior of cavitation bubbles generated by nanodroplet-mediated histotripsy, optical images of bubbles were recorded by the high-speed camera at different time delays after the arrival of the histotripsy pulse. The peak

negative pressure of 15.6 MPa was used, because it is the lowest pressure at which a cavitation cloud was always generated (P_{cav}=1) using nanodroplets. In agarose gel, the bubble diameter increased to the maximum diameter of 311.2±49.9 µm at 21 µs (**Figure 8**). The average bubble lifespan from the arrival of the histotripsy pulse to when the bubble became too small to be observed on the optical image was measured to be ~60 µs (**Figure 7**). This level of bubble expansion and collapse is similar to the behavior of bubbles formed using histotripsy alone at higher pressures and is anticipated to create cell disruption.
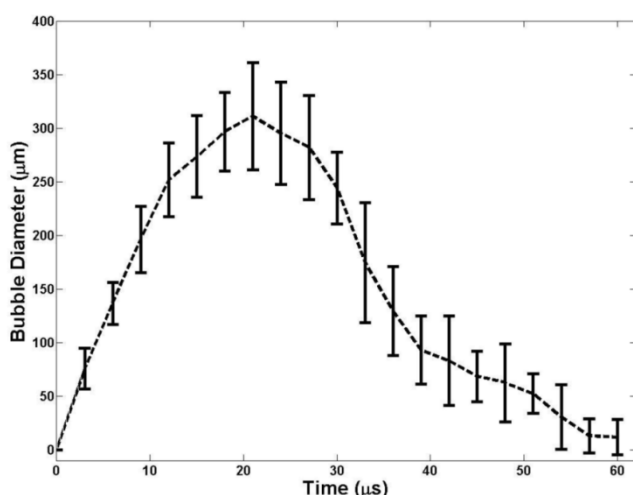

Fig 8. A plot of bubble behavior in agarose tissue phantoms. The diameter of bubble generated using a 2-cycle 500kHz pulse at 15MPa as a function of time. At each time point, the average bubble diameter and standard deviation are plotted.

Ablation of Red Blood Cells in Tissue Phantom

Agarose tissue phantoms embedded with RBC layers were used to evaluate the ability of nanodroplet-mediated histotripsy to create cell fractionation, as lesions visualized in RBC phantoms have been shown to be similar to those generated in tissue identified by histology [44]. Nanodroplet-mediated histotripsy resulted in consistent, well-defined lesions in RBC phantoms, similar to those observed for histotripsy therapy, but at pressure levels well below the histotripsy intrinsic threshold. At peak negative pressure below 10 MPa, no microbubbles were observed and no lesions were visualized. At peak negative pressure of 11.0 MPa and greater, when cavitation bubbles were generated, well-defined lesions were formed in the RBC phantoms using nanodroplets combined with histotripsy (**Figure 9**). Nanodroplet-mediated histotripsy fractionated the RBC phantom with similar efficiency to histotripsy at higher pressure with all RBCs within the focal volume completely fractionated within 2,000 pulses, resulting in transparent lesions with no intact RBCs remaining. The lesion area was analyzed following the procedure described in the Experimental Section demonstrating the area of lesion in the RBC layer increased with increasing pressure. For example, the lesion areas for RBC phantoms containing nanodroplets (n=6) were 0.77±0.09 mm², 3.92±0.41 mm², and 6.27±0.86 mm² for peak negative pressures of 11.0 MPa, 15.9 MPa, and 20.7 MPa, respectively (**Figure 9**). Furthermore, lesion area was plotted as a function of pulse number demonstrating >75% of the focal region was fractionated within the first 1,000 pulses and >95% of the focal region fractioned after 1,500 pulses at all pressure levels treated (**Figure 10**). In comparison, in control gels without nanodroplets, no lesions were formed at any treatments in this pressure range. These results are important to show that nanodroplet-mediated cavitation can indeed create cell disruption with the same effectiveness (i.e., the same number of pulses) as using histotripsy alone but at a significantly lower pressure. This is an important validation of our hypothesis confirming that the cavitating microbubbles generated via nanodroplets are destructive to use for ablation.
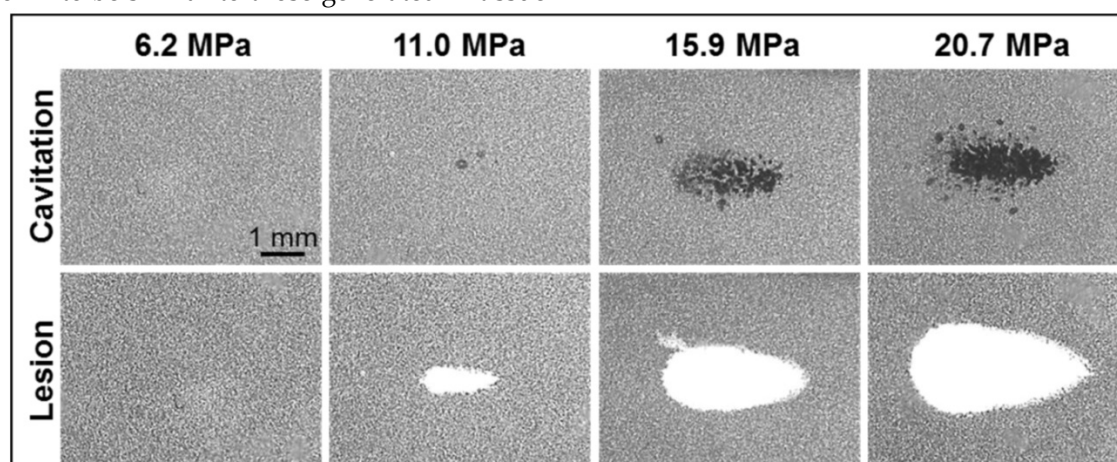

Fig 9. Optical images of nanodroplet-mediated cell fractionation. Images of cavitation bubble cloud (dark) and lesions (white) generated in the RBC agarose gel (grey) using nanodroplet-mediated histotripsy at different pressure levels. A total of 2000 2-cycle pulses at 10 Hz PRF were used for each treatment.
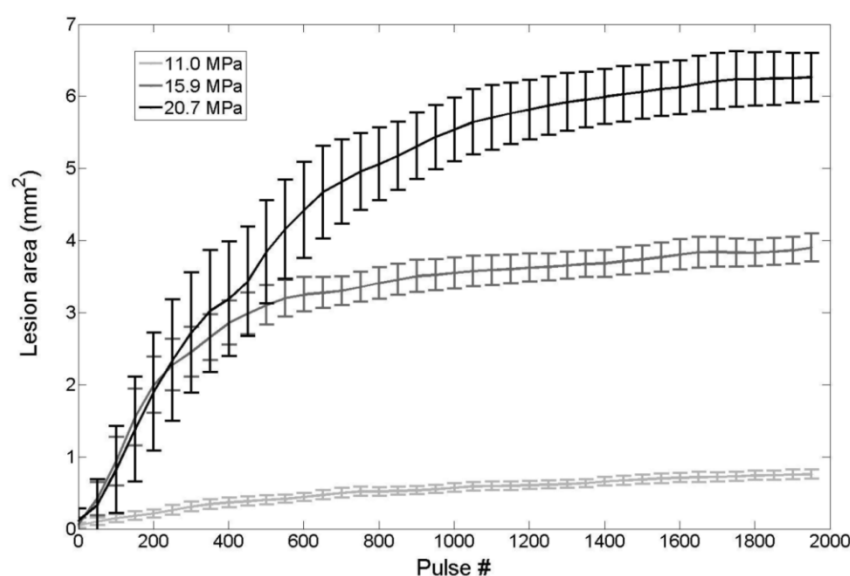
Fig 10. Nanodroplet-mediated lesion formation. The lesion area formed in the RBC agarose gel as a function of pulse number for treatments at 11.0, 15.9, and 20.7 MPa. No damage was formed for treatments at 6.2 MPa.

The findings in this work demonstrated proof of concept for selective cavitational ablation by combining histotripsy with nanodroplets. Our nanodroplets are in the size range required to penetrate through the leaky tumor vasculature and have been shown to decrease the pressure threshold required for histotripsy. These initial experiments demonstrate the potential of selectively applying histotripsy to cancer cells by using an appropriate pressure level. Furthermore, by using a low frequency transducer with a large focal zone, it is possible to apply histotripsy simultaneously to a large focal volume with cavitation occurring only at locations containing nanodroplets. As such, the treatment time for a larger volume of tissue would be shortened while still maintaining high treatment selectivity to cancer cells through the targeted nanodroplets.

Conclusions

In this work, the feasibility of using PFP encapsulated nanodroplets for enhanced histotripsy ablation was investigated. Results support our hypothesis that nanodroplets significantly decrease the histotripsy threshold to form a cavitation bubble cloud while maintaining the effectiveness of histotripsy tissue ablation. Nanodroplet-mediated histotripsy was shown capable of creating microbubble expansion and collapse as well as well-defined ablation similar to histotripsy but at significantly lower pressure. To build upon this initial study, future work will aim to test the hypothesis that our nanodroplets can be functionalized to bind to cancer cells *in vitro* and demonstrate that nanodroplet-mediated histotripsy can selectively fractionate cancer cells. We will also investigate that using nanodroplets delivered to the capsule of tumor nodules, the tumor nodule can be fractionated from outside to the inner core. Furthermore, future experiments will aim to show that nanodroplets can be delivered and accumulated at a tumor site for the selective histotripsy ablation of cancer cells in a relevant *in vivo* cancer model.

Competing Interests

The authors have declared that no competing interest exists.

References

1. Campbell RB. Tumor physiology and delivery of nanopharmaceuticals. Anticancer Agents Med Chem. 2006; 6: 503-12.
2. Hobbs SK, Monsky WL, Yuan F, Roberts WG, Griffith L, Torchilin VP, et al. Regulation of transport pathways in tumor vessels: role of tumor type and microenvironment. Proc Natl Acad Sci U S A. 1998; 95: 4607-12.
3. Torchilin V. Tumor delivery of macromolecular drugs based on the EPR effect. Adv Drug Deliv Rev. 2011; 63: 131-5.
4. Fang J, Nakamura H, Maeda H. The EPR effect: Unique features of tumor blood vessels for drug delivery, factors involved, and limitations and augmentation of the effect. Adv Drug Deliv Rev. 2011; 63: 136-51.
5. Gao Z, Kennedy AM, Christensen DA, Rapoport NY. Drug-loaded nano/microbubbles for combining ultrasonography and targeted chemotherapy. Ultrasonics. 2008; 48: 260-70. Epub 2007 Nov 19.
6. Kawabata Ki, Asami R, Yoshikawa H, Azuma T, Umemura Si. Sustaining Microbubbles Derived from Phase Change Nanodroplet by Low-Amplitude Ultrasound Exposure. Jpn J Appl Phys. 2010; 49: 07HF20.
7. Sheeran PS, Luois S, Dayton PA, Matsunaga TO. Formulation and acoustic studies of a new phase-shift agent for diagnostic and therapeutic ultrasound. Langmuir. 2011; 27: 10412-20.
8. Sheeran PS, Wong VP, Luois S, McFarland RJ, Ross WD, Feingold S, et al. Decafluorobutane as a Phase-Change Contrast Agent for Low-Energy Extravascular Ultrasonic Imaging. Ultrasound Med Biol. 2011; 37: 1518-30.

9.   Du L, Jin Y, Zhou W, Zhao J. Ultrasound-Triggered Drug Release and Enhanced Anticancer Effect of Doxorubicin-Loaded Poly(D,L-Lactide-co-Glycolide)-Methoxy-Poly(Ethylene Glycol) Nanodroplets. Ultrasound Med Biol. 2011; 37: 1252-58.

10. Rapoport N, Nam KH, Gupta R, Gao Z, Mohan P, Payne A, et al. Ultrasound-mediated tumor imaging and nanotherapy using drug loaded, block copolymer stabilized perfluorocarbon nanoemulsions. J Control Release. 2011; 153: 4-15.

11. Rapoport NY, Nam KH, Gao Z, Kennedy A. Application of Ultrasound for Targeted Nanotherapy of Malignant Tumors. Acoust Phys. 2009; 55: 594-601.

12. Gao Z, Kennedy AM, Christensen DA, Rapoport NY. Drug-loaded nano/microbubbles for combining ultrasonography and targeted chemotherapy. Ultrasonics. 2008; 48: 260-70.

13. Kripfgans OD, Fowlkes JB, Miller DL, Eldevik OP, Carson PL. Acoustic droplet vaporization for therapeutic and diagnostic applications. Ultrasound Med Biol. 2000; 26: 1177-89.

14. Sheeran PS, Wong VP, Luois S, McFarland RJ, Ross WD, Feingold S, et al. Decafluorobutane as a phase-change contrast agent for low-energy extravascular ultrasonic imaging. Ultrasound Med Biol. 2011; 37: 1518-30.

15. Kawabata K, Asami R, Axuma T, Umemura S. Acoustic response of microbubbles derived from phase-change nanodroplet. Jpn J Appl Phys. 2010; 49: 07HF18.

16. Sheeran PS, Luois S, Dayton PA, Matsunaga TO. Formulation and acoustic studies of a new phase-shift agent for diagnostic and therapeutic ultrasound. Langmuir. 2011; 27: 10412-20.

17. Wilson K, Homan K, Emelianov S. Biomedical photoacoustics beyond thermal expansion using triggered nanodroplet vaporization for contrast-enhanced imaging. Nat Commun. 2012; 3: 618.

18. Kawabata Ki, Asami R, Azuma T, Yoshikawa H, Umemura Si. Cavitation assisted HIFU with phase-change nano droplet. IEEE International Ultrasonics Symposium. 2008;: 780-3.

19. Kopechek JA, Zhang P, Burgess MT, Porter TM. Synthesis of phase-shift nanoemulsions with narrow size distributions for acoustic droplet vaporization and bubble-enhanced ultrasound-mediated ablation. J Vis Exp. 2012;: e4308.

20. Zhang M, Fabiilli ML, Haworth KJ, Padilla F, Swanson SD, Kripfgans OD, et al. Acoustic droplet vaporization for enhancement of thermal ablation by high intensity focused ultrasound. Acad Radiol. 2011; 18: 1123-32.

21. Kieran K, Hall TL, Parsons JE, Wolf JS, Jr., Fowlkes JB, Cain CA, et al. Refining histotripsy: defining the parameter space for the creation of nonthermal lesions with high intensity, pulsed focused ultrasound of the in vitro kidney. J Urol. 2007; 178: 672-6.

22. Winterroth F, Xu Z, Wang TY, Wilkinson JE, Fowlkes JB, Roberts WW, et al. Examining and analyzing subcellular morphology of renal tissue treated by histotripsy. Ultrasound Med Biol. 2011; 37: 78-86.

23. Xu Z, Fan Z, Hall TL, Winterroth F, Fowlkes JB, Cain CA. Size measurement of tissue debris particles generated from pulsed ultrasound cavitational therapy-histotripsy. Ultrasound Med Biol. 2009; 35: 245-55.

24. Xu Z, Fowlkes JB, Cain CA. A new strategy to enhance cavitational tissue erosion using a high-intensity, Initiating sequence. IEEE Trans Ultrason Ferroelectr Freq Control. 2006; 53: 1412-24.

25. Xu Z, Fowlkes JB, Rothman ED, Levin AM, Cain CA. Controlled ultrasound tissue erosion: the role of dynamic interaction between insonation and microbubble activity. J Acoust Soc Am. 2005; 117: 424-35.

26. Xu Z, Ludomirsky A, Eun LY, Hall TL, Tran BC, Fowlkes JB, et al. Controlled ultrasound tissue erosion. IEEE Trans Ultrason Ferroelectr Freq Control. 2004; 51: 726-36.

27. Maxwell AD, Owens G, Gurm HS, Ives K, Myers DD, Jr., Xu Z. Noninvasive treatment of deep venous thrombosis using pulsed ultrasound cavitation therapy (histotripsy) in a porcine model. J Vasc Interv Radiol. 2011; 22: 369-77.

28. Xu Z, Owens G, Gordon D, Cain C, Ludomirsky A. Noninvasive creation of an atrial septal defect by histotripsy in a canine model. Circulation. 2010; 121: 742-9.

29. Durmaz H, Dag A, Altintas O, Erdogan T, Hizal G, Tunca U. One-pot synthesis of ABC type triblock copolymers via in situ click 3+2 and Diels-Alder 4+2 reactions. Macromolecules 2007; 40: 191-98.

30. Durmaz YY, Vlaisavljevich E, Xu Z, Elsayed MEH. Development of targeted nano-bubbles for ultrasound imaging and ablation of prostate cancer. 35th Annual Symposium of Macromolecular Science & Engineering. Ann Arbor, Michigan. 2011.

31. Durmaz YY, Vlaisavljevich E, Xu Z, ElSayed MEH. Development of nanodroplets for targeted ultrasound-mediated ablation of cancer. Engineering Graduate Symposium. Ann Arbor, Michigan. 2011.

32. Bartczak D, Kanaras AG. Preparation of peptide-functionalized gold nanoparticles using one pot EDC/sulfo-NHS coupling. Langmuir. 2011; 27: 10119-23.

33. Nam K, Kimura T, Kishida A. Controlling coupling reaction of EDC and NHS for preparation of collagen gels using ethanol/water co-solvents. Macromol Biosci. 2008; 8: 32-7.

34. Wildling L, Unterauer B, Zhu R, Rupprecht A, Haselgrubler T, Rankl C, et al. Linking of sensor molecules with amino groups to amino-functionalized AFM tips. Bioconjug Chem. 2011; 22: 1239-48.

35. Yang X, Church CC. A model for the dynamics of gas bubbles in soft tissue. J Acoust Soc Am. 2005; 118: 3595-606.

36. Maxwell AD, Cain CA, Hall TL, Fowlkes JB, Xu Z. Probability of cavitation for single ultrasound pulses applied to tissues and tissue-mimicking materials. Ultrasound Med Biol. 2013; 39: 449-65.

37. Sheeran PS, Dayton PA. Phase-change contrast agents for imaging and therapy. Curr Pharm Des. 2012; 18: 2152-65.

38. Masuzaki R, Tateishi R, Yoshida H, Sato T, Ohki T, Goto T, et al. Assessing liver tumor stiffness by transient elastography. Hepatol Int. 2007; 1: 394-7.

39. Zhang M, Nigwekar P, Castaneda B, Hoyt K, Joseph JV, di Sant'Agnese A, et al. Quantitative characterization of viscoelastic properties of human prostate correlated with histology. Ultrasound Med Biol. 2008; 34: 1033-42.

40. Friedman M, Strauss M, Amendt P, London R, Glinsky M. Two-dimensional Rayleigh model for bubble evolution in soft tissue. Phys Fluids. 2002; 14: 1768-80.

41. Ayme EJ, Carstensen EL. Cavitation induced by asymmetric distorted pulses of ultrasound: theoretical predictions. IEEE Trans Ultrason Ferroelectr Freq Control. 1989; 36: 32-40.

42. Parsons JE, Cain CA, Fowlkes JB. Cost-effective assembly of a basic fiber-optic hydrophone for measurement of high-amplitude therapeutic ultrasound fields. J Acoust Soc Am. 2006; 119: 1432-40.

43. Normand V, Lootens DL, Amici E, Plucknett KP, Aymard P. New insight into agarose gel mechanical properties. Biomacromolecules. 2000; 1: 730-8.

44. Maxwell AD, Wang TY, Yuan L, Duryea AP, Xu Z, Cain CA. A tissue phantom for visualization and measurement of ultrasound-induced cavitation damage. Ultrasound Med Biol. 2010; 36: 2132-43.

45. O'Reilly RK. Spherical polymer micelles: nanosized reaction vessels? Phil. Trans. R. Soc. A. 2007; 365: 2863-78.

46. Zhulina EB, Adam M, LaRue I, Sheiko SS, Rubinstein M. Diblock Copolymer Micelles in a Dilute Solution. Macromolecules. 2005; 38: 5330-51.

47. Matyjaszewski K, Xia J. Atom Transfer Radical Polymerization. Chem Rev. 2001; 101: 2921-90.

48. Gao Z, Kennedy AM, Christensen DA, Rapoport NY. Drug-loaded nano/microbubbles for combining ultrasonography and targeted chemotherapy. Ultrasonics. 2008; 48: 260-70.

49. Shiraishi K, Endoh R, Furuhata H, Nishihara M, Suzuki R, Maruyama K, et al. A facile preparation method of a PFC-containing nano-sized emulsion for theranostics of solid tumors. Int J Pharm. 2011; 421: 379-87.

50. Wang C-H, Kang S-T, Lee Y-H, Luo Y-L, Huang Y-F, Yeh C-K. Aptamer-conjugated and drug-loaded acoustic droplets for ultrasound theranosis. Biomaterials. 2012; 33: 1939-47.

51. Apfel RE, Holland CK. Gauging the likelihood of cavitation from short-pulse, low-duty cycle diagnostic ultrasound. Ultrasound Med Biol. 1991; 17: 179-85.

52. Carstensen EL, Gracewski S, Dalecki D. The search for cavitation in vivo. Ultrasound Med Biol. 2000; 26: 1377-85.

53. Leighton TG. The Acoustic Bubble. Academic Press. 1994.

# Development of Nanodroplets for Histotripsy-Mediated Cell Ablation

Yasemin Yuksel Durmaz, Eli Vlaisavljevich, Zhen Xu*, and Mohamed ElSayed*

Abstract: We report the synthesis of two amphiphilic PEG-*b*-(PAA)-*b*-P(HDFMA-*co*-MMA) polymers that proved to encapsulate 1%-2% v/v PFP forming nanodroplets. Combining these nanodroplets with histotripsy proved to generate a cavitation bubble cloud that ablates neighboring RBCs at a 2.5-fold lower acoustic pressure pressure compared to histotripsy alone. Further, these nanodroplets maintained their average size and concentration upon incubation with BSA for 24 hours at 37ºC, which prove their promise for cancer cell ablation and warrant their future testing *in vivo*.

Interest in ultrasound (US) imaging and delivery of therapeutic agents to the extravascular space particularly into solid tumors has motivated the development of nano-sized contrast agents.[1] Lipids,[2] fluoroalkyl surfactant,[3] and amphiphilic block copolymers[4] have been used to encapsulate perfluorocarbon (PFC) forming nanodroplets. The potential of nanodroplets for US contrast imaging,[5] local delivery of chemotherapeutic agents,[5a, 6] and non-targeted/targeted high intensity focus ultrasound (HIFU)[7] has been extensively investigated. For example, Dayton et al. used oil to solubilize paclitaxel and incorporate it with the PFC core to develop therapeutic and imaging nanodroplets.[8] Recently, lipid-coated nanodroplets encapsulating perfluoropentane (PFP) were developed for cell-specific imaging and therapy.[7a] Further, attachment of targeting ligands to nanodroplets increased their accumulation in tumor tissue, which enhanced contrast resolution in US imaging.[9] Despite their promise in US imaging and drug delivery, nanodroplets have not been used for ultrasound-mediated cell ablation. Therefore, it would be of great interest to develop well-defined nanodroplets that can withstand the shear forces in the blood circulation, resist the adsorption of serum proteins that will trigger their phagocytosis by macrophages (e.g. Kupffer cells), and allow the covalent attachment of targeting ligands to be used for mechanical ablation of cancer cells. To address this need, we designed and synthesized the amphiphilic poly[(ethylene glycol-*b*-(acrylic acid)-*b*-(heptadecafluorodecyl methacrylate-*co*-methyl methacrylate)] [PEG-*b*-(PAA)-*b*-P(HDFMA-*co*-MMA)] triblock copolymer, which encapsulates perfluoropentane (PFP, an US

contrast agent) in the core forming nanodroplets with an average diameter of 100-350nm **(Table 1 & Figure 1)**. The hydrophilic PEG block is used to inhibit the adsorption of serum proteins and inhibit the uptake by Kupffer cells,[10] which will consequently increase droplets residence time in the systemic circulation. Further, the free end of the PEG block can be used to conjugate different types of targeting ligands prior to the formulation of the nanodroplets, which will allow the presentation of a well-defined and tunable number of targeting ligands on the droplets' surface to mediate selective binding to cancer cells.[10] The carboxylic acid groups in the central PAA block are used for covalent cross-linkage of the polymer chains to form a flexible shell that stabilizes the nanodroplets. The fluorinated and hydrophobic P(HDFMA-*co*-MMA) block is designed to facilitate the encapsulation of PFP in the droplets' core.[3, 11]
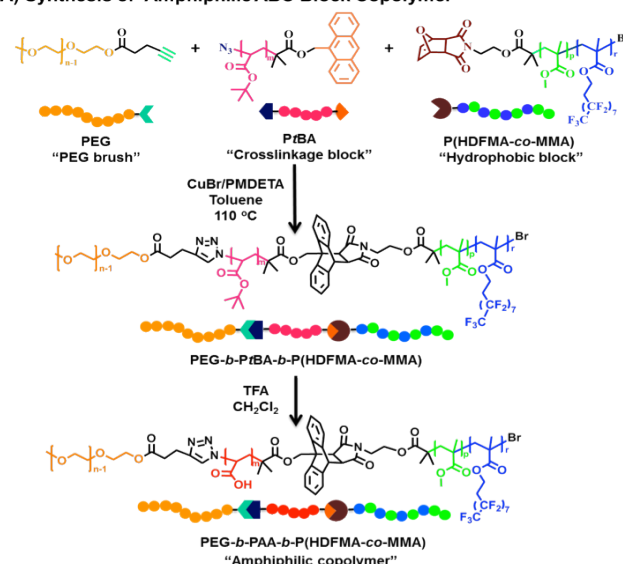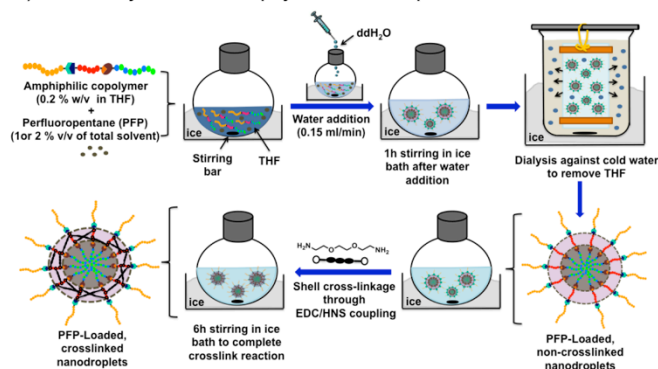

Figure 1. (A) Scheme for synthesis of amphiphilic PEG-*b*-(PAA)-*b*-P(HDFMA-*co*-MMA) copolymers using one-pot "click" reaction. (B) Schematic presentation showing the formulation of PFP-loaded nanodroplets using amphiphilic PEG-*b*-(PAA)-*b*-P(HDFMA-*co*-MMA) copolymers.

[∗] Dr. Yasemin Yuksel Durmaz and Asist. Prof. Mohamed Elsayed∗
     Department of Biomedical Engineering, University of Michigan
     1101 Beal Avenue, Lurie Biomedical Engineering Bldg
     Ann Arbor, MI, 48109, USA
     Fax: (+) 734 647 4834
     E-mail: melsayed@umich.edu
     Homepage: www.bme.umich.edu/centlab.php

     Mr. Eli Vlaisavljevich, Asist. Prof. Zhen Xu∗
     Department of Biomedical Engineering, University of Michigan
     2115 Carl A. Gerstacker Building, 2200 Bonisteel Boulevard
     Ann Arbor, MI, 48109, USA
     Fax: + 1 (734) 939-1905
     E-mail: zhenx@umich.edu
     Homepage: www.bme.umich.edu/labs/xulab/

     Supporting information for this article is available on the WWW under http://dx.doi.org/10.1002/anie.201xxxxxx.

Table 1. Composition of amphiphilic PEG-*b*-PAA-*b*-P(HDFMA-*co*-MMA) copolymers.

Polymer	$M_{n,PEG}$ (g/mol) (# of units)	$M_{n,PtBA}$[a,b] (g/mol) (# of units)	$M_{n,P(MMA-co-HDFMA)}$[a] (g/mol) (# of units)	M_{nHP}/M_{nHF}[c]	# of HP/# of HF units[d]	$M_{n,ABC}$[a] (g/mol)	$M_{n,ABC}$[e] (g/mol)	PD[e]
ABC-1	2000 (45)	1640 (10)	6720 (29)	1.84	0.53	10370	9613	1.11
ABC-2	5000 (113)	1640 (10)	11390 (52.5)	1.71	0.42	18040	17510	1.12

[a] Calculated from ¹H NMR spectra. [b] *Tert*-butyl groups were efficiently hydrolyzed into carboxylic acid group to obtain the final ABC copolymer. [c] M_{nHP}/M_{nHF}: Molecular weight of hydrophobic block (HP)/molecular weight of hydrophilic blocks (HF). [d] # of HP/# of HF units: The number of hydrophobic units (HP)/the number of hydrophilic units. [e] Determined by gel permeation chromatography (GPC) using Styragel HR 4E column compared to a series of PMMA standards (PolyAnalitik Inc, Canada) using THF as a mobile phase at a flow rate of 1 mL/min at 35 °C. Data were analyzed using Viscotek OmniSEC Omni-01 software.

Histotripsy is a non-invasive, non-thermal, image-guided, ultrasound ablation method that uses extremely high acoustic pressure and microseconds long pulses to generate a cluster of microbubbles (bubble cloud) from pre-existing gas pockets in tissue.[12] Rapid expansion and energetic collapse (i.e. cavitation) of the formed microbubbles, each with an average diameter >50μm, mechanically fragment the adjacent cells into subcellular debris.[13] Histotripsy has been used to ablate tumor cells in canine prostate cancer model[14] and dissolve deep vein thrombosis in a porcine model.[15] However, the required high acoustic pressure and the inability to detect/image small metastatic tumor foci are some of histotripsy limitations, which can be overcome by combing histotripsy with our nanodroplets.

We hypothesize that PFP-loaded nanodroplets with an average diameter < 500nm can diffuse across tumor's leaky vasculature and accumulate in the cancer lesion when administered into the systemic circulation.[16] Applying specific US pulse sequences to the tumor lesion will deliver the acoustic energy necessary to convert the PFP core from the liquid to the gaseous phase in a process known as acoustic droplet vaporization (ADV),[16a, 17] which will allow real time US imaging of tumor tissue. Unlike histotripsy that relies on cavitation nuclei derived from rare gas pockets in the tissue and extremely high acoustic pressures to initiate the cavitation process, the gas bubbles formed by ADV can act as cavitation nuclei to generate and maintain the cavitation bubble cloud at a significantly reduced pressure. The significantly reduced cavitation threshold will allow us to deliver histotripsy to the tumor tissue "tagged" with the nanodroplets resulting in selective fractionation of cancer cells while sparing the surrounding normal tissue.

In this report, we describe the synthesis of two triblock copolymers (ABC-1 and ABC-2) where the molecular weight of the P(HDFMA-*co*-MMA) (6.5kDa and 11.5kDa) and PEG (2kDa and 5kDa) blocks was varied to examine their effect on encapsulation efficiency of different amounts of PFP (1% and 2% v/v) and overall droplets stability. We describe the self-assembly of amphiphilic ABC-1 and ABC-2 polymers around the PFP core forming nanodroplets with variable PFP content (0%, 1%, and 2% v/v), the chemical cross-linkage of the polymer shell to stabilize the droplets, and their characterization in terms of size, shape, and intrinsic cytotoxicity towards mammalian cells. We investigated the relationship between polymer composition (ABC-1 versus ABC-2) and PFP content (0%, 1%, and 2% v/v) on the ability of the formulated nanodroplets to initiate a bubble cloud in agarose gel phantoms with similar mechanical and acoustic properties to tumor tissue in response to a 2 cycles long histotripsy pulse. Further, we correlated the behavior of the bubble cloud to the observed damage of a layer of red blood cells (RBCs) embedded with different nanodroplets in the agarose gel phantom to identify the ablative capacity of each formulation. In addition, we showed effective hemolysis of RBCs using the combination of most effective composition and histotripsy under the physiological conditions. Futher, we examined the change in nanodroplets size and concentration upon incubation with bovine serum albumin (BSA) as a model serum protein for 24 hours at 37°C while stirring to determine the stability of different nanodroplets formulations in a condition that resembles the systemic circulation *in vivo*. Results establish the potential of combining these nanodroplets with histotripsy to achieve ultrasound-mediated cell ablation.

Two PEG-*b*-(PAA)-*b*-P(HDFMA-*co*-MMA) polymers were synthesized via a one-pot "click" reaction of PEG, poly(*tert*-butyl acrylate) (P*t*BA), and P(HDFMA-*co*-MMA) blocks following the synthesis scheme outlined in **Figure 1, Panel A**. Detailed description of the synthesis procedure and supporting spectra are available in the Supplementary Information (**Scheme S1**). Briefly, commercial PEG (2kDa and 5kDa) was reacted with 4-pentynoic acid to introduce a terminal alkyne group forming PEG-Alkyne (block A). The P*t*BA block was synthesized via atom transfer radical polymerization (ATRP) using anthracene-functional initiator followed by azidation of the terminal Br group to yield the Anth-P*t*BA-N₃ block (block B) (**Supplementary Information, Scheme S1**). Earlier reports show that the percentage of fluorinated monomers play a critical role in the amount of encapsulated PFC and the stability of the formed droplets.[3] Therefore, we synthesized two different P(HDFMA-*co*-MMA) copolymers (block C) that incorporate a different number of fluorinated HDFMA units (8 and 13.5 units) and different molecular weights (6.7kDa and 11.4kDa) (**Supplementary Information, Table S1**) via ATRP using a maleimide-functional initiator (**Supplementary Information, Scheme S1**). Pure A, B, and C blocks were coupled via a one-pot alkyne-azide and Diels-Alder "click" reactions in presence of a copper catalyst (**Figure 1, Panel A**) to yield two ABC triblock copolymers (ABC-1 and ABC-2) that vary in the length of the PEG and P(HDFMA-*co*-MMA) blocks but have similar number of P*t*BA units (**Table 1**). The synthesized polymers (ABC-1 and ABC-2) were purified and characterized (**Supplementary Information, Figures S8-S11**) before acid hydrolysis of the *tert*-butyl groups to obtain the corresponding acrylic acid.

ABC-1 and ABC-2 copolymers were dissolved in tetrahydrofuran (THF) followed by cooling down the polymer solution in an ice bath and adding different volumes of PFP (0%, 1%, or 2% v/v) while mixing. An equal amount of water was slowly added to the polymer/PFP mixture to initiate polymers self-assembly into nano-sized micelles that will encapsulate the hydrophobic PFP solution forming nanodroplets (**Figure 1, Panel B**). This solution mixture was kept stirring on an ice bath for 1 hour before transferring to a dialysis bag and dialyzing against ice cold water for 12 hours to yield a homogenous milky solution indicating nanodroplets formation. We used 2,2`-(ethylenedioxy)-bis(ethylamine) linker to crosslink the polymer chains via standard NHS/EDC coupling reactions with the central PAA block.[18] Cross-linked nanodroplets were further purified by dialysis against ice cold water before their characterization and use in ablation studies.

We confirmed the cross-linkage of the central PAA block by examining the thermal behavior of the amphiphilic polymer (e.g. ABC-1), the hydrophobic P(HDFMA-*co*-MMA) block, cross-linked droplets, and non-cross-linked droplets when heated between 20-120°C using a differential scanning calorimeter. The P(HDFMA-*co*-MMA) block with an average molecular weight of 6.7 kDa has a glass transition temperature (T_g) of 61.4°C, which increased to 76.5°C with the increase in molecular weight to 11.4 KDa (**Supplementary Information, Figure S12 & Table S2**). Since the PEG and P(HDFMA-*co*-MMA) blocks are not miscible, the thermograph of ABC-1 polymer shows two transitions at 50.8°C and 60.9°C corresponding to the PEG melting point and T_g of the P(HDFMA-*co*-MMA) block, respectively (**Supplementary Information, Figure S12**). Increasing the molecular weight of the

PEG and P(HDFMA-*co*-MMA) blocks increased their melting point and T_g, respectively **(Supplementary Information, Table S2)**. The restricted mobility of the polymer chains in cross-linked droplets prepared using ABC-1 polymer caused an increase in the T_g compared to the parent polymer and non-cross-linked droplets **(Supplementary Information, Figure S12 & Table S2)**. However, the insignificant difference in the T_g between cross-linked and non-cross-linked droplets prepared using ABC-2 is due to the increase in PEG content (38%) compared to ABC-1 (24%), which acts as a plasticizer and reduce the observed T_g as shown in previous reports.[19]
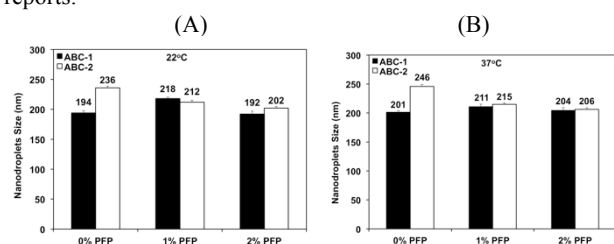

Figure 2. Size of cross-linked nanodroplets prepared using ABC-1 and ABC-2 polymers with different PFP content (0%, 1%, and 2% v/v) at: (A) 22ºC and (B) 37ºC calculated using the Nanoparticle Tracking Analysis (NTA) 2.3 software. Results are reported as the average of six different measurements collected from three independent solutions + standard error of the mean.

We used Nanosight NS500 (NanoSight Limited, Amesbury, United Kingdom) equipped with a sample chamber with a 640nm laser and a fluoroelastomer O-ring to measure the size and concentration (i.e. number of nanodroplets/mL) of cross-linked (CL) nanodroplets formulated using ABC-1 and ABC-2 polymers as a function of PFP loading (0%, 1%, and 2% v/v) at room (22ºC) and body (37ºC) temperatures. We relied on the Nanoparticle Tracking Analysis (NTA) 2.3 software to capture and analyze images of different nanodroplets solutions and calculate the average size of each formulation **(Figure 2)**. Results show that nanodroplets formulated using ABC-1 polymer have average diameter of 192±4.7-218±2.1nm at 22ºC, which slightly increased to 201±2.61-211±4.7nm at 37ºC **(Figure 2)**. Nanodroplets formulated using ABC-2 polymer have average diameter of 202±2.7-236±2.6nm at 22ºC, which also slightly increased to 206±2.9-246±3.4nm at 37ºC. Results show that the increase in PFP loading from 0%-2% v/v did not influence the average size of all the formulated nanodroplets. It is important to note that NTA software identified the major fraction in each formulation and calculated its average mode size and concentration **(Table 2)**. Results show that the average mode size for ND-ABC-1-1% and ND-ABC-1-2% droplets at 37ºC is 111.9±6.8nm and 135.3±7.1nm, respectively. Similarly, the average mode size for ND-ABC-2-1% and ND-ABC-2-2% droplets at 37ºC is 167.0±9.0nm and 166.8±4.3nm, respectively **(Table 2 & Supplementary Information, Figure S13)**. These results clearly show that the average size of cross-linked (CL) nanodroplets prepared using ABC-1 and ABC-2 polymers with different PFP content is much smaller than the size cutoff (~500nm) of the tumor vasculature.[4, 20] Furthermore, the concentration of cross-linked ND-ABC-1 and ND-ABC-2 nanodroplets did not decrease upon increasing the solution temperature from 22ºC to 37ºC, which

indicates droplets resistance to dissolution and stability at body temperature **(Table 2)**. These results collectively indicate the promise of these nanodroplets in future *in vivo* evaluation.
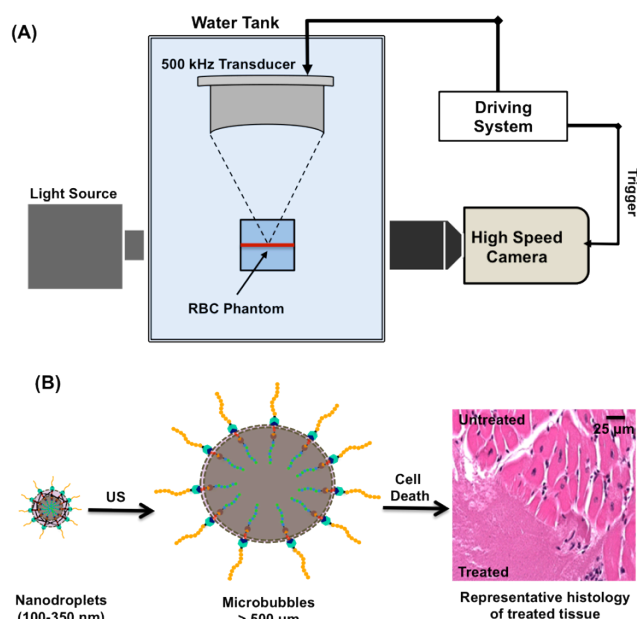

Figure 3. (A) A schematic drawing of the experimental setup incorporating a 500 kHz transducer attached to a motorized 3D positioning system controlled using a PC console. The transducer focus was aligned with the center of the red blood cell (RBC) layer embedded in the agarose gel. Formation of a bubble cloud in response to histotripsy treatment was monitored using high-speed optical imaging (Phantom V210, Vision Research). (B) A schematic drawing showing the expansion of the nanodroplets (100-350nm) forming microbubbles (> 500µm) before energetically collapsing and mechanically fractionating neighboring cells.

We visualized different nanodroplets formulations using a FEI Quanta 3D Dual-Beam Environmental Scanning Electron Microscope (FEI Co., Oregon, USA) under low pressure (5.2 Torr) and temperature (1.3ºC) to examine droplets morphology. Images of all PFP-loaded formulations show spherical nanodroplets **(Supplementary Information, Figure S14)** with average size of 316±49nm, 342±11nm, 310±10nm, and 333±9nm for ND-ABC-1-1% PFP, ND-ABC-1-2% PFP, ND-ABC-2-1% PFP, and ND-ABC-2-2% PFP, respectively. The higher average size observed with scanning electron microscopy could possibly be as a result of the small number of droplets manually analyzed compared to NTA, which measures the size of each droplet in the solution or/and low pressure which may cause expension of PFP. We used Malvern ZetasizerNano ZSP (Malvern, United Kingdom) to measure the zeta potential of nanodroplets formulations, which was in the range of -40.1±7.16 and -24.5±6.71 mV showing similar surface charge with most of the PEG containig micelles[21] and liposome surfaces[22] **(Table 2)**.

Agarose tissue phantoms (1% w/v) with an embedded layer of red blood cells (RBCs) have been used as model tissue phantoms to investigate the ablative effects of histotripsy therapy.[23] To compare the effects of our nanodroplet-mediated ablation to histotripsy alone at higher pressure, we treated RBC agarose tissue phantoms (1% w/v) containing each of our nanodroplet formulations **(Figure 3)**. Briefly, the agarose phantom was placed in the focal zone of a 32 element, 500 kHz, transducer inside a degassed water tank at 37ºC **(Figure 3, Panel A)**. A high-speed, 1 megapixel CCD camera (Phantom V210, Vision Research) was positioned to image the plane of the RBCs layer throughout

Table 2. Properties of the nanodroplets prepared using ABC-1 and ABC-2 polymers.

Nanodroplets Code	Mode Size at 22°C (nm)[a]	Concentration at 22ºC (10^10 Particles/mL)[a]	Mode Size at 37ºC (nm)[a]	Concentration at 37ºC (10^10 Particles/mL)[a]	Zeta Potential (mV)[b]
ND-ABC-1-0% PFP	164.5±8.5	2.31±0.08	162.0±6.5	2.96±0.07	-40.1±7.16
ND-ABC-1-1% PFP	117.5±9.7	2.50±0.05	111.9±6.8	2.58±0.04	-39.9±7.55
ND-ABC-1-2% PFP	126.3±8.0	3.07±0.11	135.3±7.1	3.00±0.12	-37.0±24.8
ND-ABC-2-0% PFP	178.9±7.4	2.98±0.10	187.3±10.8	2.98±0.09	-24.5±6.71
ND-ABC-2-1% PFP	163.0±11.1	3.59±0.09	167.0±9.0	4.09±0.11	-26.7±7.32
ND-ABC-2-2% PFP	159.1±6.2	4.41±0.11	166.8±4.3	4.85±0.12	-38.8±13.6

[a] Mode size represents the most abundant fraction in the nanodroplets solution identified and calculated using Nanoparticles Tracking Analysis (NTA) and NTA 2.3 build 127 software. Results are the average of 6 measurements of a minimum of 3 independent experiments ± standard error of the mean (SEM). The average size of the nanodroplets is presented in Figure 2.
[b] Measured using Malvern ZetasizerNano ZSP at room temperature.

the histotripsy treatment using a flash lamp as a backlight for the phantom to record the bubble cloud formed from the expansion of the embedded nanodroplets into microbubbles as well as the resulting damage to the RBC tissue phantom. We hypothesized that ultrasound treatment of the embedded nanodroplets will trigger acoustic droplet vaporization forming microbubbles, which will expand reaching an average size > 50μm before they violently collapse causing disruption of the neighboring RBCs (Figure 3, Panel B). Disruption of the translucent RBCs layer renders the agarose gel more transparent, which provides visual evidence of cell ablation. Previous work has demonstrated that damage to the RBC tissue phantoms directly correlates to the tissue damage formed by histotripsy therapy.[23] We tested our hypothesis by applying histotripsy pulses to the center of the agarose gels at the RBC layer using a pulse repetition frequency of 10Hz at a peak negative pressure of 20.7MPa. We embedded an equal number of nanodroplets (2.36×10^8 droplets/mL) in the agarose gel to eliminate the effect of droplets concentration on the observed ablation behavior but rather focus on investigating the effect of polymer composition (ABC-1 versus ABC-2) and PFP content (0%, 1%, and 2% v/v) on ablation capacity to identify the most effective formulation. Results show that histotripsy application could not initiate a bubble cloud from empty nanodroplets (i.e. 0% PFP loading) prepared using ABC-1 and ABC-2 polymers at the applied acoustic pressure (20.7MPa) and no damage was observed in the RBCs layer (Figure 4, Panel A). A similar histotripsy application to tissue phantoms containing nanodroplets prepared using ABC-1 polymer loaded with 1% and 2% v/v PFP resulted in the formation of a bubble cloud in the center of the gel and formation of a corresponding transparent zone confirming the ablation of the RBCs (Figure 4, Panel A). The nanodroplets prepared using ABC-2 polymer and loaded with 1% and 2% v/v PFP also resulted in cavitation and lesion formation in response to the histotripsy treatment (Figure 4, Panel A).

PFP content (Figure 4, Panel B). Results show that empty nanodroplets (i.e. 0% PFP loading) caused no ablation to RBCs regardless of the polymer composition used to formulate the nanodroplets. This demonstrates that the loading of PFP in the droplets' core is critical for bubble formation in response to histotripsy treatment. Increasing PFP content from 1% to 2% v/v caused an increase in the surface area of the ablation lesion from $0.67\pm0.23mm^2$ to $5.60\pm0.52mm^2$ (8.4 folds) for nanodroplets prepared using ABC-1 polymer. Similarly, increasing PFP content in the nanodroplets prepared using ABC-2 polymer from 1% to 2% v/v increased the surface area of the ablation lesion from $0.37\pm0.17mm^2$ to $1.59\pm1.86mm^2$ (4.3 folds). It is interesting to note that nanodroplets prepared using ABC-1 polymer exhibit higher ablation capacity compared to those prepared using ABC-2 polymer, which can be attributed to difference in polymer's capacity to encapsulate and retain the loaded PFP. Specifically, ABC-2 polymer has an average of 13.5 units of the fluorinated monomer with the heptadecafluorodecyl groups distributed along a long hydrophobic backbone, which results in strong interaction of the hydrophobic block in the droplets core that limits PFP loading and encapsulation.

Our results are supported by previously published reports showing that the number of fluorinated monomers plays a critical role in PFC loading and encapsulation by a polymeric shell.[3, 11] For example, Yokoyama and coworkers synthesized a series of amphiphilic PEG-b-poly(fluoroheptyl aspartate) copolymers with a variable number of fluorinated alkyl chains and investigated their ability to encapsulate PFC forming nanodroplets.[3, 11] Results showed that introducing 10% of fluoroheptyl units in the polymer backbone was sufficient to encapsulate the loaded PFP (45.5 mg/mL) forming nanodroplets. Incorporation of higher or lower percentages of fluoroheptyl units in the polymer backbone reduced PFP encapsulation by the polymer and negatively affected droplets stability. Further, the increase in the number of fluorinated carbon atoms in the fluoroalkyl chain above 9 decreased the encapsulation of PFP. These results collectively show that the nanodroplets formulated using ABC-1 polymer and loaded by 2% PFP exhibit the highest ablation capacity among all formulations.

We also examined the effect of PFP-loaded nanodroplets coupled with ultrasound on hemolysis of RBCs solution. Specifically the hemolysis ability of nanodroplets (ND-ABC-1-2% PFP) at the same concentration used for phantom experiment was evaluated as combined with histotripsy pulse at a pulse repetition frequency of 50Hz and a peak negative pressure of 20.7MPa (Figure 4, Panel C). The results showed that, PFP-loaded nanodroplets combined with ultrasound hemolyzed 60.9% of RBCs in the solution while empty micelles combined with ultrasound and ultrasound alone caused < 1% hemolysis of the RBCs.
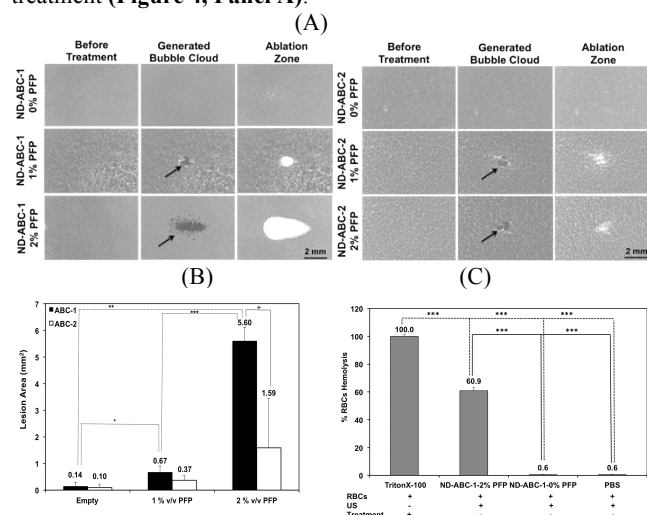

Figure 4. (A) Effect of 2-cycle histotripsy pulse (20.7MPa) with a pulse repetition frequency of 10MHz on the nanodroplets prepared using ABC-1 and ABC-2 polymers with different PFP loading and embedded with RBCs in agarose gels. Images were captured using high-speed, 1 megapixel CCD camera (Phantom V210, Vision Research) capable of a maximum frame rate of 2000 fps and show the generated bubble cloud and the corresponding transparent ablation zone. (B) The area of the ablation zone (mm²) observed after treatment of agarose gels using different nanodroplet formulations calculated using MATLAB (The Math-Works, Natick, MA, USA). (C) RBCs hemolysis using ND-ABC-1-2% PFP and histotripsy pulse (20.7MPa) with a pulse repetition frequency of 50MHz for 10 min. Statistical difference between the area of the ablation zone for different nanodroplets was evaluated using student's t test where * denotes $p \leq 0.05$, ** denotes $p \leq 0.01$, and *** denotes $p \leq 0.001$.

We measured the surface area of the lesions formed in each tissue phantom and plotted it against nanodroplets composition and
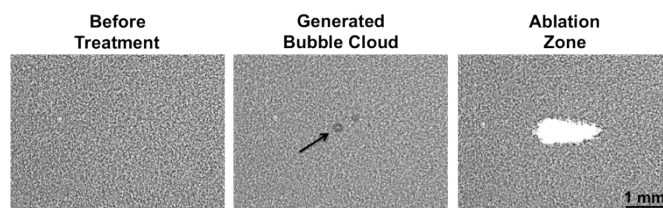

Figure 5. Effect of 2-cycle histotripsy pulse (11.0MPa) with a pulse repetition frequency of 10MHz on ND-ABC-1-2% PFP embedded with RBCs in agarose gels. Images were captured using high-speed camera (Phantom V210, Vision Research) and show the generated bubble cloud and the corresponding transparent ablation zone.

Using ND-ABC-1-2% PFP nanodroplets, we investigated the ability to generate a bubble cloud and ablate the RBCs in agarose gels at a lower acoustic pressure. We applied histotripsy pulses at a pulse repetition frequency of 10Hz and a peak negative pressure of 11.0MPa, which is 2.5-fold lower than the intrinsic threshold of ~26-30 MPa required to generate cavitation using 2-cycle histotripsy pulses alone.[24] Results show the generation of a bubble cloud and a clear ablation zone with sharp margins of the RBCs at this reduced acoustic pressure (Figure 5). This clearly shows that PFP-loaded

Table 3. Effect of incubating nanodroplets at 37ºC for 24 hours in presence and absence of bovine serum albumin on droplets size and concentration.

Nanodroplets Code	Mode Size (nm)[a,b]	Mean Size (nm)[a]	Concentration (10^10 Particles/mL)[a,c]
ND-ABC-1-2% PFP (0h)	131.3±10.9	237.35±6.1	1.98±0.09
ND-ABC-1-2% PFP (24h)	142.0±10.5	243.9±6.0	1.81±0.06
ND-ABC-1-2% PFP+BSA (24h)	144.5±13.9	242.6±4.1	1.93±0.07
ND-ABC-2-2% PFP (0h)	160.0±4.4	207.6±3.2	3.87±0.17
ND-ABC-2-2% PFP (24h)	152.6±4.3	207.0± 3.3	3.45±0.16
ND-ABC-2-2% PFP+BSA (24h)	159.0±7.8	209.6±2.5	2.94± 0.12

[a] Results are the average of 6 measurements of a minimum of 3 independent experiments ± standard error of the mean (SEM). [b] Mode size represents the most abundant fraction in the nanodroplets solution. [c] Nanoparticles concentration is calculated using Nanoparticles Tracking Analysis (NTA) and NTA 2.3 build 127 software.

nanodroplets can reduce the histotripsy cavitation threshold and be used to generate lesions at significantly lower pressure than histotripsy alone. Previous in vivo histotripsy study shows that tissue fractionation is always formed when a cavitation bubble cloud is generated and maintained in various organs such as prostate,[25] heart,[26] kidney,[27] and liver[28] in large animals. The observed reduction in the acoustic pressure necessary to generate and maintain a bubble cloud coupled with the sharp demarcation of the ablation zone exhibited by these nanodroplets are critical properties that indicate their potential for future in vivo use to allow selective ablation of specific lesions (e.g. solid tumors) where the nanodroplets will accumulate while neighboring healthy tissue will be preserved.
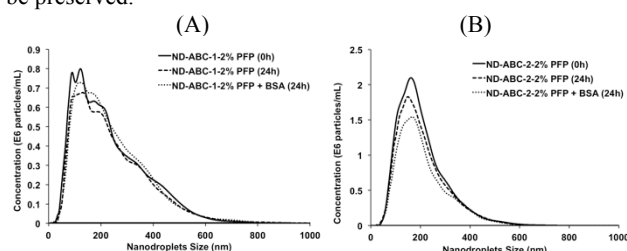

Figure 6. Effect of incubating (A) ND-ABC-1-2% PFP and (B) ND-ABC-2-2% PFP nanodroplets for 24 hours at 37ºC in the presence and absence of bovine serum albumin (BSA) as a model serum protein on droplets size and concentration.

We investigated the stability of nanodroplets prepared using ABC-1 and ABC-2 polymers and loaded with 2% v/v PFP upon incubation for 24 hours at 37ºC in presence and absence of bovine serum albumin (20 µg/ml) as a model serum protein. Using NTA software, we measured the mode and mean size for each formulation at the beginning of the incubation time (0hr) and after 24 hours along with droplets concentration. Results show that the nanodroplets prepared using ABC-1 polymer have an initial mode and mean size of 131.3±10.9nm and 237.35±6.1nm, respectively (**Table 3 & Figure 6, Panel A**). Incubating the droplets at 37ºC for 24 hours caused a slight shift in mode size and mean size to 142.0±10.5nm and 243.9±6.0nm, respectively. Incubating the nanodroplets with BSA did not affect nanodroplets mode size (144.5±13.9nm) and mean size (242.6±4.1nm), which indicates the success of the PEG brush displayed on droplets surface in suppressing BSA adsorption. Results also show that nanodroplets concentration did not change throughout the 24 hours incubation time in presence or absence of BSA, which indicates their stability against dissolution and aggregation. Analysis of mode and mean size of the nanodroplets prepared using ABC-2 and encapsulate 2% v/v PFP show that they maintained their size throughout the incubation time and in presence of BSA (**Table 3 & Figure 6, Panel B**). However, there was a 25% reduction in droplets concentration upon incubation with BSA for 24 hours, which is probably due to droplets dissolution or poor PFP encapsulation indicated by the low ablation capacity of these droplets shown in **Figure 4**. These results show that ND-ABC-1-2% PFP nanodroplets

resist the adsorption of serum proteins and are suited for in vivo testing.

Finally, we investigated the toxicity of ABC-1 and ABC-2 polymers towards PC-3 prostate cancer cells as a function of polymer concentration using the MTT assay (ATCC, Manassas, VA) following manufacturer's specifications. Briefly, we incubated PC-3 cells with ABC-1 and ABC-2 polymers formulated as empty nanodroplets (i.e. 0% loaded PFP) for 24 hours under normal culture conditions and compared the percentage of viable cells at each polymer concentration (0.3-75 µg/mL) to that observed for PC-3 cultured in normal culture medium (0 µg/mL polymer). Results show that the nanodroplets did not affect the viability of PC-3 cells at any of the tested concentrations (**Supplementary Information, Figure S15**) indicating their biocompatibility. We did not evaluate the toxicity of the PFP given that it is commonly used in FDA-approved ultrasound contrast agents and its concentration in the blood circulation drops by 90% within 10 minutes of its administration.[11]

To summarize, we have designed and synthesized two amphiphilic PEG-b-(PAA)-b-P(HDFMA-co-MMA) polymers (ABC-1 & ABC-2) that proved to encapsulate 1%-2% v/v PFP forming nanodroplets. Combining histotripsy pulses with nanodroplets formulated using ABC-1 and ABC-2 polymers proved to generate a cavitation bubble cloud that ablates neighboring RBCs at reduced acoustic pressure compared to histotripsy alone. The increase in PFP content from 1% to 2% v/v proved to increase the ablation lesion induced by the nanodroplets. Further, the nanodroplets formulated using ABC-1 appear to better encapsulate the loaded PFP and exhibit higher ablation capacity compared to those formulated by ABC-2 polymer at equal PFP loading. Based on the surface area of the ablation zone, ND-ABC-1-2% PFP nanodroplets exhibit effective ablation of RBCs at 2.5-fold lower acoustic pressure than the intrinsic threshold required to initiate the bubble cloud using the same 2-cycle histotripsy pulses alone. Furthermore, ND-ABC-1-2% PFP nanodroplets caused 60.9% of RBCs hemolysis comparing empty nanodroplets and PBS solution under the same histotripsy and physiological conditions. Further, these nanodroplets maintained their average size and concentration upon incubation with BSA for 24 hours at 37ºC, which prove their promise for cancer cell ablation and warrant their future testing in vivo.

[1]   a) N. Rapoport, Z. Gao, A. Kennedy, *J Natl Cancer Inst.* **2007**, *99*, 1095-1106. Epub 2007 Jul 1010, b) K. W. Ferrara, M. A. Borden, H. Zhang, *Acc Chem Res.* **2009**, *42*, 881-892, c) D. Phillips, X. Chen, R. Baggs, D. Rubens, M. Violante, K. J. Parker, *Ultrasonics* **1998**, *36*, 883-892, d) M. A. Wheatley, J. Lewandowski, *Mol Imaging.* **2010**, *9*, 96-107, e) Y. Uesugi, H. Kawata, J. Jo, Y. Saito, Y. Tabata, *J Control Release.* **2010**, *147*, 269-277. Epub 2010 Aug 2016, f) B. E. Oeffinger, M. A. Wheatley, *Ultrasonics* **2004**, *42*, 343-347, g) K. Hadinoto, *Int J Pharm.* **2009**, *374*, 153-161. Epub 2009 Mar 2024.
[2]   a) K. Kawabata, T. Maruoka, R. Asami, S. Umemura, *Jpn. J. Appl. Phys.* **2011**, *50*, b) N. R. Soman, S. L. Baldwin, G. Hu, J. N. Marsh, G. M. Lanza, J. E. Heuser, J. M. Arbeit, S. A. Wickline, P. H. Schlesinger, *J. Clin. Invest.* **2009**, *119*, 2830-2842, c) P. M.

Winter, K. Cai, S. D. Caruthers, S. A. Wickline, G. M. Lanza, *Expert. Rev. Med. Devices* **2007**, *4*, 137-145.

[3] M. Nishihara, K. Imai, M. Yokoyama, *Chem. Lett.* **2009**, *38*, 556-557.

[4] Z. Gao, A. M. Kennedy, D. A. Christensen, N. Y. Rapoport, *Ultrasonics* **2008**, *48*, 260-270.

[5] a) N. Rapoport, *Wiley Interdiscip. Rev. Nanomed. Nanobiotechnol.* **2012**, *4*, 492-510, b) K. Wilson, K. Homan, S. Emelianov, *Nat. Commun.* **2012**, *3*.

[6] N. Rapoport, Z. G. Gao, A. Kennedy, *J. Natl. Cancer Inst.* **2007**, *99*, 1095-1106.

[7] a) C. H. Wang, S. T. Kang, Y. H. Lee, Y. L. Luo, Y. F. Huang, C. K. Yeh, *Biomaterials* **2012**, *33*, 1939-1947, b) P. Zhang, T. Porter, *Ultrasound Med. Biol.* **2010**, *36*, 1856-1866, c) J. W. Huang, J. S. Xu, R. X. Xu, *Biomaterials* **2010**, *31*, 1278-1286, d) Y. Inaba, M. Tatsuya, S. Yoshizawa, S. Umemura, *Jpn. J. Appl. Phys.* **2011**, *50*.

[8] P. A. Dayton, T. O. Matsunaga, *Drug Dev. Res.* **2006**, *67*, 42-46.

[9] a) C. H. Wang, Y. F. Huang, C. K. Yeh, *Langmuir* **2011**, *27*, 6971-6976, b) S. A. Wickline, A. M. Neubauer, P. M. Winter, S. D. Caruthers, G. M. Lanza, *J. Magn. Reson. Imaging* **2007**, *25*, 667-680.

[10] S. H. Medina, G. Tiruchinapally, M. V. Chevliakov, Y. Y. Durmaz, R. N. Stender, W. D. Ensminger, D. S. Shewach, M. E. H. ElSayed, *Advanced Healthcare Materials* **2013**, n/a-n/a.

[11] K. Shiraishi, R. Endoh, H. Furuhata, M. Nishihara, R. Suzuki, K. Maruyama, Y. Oda, J. Jo, Y. Tabata, J. Yamamoto, M. Yokoyama, *Int. J. Pharm.* **2011**, *421*, 379-387.

[12] a) K. Kieran, T. L. Hall, J. E. Parsons, J. S. Wolf, Jr., J. B. Fowlkes, C. A. Cain, W. W. Roberts, *J Urol* **2007**, *178*, 672-676, b) F. Winterroth, Z. Xu, T. Y. Wang, J. E. Wilkinson, J. B. Fowlkes, W. W. Roberts, C. A. Cain, *Ultrasound Med Biol* **2011**, *37*, 78-86, c) Z. Xu, Z. Fan, T. L. Hall, F. Winterroth, J. B. Fowlkes, C. A. Cain, *Ultrasound Med Biol* **2009**, *35*, 245-255, d) Z. Xu, J. B. Fowlkes, C. A. Cain, *IEEE Trans Ultrason Ferroelectr Freq Control* **2006**, *53*, 1412-1424, e) Z. Xu, J. B. Fowlkes, E. D. Rothman, A. M. Levin, C. A. Cain, *J Acoust Soc Am* **2005**, *117*, 424-435.

[13] a) Z. Xu, Z. Fan, T. L. Hall, F. Winterroth, J. B. Fowlkes, C. A. Cain, *Ultrasound in Medicine & Biology* **2009**, *35*, 245-255, b) K. J. Carvell, T. A. Bigelow, *Ultrasonics* **2011**, *51*, 115-122, c) A. D. Maxwell, T.-Y. Wang, L. Yuan, A. P. Duryea, Z. Xu, C. A. Cain, *Ultrasound in Medicine & Biology* **2010**, *36*, 2132-2143, d) F. Winterroth, Z. Xu, T.-Y. Wang, J. E. Wilkinson, J. B. Fowlkes, W. W. Roberts, C. A. Cain, *Ultrasound in Medicine & Biology* **2011**, *37*, 78-86.

[14] G. R. Schade, J. Keller, K. Ives, X. Cheng, T. J. Rosol, E. Keller, W. W. Roberts, *The Journal of Urology* **2012**, *188*, 1957-1964.

[15] A. D. Maxwell, G. Owens, H. S. Gurm, K. Ives, D. D. Myers, Z. Xu, *J. Vasc. Interv. Radiol.* **2011**, *22*, 369-377.

[16] a) Z. Gao, A. M. Kennedy, D. A. Christensen, N. Y. Rapoport, *Ultrasonics* **2008**, *48*, 260-270. Epub 2007 Nov 2019, b) K. i. Kawabata, R. Asami, H. Yoshikawa, T. Azuma, S. i. Umemura, *Japanese Journal of Applied Physics* **2010**, *49*, 07HF20 (04 pp.), c) P. S. Sheeran, S. Luois, P. A. Dayton, T. O. Matsunaga, *Langmuir* **2011**, *27*, 10412-10420.

[17] a) Kripfgans Od, Fowlkes Jb, Miller Dl, Eldevik Op, Carson Pl, *Ultrasound Med. Biol.* **2000**, *26*, 1177-1189, b) P. S. Sheeran, V. P. Wong, S. Luois, R. J. McFarland, W. D. Ross, S. Feingold, T. O. Matsunaga, P. A. Dayton, *Ultrasound in Medicine and Biology* **2011**, *37*, 1518-1530.

[18] a) X. K. Sun, R. Rossin, J. L. Turner, M. L. Becker, M. J. Joralemon, M. J. Welch, K. L. Wooley, *Biomacromolecules* **2005**, *6*, 2541-2554, b) K. Nam, T. Kimura, A. Kishida, *Macromol. Biosci.* **2008**, *8*, 32-37.

[19] A. A. Deschamps, D. W. Grijpma, J. Feijen, *Polymer* **2001**, *42*, 9335-9345.

[20] P. S. Sheeran, S. Luois, P. A. Dayton, T. O. Matsunaga, *Langmuir* **2011**, *27*, 10412-10420.

[21] B. P. Bastakoti, S. H. Liao, M. Inoue, S. I. Yusa, M. Imura, K. Nakashima, K. C. W. Wu, Y. Yamauchi, *Sci Technol Adv Mater* **2013**, *14*.

[22] a) J. Y. Kim, J. K. Kim, J. S. Park, Y. Byun, C. K. Kim, *Biomaterials* **2009**, *30*, 5751-5756, b) A. N. Lukyanov, W. C. Hartner, V. P. Torchilin, *J. Control Release* **2004**, *94*, 187-193.

[23] A. D. Maxwell, T. Y. Wang, L. Q. Yuan, A. P. Duryea, Z. Xu, C. A. Cain, *Ultrasound Med. Biol.* **2010**, *36*, 2132-2143.

[24] A. D. Maxwell, C. A. Cain, T. L. Hall, J. B. Fowlkes, Z. Xu, *Ultrasound Med. Biol.* **2013**, *39*, 449-465.

[25] a) C. R. Hempel, T. L. Hall, C. A. Cain, J. B. Fowlkes, Z. Xu, W. W. Roberts, *J. Urol.* **2011**, *185*, 1484-1489, b) G. R. Schade, J. Keller, K. Ives, X. Cheng, T. J. Rosol, E. Keller, W. W. Roberts, *J. Urol.* **2012**, *188*, 1957-1964.

[26] Z. Xu, G. Owens, D. Gordon, C. Cain, A. Ludomirsky, *Circulation* **2010**, *121*, 742-749.

[27] a) W. W. Roberts, T. L. Hall, K. Ives, J. S. Wolf, J. B. Fowlkes, C. A. Cain, *J. Urol.* **2006**, *175*, 734-738, b) N. R. Styn, T. L. Hall, J. B. Fowlkes, C. A. Cain, W. W. Roberts, *Urology* **2012**, *80*, 724-729, c) T. L. Hall, K. Kieran, K. Ives, J. B. Fowlkes, C. A. Cain, W. W. Roberts, *J. Endourol.* **2007**, *21*, 1159-1165.

[28] E. Vlaisavljevich, Y. Kim, S. Allen, G. Owens, S. Pelletier, C. Cain, K. Ives, Z. Xu, *Ultrasound Med. Biol.* **2013**, *39*, 1398-1409.

Cell Ablation

Yasemin Yuksel Durmaz, Eli
Vlaisavljevich, Zhen Xu* Mohamed
ElSayed*

Development of Nanodroplets for
Histotripsy-Mediated Cell Ablation
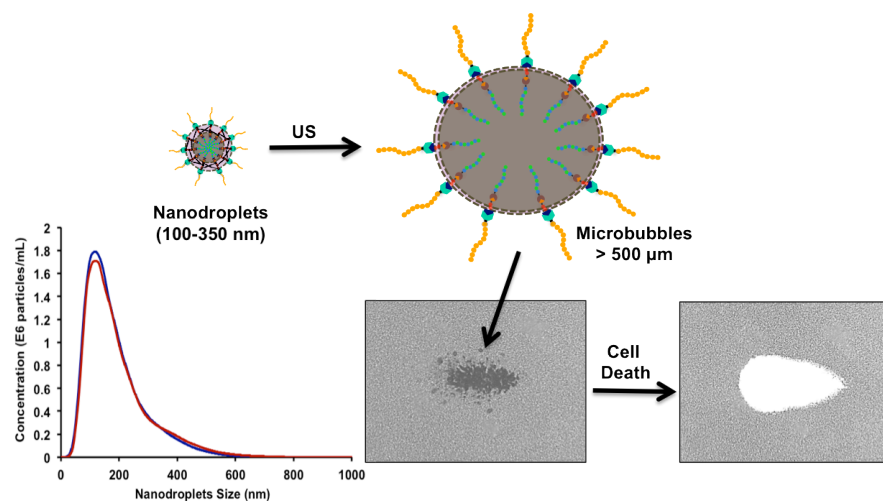
Combining histotripsy pulses with PFP-loaded nanodroplets proved to generate a cavitation bubble cloud that ablates neighboring red blood cells at reduced acoustic pressure compared to histotripsy alone. The increase in PFP content proved to increase the size of the ablation zone induced by the nanodroplets. Further, these nanodroplets maintained their average size and concentration upon incubation with serum protein, which prove their promise for *in vivo* ablation of cancer cells.

8. SUPPORTING DATA

1. EXPERIMENTAL SECTION

1.1 Materials

Methyl methacrylate (MMA, Sigma-Aldrich, 99 %), 3,3,4,4,5,5,6,6,7,7,8,8,9,9,10,10,10-heptadecafluorodecyl methacrylate (HDFMA, Sigma-Aldrich, 97 %), *tert*-butyl acrylate (*t*BA, Sigma-Aldrich, 98 %) and *N, N, N', N'', N''*-pentamethyldiethylenetriamine (PMDETA, Sigma-Aldrich, 99 %,) were passed through basic alumina column to remove the inhibitor. *N*-(*n*-Pentyl)-2-pyridylmethanimine was synthesized according to the literature procedure.(*11*) Copper (I) bromide (CuBr, Sigma-Aldrich, 99.9 %), 2-bromoisobutyryl bromide (Fluka, >97 %), tetrahydrofuran anhydrous (THF, Sigma-Aldrich, >99.9 %), *N,N'*-Dicyclohexylcarbodiimide (DCC, Sigma-Aldrich, 99 %), dimethylaminopyridine (DMAP, Acros, 99 %), 4-pentynoic acid (Sigma-Aldrich, 99 %), furan (Sigma-Aldrich, ≥99 %), maleic anhydride (Fluka, ≥99 %), 9-anthracene methanol (Aldrich, ≥ 99%), perfluoropentane (PFC, Alfa Aesar, 97% ca. 85% n-isomer), *N*-hydroxy succinimide (NHS, Fluka, 97 %), *N*-(3-Dimethylaminopropyl)-*N'*-ethylcarbodiimide hydrochloride (EDC, Fluka >98 %), poly(ethylene glycol) monomethylether (Me-PEG, M_n : 2000 and 5000, Sigma-Aldrich), sodium azide (NaN$_3$, Acros, 99 %), 2-(*N*-morpholino)ethanesulfonic acid monohydrate (MES, Acros, 99 %), triethylamine (TEA, Sigma-Aldrich, ≥99%), trifluoroacetic acid (TFA, Acros, 99 %), ethylene carbonate (Sigma-Aldrich, 98 %), 2,2`-(ethylenedioxy)-bis(ethylamine) (Sigma-Aldrich, 98%) agarose powder (Type VII; Sigma-Aldrich), citratephosphate-dextrose (CPD, Sigma-Aldrich) were used as received. RPMI medium 1640, fetal bovine serum (FBS), 0.25% trypsin/0.20% ethylene diamine teraacetic acid (EDTA), phosphate buffered saline (PBS), penicillin/streptomycin/amphotericin, sodium pyruvate, and non-essential amino acid solutions were purchased from Invitrogen Corporation (Carlsbad, CA). MTT Assay Kit was purchased from American Type Culture Collection (Manassas, VA). T-75 flasks, Costar 96-well plates, and cell culture supplies were purchased from Corning Inc. (Corning, NY).

1.2 Characterization

^{1}H NMR and ^{13}C NMR spectra of 5–10 % (w/w) solutions in CDCl$_3$ or D$_2$O with Si(CH$_3$)$_4$ as an internal standard were recorded using 400 MHz and 500 MHz Varian Mercury system (Palo Alto, CA) at room temperature, respectively. Gel permeation chromatography (GPC) measurements were obtained from a Viscotek GPCmax Autosampler system consisting of a pump and Water 2414 refractive index (RI) detector. The molecular weight and molecular weight distribution of final polymers were determined based on their elution volume on an Styragel HR 4E column compared to a series of poly(methyl methacrylate) standards (PolyAnalitik Inc, Canada) using THF as a mobile phase at a flow rate of 1 ml/min at 35 ^{o}C. Data were analyzed using Viscotek OmniSEC Omni-01 software. FT-IR spectra were recorded on a Perkin-Elmer FT-IR Spectrum 4100 type A. Differential scanning calorimetry (DSC) was performed on Perkin-Elmer Diamond DSC calibrated with indium. Glass transition temperatures were measured, after a first heating (from 20 ^{o}C to 120 °C) and cooling (from 120 °C to 20 ^{o}C) cycle. Thermograms were recorded during the second heating cycle (from 20 to 120 ^{o}C) at 10 °C/min under nitrogen flow and the glass transition temperature (T_g) was determined at the midpoint between upper and lower intersection of the baseline with the tangent to the transition step. Micelles size were measured using Dynamic Light Scattering (DLS) 90Plus particle size analyzer with ZetaPALS capability (Brookhaven Instruments Corporation, Holtsville, NY) and Nanoparticle Tracking Analyzer (NTA) with Nanosight NS500 (Nanosight, Amesbury, United Kingdom) equipped with a sample chamber with a 640 nm laser and a fluoroelastomer O-ring at 22 ^{o}C. Each sample was analyzed for six times. NTA 2.3 Build 127 was used as software to capture and analyzing the data. The samples were measured for 60 second with manual shutter and gain adjustments. NTA software was also used for concentration (number of particles/mL) calculation. The morphology of micelle was observed by a FEI Quanta 3D Dual-Beam SEM Environment Scanning Electron Microscope (FEI, Oregon, USA). A drop of micelle solution was deposited onto silicon chip mounted on aluminium stub. The samples were imaged under 5.2 Torr at 1.3 ^{o}C.

1.3 Synthesis of Amphiphilic Block Copolymer

1.3.1 Synthesis of Alkyne Functional Poly(ethylene glycol) (Alkyne-PEG)

PEG_{2000} (5.0 g, 2.5 x 10^{-3} mol) and 4-pentynoic acid (0.367 g, 3.75 x 10^{-3} mol) were dissolved in 25 mL of CH_2Cl_2. DMAP (0.308 g, 2.5 x 10^{-3} mol) and a solution of DCC (0.770 g, 3.75 x 10^{-3} mol) in 10 mL of CH_2Cl_2 were successively added to the reaction mixture followed by stirring overnight at room temperature. After filtration of the salt, the solution was concentrated and solution of alkyne-PEG was precipitated in diethyl ether tree times and filtered. (Yield: 3.86 g). Functionalization efficiency: 92 %. ^1H NMR (500 MHz, CDCl$_3$, δ): 4.26 9 (t, 2H, CO-O-CH_2), 3.71 (t, 2H CO-O-CH$_2$-CH_2-O), 3.65 (bs, 180H, OCH_2CH$_2$), 3.38 (s, 3H, O-CH_3), 2.58 (2H, CH$_2$CH_2-CO-O), 2.51 (2H, CH$_2$CH_2-CO-O), 1.99 (1H, alkyne proton).

1.3.2 Synthesis of 9-anthyrylmethyl 2-bromo-2-methyl propanoate

9-anthyrylmethyl 2-bromo-2-methyl propanoate was synthesized by following literature.(*12*) 9-Anthracene methanol (1.50 g, 7.18 mmol) and DMAP (0.175 g, 1.44 mmol) were dissolved in 50 mL of CH_2Cl_2, and Et$_3$N (1.2 mL, 8.6 mmol) was added. The reaction mixture was then cooled to 0 ^{o}C. 2-bromo isobutyryl bromide (1.82 g, 7.89 mmol) was added dropwise within 30 minutes to this solution. The reaction mixture was stirred for 15 min at 0 ^{o}C then for overnight at room temperature. The ammonium salt was filtered off and the solvent was evaporated under reduced pressure. The remaining residue was extracted with CH_2Cl_2, and saturated aqueous NaHCO$_3$ and combined organic phases dried over Na$_2$SO$_4$. The solution was concentrated, and the crude product was purified by column chromatography over silica gel eluting with hexane/EtOAc (10:1) to give product as yellow solid. Yield: 2.15 g (84 %). EIMS *m/z* 379.0 for [M + Na]+ C$_{19}$H$_{17}$O$_2$BrNa calculated 379.04. ^1H NMR (500 MHz, CDCl$_3$, δ): 8.55 (s, 1H, ArH of anthracene), 8.35 (d, *J* = 8.99 Hz, 2H, ArH of anthracene), 8.05 (d, *J* = 8.49 Hz, 2H, ArH of anthracene), 7.60-7.45 (m, 4H, ArH of anthracene), 6.24 (s, 2H, CH_2-anthracene), 1.89 (s, 6H, C(CH_3)$_2$-Br). ^{13}C NMR (CDCl$_3$, δ): 172, 131.3, 131.1, 129.4, 129.1, 126.7, 125.5, 125.1, 123.9, 69.7, 55.9, 30.7.

1.3.3 Synthesis of Anthracene Functional Poly(tert-Butyl Acrylate) (Anth-PtBA-Br)

CuBr (97.8 mg, 6.82 x 10^{-4} mol), PMDETA (142.4 μL, 6.82 x 10^{-4} mol), anthracene functional initiator (0.244, 6.82 x 10^{-4} mol) as an initiator, *t*-BA (10 mL, 6.82 x 10^{-2} mol), and ethylene carbonate (10% w/w, 0.92 g) were introduced in a round bottom flask (50 mL) under the argon. The mixture was degassed by three freeze–pump–thaw cycles and left argon atmosphere at 80°C for 90 min. After the given time, the mixture was diluted with THF. Then the copper complex was removed out by passing through a neutral alumina column, and THF was removed by rotary evaporation. The mixture was precipitated in cold methanol/water (80/20 v/v). After decantation, the polymer was dissolved in CH_2Cl_2, extracted with water and the water phase was again extracted with CH_2Cl_2 and combined organic phase was dried over Na$_2$SO$_4$. Finally, the organic phase was evaporated to give anthracene functional poly(*tert*-butyl acrylate). Conversion: 9 %, $M_{n,theo}$: 1510 g/mol, $M_{n,NMR}$: 1640 g/mol, $M_{n,GPC}$: 2000 g/mol, M_w/M_n: 1.26. ^1H NMR (500 MHz, CDCl$_3$, δ): 8.51 (s, 1H, ArH of anthracene), 8.40 (d, 2H, ArH of anthracene), 8.04 (d, *J* = 8.49 Hz, 2H, ArH of anthracene), 7.58-7.50 (m, 4H, ArH of anthracene), 6.12 (s, 2H, CH_2-anthracene), 4.11 (CH$_2$CH-Br), 2.26 (CH$_2$CH-CO), 1.86 (6H, O-CO-C(CH_3)$_2$), 1.45 (9H, CO-O-C(CH_3)$_3$).

1.3.4 Azidation of Anthracene Functional Poly(tert-butyl acrylate) (Anth-PtBA-N₃)

Anth-P*t*BA-Br (0.5g, 3.04 x 10^{-4} mol) and 20 equivalent NaN$_3$ (0.396 g, 6.09 x 10^{-3} mol) were stirred in DMF at 50 ^{o}C for overnight. The polymer was dissolved in CH_2Cl_2, extracted with water and the water phase was again extracted with CH_2Cl_2 and combined organic phase was dried over Na$_2$SO$_4$. Finally, the organic phase was evaporated to give anthracene functional azide terminated P(*t*BA). ^1H NMR (500 MHz, CDCl$_3$, δ): 8.51 (s, 1H, ArH of anthracene), 8.39 (d, *J* = 8.49 Hz, 2H, ArH of anthracene), 8.05 (d, *J* = 8.99 Hz, 2H, ArH of anthracene), 7.58-7.50 (m, 4H, ArH of anthracene), 6.12 (s, 2H, CH_2-anthracene), 3.77 (CH$_2$CH-N$_3$), 2.26 (CH$_2$CH-CO), 1.86 (6H, O-CO-C(CH_3)$_2$), 1.45 (9H, CO-O-C(CH_3)$_3$).

1.3.5 Synthesis of 2-bromo-2-methyl-propionic acid 2-(3,5-dioxo-10-oxa-4 azatricyclo [5.2.1.02,6]dec-8-en-4-yl) ethyl ester (protected maleimide functional initiator)

Protected-maleimide functional initiator was synthesized by following literature.(*13*) Maleic anhydride (10.0 g, 0.1 mol) was suspended in 30 mL of toluene and the mixture warmed to 80 °C. Furan (11.3 mL, 0.15 mol) was added via syringe and the turbid solution was stirred for overnight. The mixture was then cooled to ambient temperature white solids formed during standing were collected by filtration and washed with 2 × 30 mL of diethyl ether afforded 3a,4,7,7a-tetrahydro-4,7-epoxyisobenzofuran-1,3-dione as white needless. Yield: 12.35 g (74 %). ^{1}H NMR (500 MHz, CDCl$_3$, δ) 6.55 (s, 2H, C*H*=C*H*, bridge protons), 5.45 (s, 2H, -C*H*O, bridge-head protons), 3.15 (s, 2H, C*H*-C*H*, bridge protons). ^{13}C NMR (CDCl$_3$, δ): 169.9, 137.0, 82.2, 48.7.

3a,4,7,7a-tetrahydro-4,7-epoxyisobenzofuran-1,3-dione (10.0 g, 60.0 mmol) was suspended in methanol (150 mL) and the mixture cooled to 0 °C. A solution of ethanolamine (3.6 mL, 60 mmol) in 30 mL of methanol was added dropwise (10 min) to the reaction mixture, and the resulting solution was stirred for 5 min at 0 °C, then 30 min at ambient temperature, and finally refluxed for 6 h. After cooling the mixture to ambient temperature, solvent was removed under reduced pressure, and residue was dissolved in 150 mL of CH$_2$Cl$_2$ and washed with 3 × 100 mL of water. The organic layer was separated, dried over Na$_2$SO$_4$ and filtered. Removal of the solvent under reduced pressure gave white-off solid which was further purified by flash chromatography eluting with ethylacetate (EtOAc) to give the product, 2-(2-hydroxyethyl)-3a,4,7,7a-tetrahydro-1H-4,7-epoxyisoindole-1,3(2H)-dione as a white solid. Yield: 3.3 g (27%). ^{1}H NMR (500 MHz, CDCl$_3$, δ): 6.53 (s, 2H, C*H*=C*H*, bridge protons), 5.29 (s, 2H, -C*H*O, bridge-head protons), 3.79-3.70 (m, 4H, NC*H$_2$*C*H$_2$*OH), 2.90 (s, 2H, C*H*-C*H*, bridge protons). ^{13}C NMR (500 MHz, CDCl$_3$, δ): 176.8, 136.5, 80.9, 60.1, 47.5, 41.7.

3a,4,7,7a-tetrahydro-1H-4,7-epoxyisoindole-1,3(2H)-dione (2.0 g, 9.55 mmol) and Et$_3$N (1.44 mL, 10.54 mmol) in 100 mL of THF were added in a 250 mL of round bottom flask. The mixture was cooled to 0 °C, and a solution of 2-bromo isobutyryl bromide (2.34 g, 10.0 mmol) in 25 mL of THF was added dropwise (30 min) to the reaction mixture. The white suspension was stirred for 3 h at 0 °C and subsequently at ambient temperature for overnight. The ammonium salt was filtered off and the solvent was removed under reduced pressure to give a pale-yellow residue that was further purified by column chromatography over silica gel eluting with EtOAc /hexane (1:4) to give protected maleimide functional initiator as a white solid. Yield: 2.5 g (91%). EIMS *m/z* 338.0 for [M + Na]+ C$_{14}$H$_{16}$NO$_5$BrNa calculated 380.02. ^{1}H NMR (500 MHz, CDCl$_3$, δ) 6.52 (s, 2H, C*H*=C*H*, bridge protons), 5.27 (s, 2H, -C*H*O, bridge-head protons), 4.33 (t, *J* = 10.5 Hz, 2H, NCH$_2$C*H$_2$*OC=O), 3.77 (t, *J* =10.5 Hz, 2H, NC*H$_2$*CH$_2$OC=O), 2.87 (s, 2H, C*H*-C*H*, bridge protons), 1.90 (s, 6H, C(C*H$_3$*)$_2$-Br). ^{13}C NMR (500 MHz, CDCl$_3$, δ): 175.8, 171.3, 136.5, 80.8, 62.1, 55.6, 47.4, 37.5, 30.5.

1.3.6 Synthesis of Protected Maleimide Functional Poly(heptadecafluorodecyl methacrylate-co-methyl methacrylate) (PMI-P(HDFMA-co-MMA)-Br)

CuBr (33.5 mg, 2.33 x 10^{-4} mol), *N*-(*n*-pentyl)-2-pyridylmethanimine (86.5µL, 4.68 x 10^{-4} mol), protected maleimide functional initiator (83.3, 2.23 x 10^{-4} mmol), MMA (2 mL, 1.87 x 10^{-2} mol), HDFMA (2.07 mL, 4.65 x 10^{-3}) and 3.5 mL Toluene were introduced in a Schlenk tube under argon. The tube was heated at 90 ^{o}C in an oil bath and stirred 1h 40 min. Then the mixture was diluted with THF, and passed through an alumina column to remove the complex salts. Precipitation of the polymer was performed in a ten-fold volume of heptane. The solid was then collected after filtration. Conversion: 25.4 %, $M_{n,theo}$: 5100 g/mol, $M_{n,NMR}$: 6720 g/mol, $M_{n,GPC}$: 5930 g/mol, M_w/M_n: 1.15. ^{1}H NMR (500 MHz, CDCl$_3$, δ): 6.54 (s, 2H, C*H*=C*H*), 5.28 (s, 2H, -C*H*O), 4.47 (t, 2H, NCH$_2$C*H$_2$*OC=O), 4.26 (bs, CO-O-C*H$_2$*-CH$_2$-CF$_2$), 3.77 (t, 2H, NC*H$_2$*CH$_2$OC=O), 3.60 (bs, CO-O-C*H$_3$*), 2.90 (s, 2H, C*H*-C*H)*, 2.49 (bs, CO-O-CH$_2$-C*H$_2$*-CF$_2$), 2.05-0.85 (m, *CH$_2$*-CC*H$_3$*, CO-*(CH$_3$)$_2$*). ^{19}F NMR (470 MHz, CDCl$_3$, δ):-80.8, -113.5, -121.9, -122.7, -123.6, -121.1.

1.3.7 Synthesis of Poly[(ethylene glycol-b-(tert-butyl acrylate)-b-(heptadecafluorodecyl methacrylate-co-methyl methacrylate)] Triblock Copolymer via one-pot Diels-Alder/Copper Catalyzed Azide-Alkyne Cycloaddition Reaction (PEG-b-PtBA-b-P(HDFMA-co-MMA))

Briefly, protected maleimide functional (HDFMA-*co*-MMA) (0.182 g, 2.70 x 10^{-5} mol), Anth-PtBA-N$_3$ (0.050 g, 3.03 x 10^{-5} mol), and Alkyne-PEG (0.071 g, 3.03 x 10^{-5} mol) were dissolved in Toluene (10 mL) in a Schlenk tube. CuBr (5.21 mg, 3.63 x 10^{-5} mol) and PMDETA (7.6 µL, 3.63 x 10^{-5} mol) were added, and the reaction mixture was degassed by three freeze-pump-thaw cycles and stirred at 110 °C for 48 h. The mixture was passed through alumina column to remove copper catalyst using THF as an eluent. Concentrated polymer solution was precipitated in hexane. The product was reprecipitated from CH$_2$Cl$_2$/hexane and cold methanol to remove excess homopolymers. (Yield: 90 mg) ^{1}H NMR (500 MHz, CDCl$_3$, δ): 7.58-7.19 (8H, aromatic

protons), 5.47-5.29 (3H, CH$_2$-C*H*-triazole and CO-O-C*H$_2$*-cycloadduct), 4.78 (2H, C*H* bridge protons), 4.24 (CO-O-C*H$_2$*-CH$_2$-CF$_2$), 3.78 (2H, CO-O-C*H$_2$*-CH$_2$-N), 3.63 (OC*H$_2$*CH$_2$), 3.47 (CO-O-C*H$_3$*), 3.38 (3H, OCH$_2$CH$_2$O-C*H$_3$*), 3.28 (4H, CO-O-CH$_2$-C*H$_2$*-N and CH bridge protons of cycloadduct), 3.02 (2H, triazole-C*H$_2$*-CH$_2$-CO-O), 2.75 (2H, triazole-CH$_2$-C*H$_2$*-CO-O), 2.47 (CO-O-CH$_2$-C*H$_2$*-CF$_2$), 2.25 (CH$_2$C*H*-CO), 2.03-0.84 (O-CO-C(C*H$_3$*)$_2$, CO-O-C(C*H$_3$*)$_3$ and rest of the backbone protons).

1.3.8 Synthesis of Poly[(ethylene glycol-b-(acrylic acid)-b-(heptadecafluorodecyl methacrylate-co-methyl methacrylate)] Triblock Copolymer (PEG-b-PAA-b-P(HDFMA-co-MMA))

To be able to obtain acid functionality in the middle block, *tert*-butyl groups were hydrolyzed using TFA. PEG-*b*-(P*t*BA)-*b*-P(HDFMA-*co*-MMA) copolymer was dissolved in dichloromethane and 10 fold excess of TFA (equivalent to *tert*-butyl group) was added at 0 °C under argon atmosphere. Reaction mixture was stirred 30 min at this temperature and 24 h stirred at room temperature. Dichloromethane and TFA were evaporated with air stream and PEG-*b*-(PAA)-*b*-P(HDFMA-*co*-MMA) was precipitated in methanol. ^{1}H NMR (500 MHz, CDCl$_3$, δ): 7.58-7.19 (8H, aromatic protons), 5.47-5.29 (3H, CH$_2$-C*H*-triazole and CO-O-C*H$_2$*-cycloadduct), 4.78 (2H, C*H* bridge protons), 4.24 (CO-O-C*H$_2$*-CH$_2$-CF$_2$), 3.78 (2H, CO-O-C*H$_2$*-CH$_2$-N), 3.63 (OC*H$_2$*CH$_2$), 3.47 (CO-O-C*H$_3$*), 3.38 (3H, OCH$_2$CH$_2$O-C*H$_3$*), 3.28 (4H, CO-O-CH$_2$-C*H$_2$*-N and CH bridge protons of cycloadduct), 3.02 (2H, triazole-C*H$_2$*-CH$_2$-CO-O), 2.75 (2H, triazole-CH$_2$-C*H$_2$*-CO-O), 2.47 (CO-O-CH$_2$-C*H$_2$*-CF$_2$), 2.25 (CH$_2$C*H*-CO), 2.03-0.84 (O-CO-C(C*H$_3$*)$_2$, and rest of the backbone protons).

1.4 Preparation of PFP Encapsulated Nanodroplets

Self–assembly of amphiphilic fluorinated triblock copolymers in the presence of PFP was resulted in PFP encapsulated nanodroplets, since hydrophobic PFP prefers to stay in hydrophobic core of nanosized self-assembly. PFP is most common used PFC with boiling point of 29 °C, which is close to room temperature. In order to minimize PFP evaporation, each step of nanodroplets preparation was performed in ice bath (**Figure 1, Panel B**). PEG-*b*-(PAA)-*b*-P(HDFMA-*co*-MMA) copolymers were dissolved in tetrahydrofuran (THF) (0.2 % w/v) and cooled down to 0 °C before addition of PFP (1 or 2% v/v). Equal amount of water was slowly added to this solution mixture to trigger micelle formation and mixture was stirred for 1h in ice bath. The solution was transferred into a dialysis bag (MWCO of 1 KDa) and dialyzed against ice-cold MES solution or water to remove THF. After 12 hours of dialysis, slightly milky solution of PFP encapsulated noncross-linked nanodroplets was obtained. These nanodroplets were further reacted with 2,2`-(ethylenedioxy)-bis(ethylamine) via NHS/EDC coupling (2/4 equivalent of COOH groups) to obtain cross-linked shell. Briefly, 5mL of this nanodroplets solution (3.18 x 10^{-7} mol of ABC-1, 3.02 x 10^{-7} mol of carboxylic acid groups) was transferred into round bottom flask. 121.1 µl of NHS solution (6.05 x 10^{-6} mol, 50 mM solution in 100 mM MES buffer pH: 5.5) and 242.2 µl of EDC solution (1.21 x 10^{-6} mol, 50 mM solution in 100 mM MES buffer pH: 5.5) were added to nanodroplets solution and stirred for 45 min followed by addition 151.4 µl of 2,2`-(ethylenedioxy)-bis(ethylamine) as a cross-linker (1.51 x 10^{-6} mol, 10 mM solution in PBS buffer pH: 7.4). After 6 h stirring in ice bath, nanodroplets solution was transferred into a dialysis bag to remove buffer impurities. Nanodroplets size was monitored using DLS before and after crosslinking.

1.5 Characterization of Nanodroplets

Self-assembly of amphiphilic triblock copolymers without PFP forms nano-sized micelles. In the presence of PFP, these micelles have hydrophobic liquid (PFP) in their core, which makes them nanodroplets. Micelles and nanodroplets size were measured using both Dynamic Light Scattering (DLS) 90Plus particle size analyzer with ZetaPALS capability (Brookhaven Instruments Corporation, Holtsville, NY) and Nanoparticle Tracking Analyzer (NTA) methods at 22 °C and 37 °C. DLS was used as most common size measurement techniques, which allowed us to monitor our preparation process before and after critical points such as PFP encapsulation and shell cross-linked. NTA was used not only for size measurement but also for determination of particle concentration. The technique combines light scattering microscopy with camera, which enables visualization and recording of Brownian motion of nanoparticles in solution, which allows later evaluating their size and concentration. NTA measurements were performed with Nanosight NS500 (Nanosight, Amesbury, United Kingdom) equipped with a sample chamber with a 640 nm laser and a fluoroelastomer O-ring at 22 °C. Each sample was analyzed for six times. NTA 2.3 Build 127 was used as software to capture and analyzing the data. The samples were measured for 60 second with manual shutter and gain adjustments. The error bars were obtained by the standard deviation of the different measurements of each sample. The mean size and standard deviation values were obtained by the NTA software correspond to arithmetic values calculated with the sizes

of the all particles analyzed by the software. The error bars displayed on the DLS graphs were obtained by the standard deviation of minimum three different samples. All statistical evaluations were carried out with unpaired two-tailed Student's t-tests. A p-value of less than 0.05 ($p < 0.05$) was considered significant.

1.6 Ablation of Red Blood Cells in Tissue Phantoms

Agarose gel phantoms with an embedded red blood cell (RBC) layer were used to demonstrate the ability of using nanodroplets to mechanically ablate tissue.(7) This phantom provides a thin, translucent red layer of RBCs as a visual indicator between the two transparent agorose gel layers that locally appears more transparent when RBCs layer is damaged. Tissue phantoms were prepared using a mixture of agarose powder (Type VII; Sigma-Aldrich Co., St. Louis, Missouri, USA) and canine RBCs in 0.9% isotonic saline. Fresh canine blood was obtained from adult research subjects in an unrelated study and added to an anticoagulant solution of citratephosphate- dextrose (CPD, Sigma-Aldrich Co.) with a CPD-to-blood ratio of 1:9 mL. Whole blood was separated in a centrifuge at 3000 rpm for 10 min. The plasma and white buffy coat were removed, and the RBCs were saved for addition to the phantom.

Agarose was slowly combined with saline while stirring at 20 °C (1.5% w/v agarose/saline), forming a translucent solution. The solution was heated in a microwave oven for 30 s and then stirred. Heating at 30 s intervals and stirring was repeated until the solution turned entirely transparent. The solution was then placed under a partial vacuum of 20.5 psi for 30 min to degas the mixture. After removing the mixture from the vacuum, mixture was cooled to 37 °C and PFP encapsulated micelles were added to experimental phantom for comparison with 1 or 2% PFP encapsulated nanodroplets and micelles phantoms. A layer of these phantom mixtures were then poured into a rectangular polycarbonate housing to fill half of it. The housing was placed in a refrigerator at 4 °C to allow the agarose to cool and solidify. The remaining agarose solution was kept at 37°C. A small amount of agarose solution was mixed with the RBCs (5% RBCs v/v). The frame with solidified agarose was removed from refrigeration, and a thin layer of the RBC-agarose solution was poured onto the gel surface to allow the entire surface to coat in a thin layer. After 5 min, the RBC-agarose layer was solidified, and the remaining agarose solution without RBCs was poured to completely fill the frame. This procedure created a thin layer of RBCs suspended in the center of the agarose phantom.

The focus of a 32 element 500 kHz transducer was aligned with the center of the red blood cell phantom layer. Histotripsy pulses were applied at a pulse repetition frequency of 10 Hz at peak negative pressures of 11.0, and 20.7, MPa to the center of phantoms containing red blood cell layer embedded with PFP encapsulated micelles, and empty micelles. Red blood cell fractionation was monitored using a high-speed, 1 megapixel CCD camera (Phantom V210, Vision Research) capable of a maximum frame rate of 2000 fps. The camera was focused to the red blood cell layer and backlit by a continuous light source. The camera was triggered to record two images for each applied pulse, one 10 μs after the pulse reached the focus to visualized the bubble activity and another frame was captured between pulses to assess tissue damage. The camera exposure time was 10 μs. The bubbles appeared as black regions in the shadow graphic image while red blood cell fractionation was visualized, as red blood cells turn transparent after fractionation. Tissue fraction was compared between RBC phantoms with nanodroplets, and micelles as controls.

1.7 Cytotoxicity of Micelles Prepared Using ABC-1 and ABC-2 Copolymer

Briefly, PC-3 cells were seeded in 96-well plates at a seeding density of 1×10^5 cells/well and allowed to adhere overnight before replacing the culture medium with RPMI medium 1640 solution (without phenol red) containing different concentration of micelles and incubating for 24 h under normal culture conditions. The cells were then exposed to 10 μL MTT reagent included in the assay kit following the manufacturer's guidelines, for 2 hours which results in reduction of MTT reagent to purple formazan precipitate. MTT reagent detergent (100 μL) was added to each well and incubated for 3 h in dark at room temperature, followed by measuring the absorbance of this mixture at 570 nm using a Multiskan microplate reader (Thermo Fisher Scientific Inc., Waltham, MA). Contribution of free culture medium was eliminated by subtracting the absorbance of equal volume of culture medium at this wavelength. PC-3 cells with RPMI1640culture medium (untreated cells) and 5% v/v Triton X-100 solution were used as negative and positive controls, respectively. The micelles concentrations that result in statistically different than untreated cell were considered cytotoxic.

1.8 Stability of Nanodroplets

The stability of the nanodroplets and its interaction with bovine serum albumin (BSA) have been investigated by incubating them in BSA solution at 37 °C. Typically, 0.366 mg/mL of nanodroplets solution of

each block copolymer were placed in contact with the model proteins at concentrations of 20 µg/mL of BSA. Nanodroplets size and concentration were measured before and after (24h later) incubation using NTA.
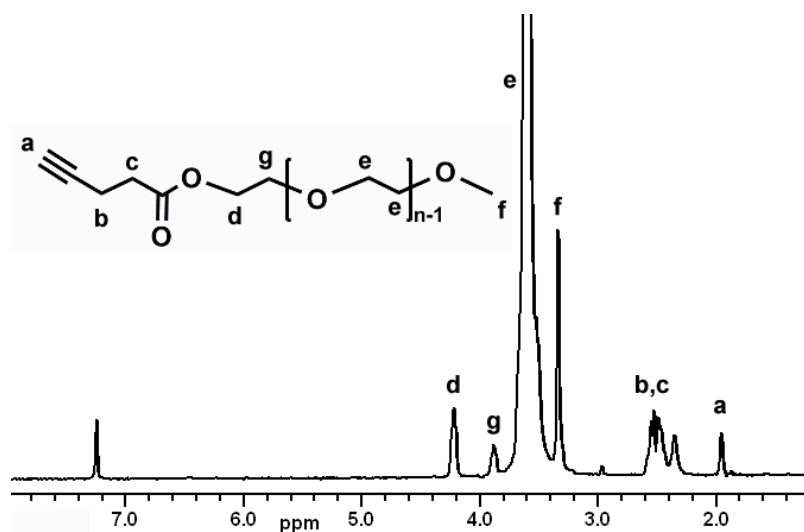
NMR Spectra
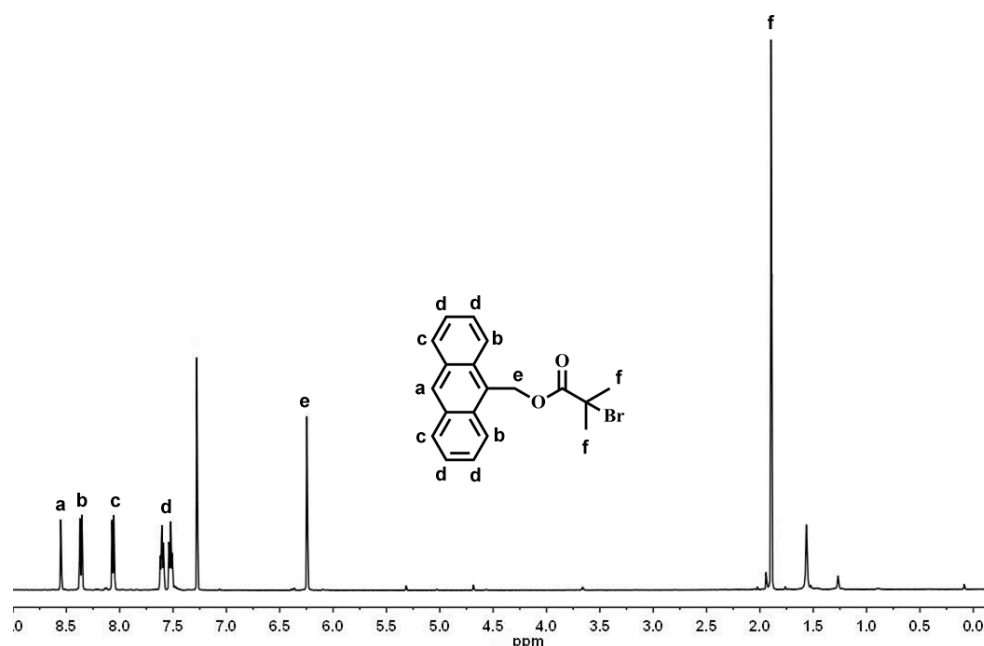

Figure S1. ^{1}H NMR spectrum of alkyne-PEG in CDCl$_3$.

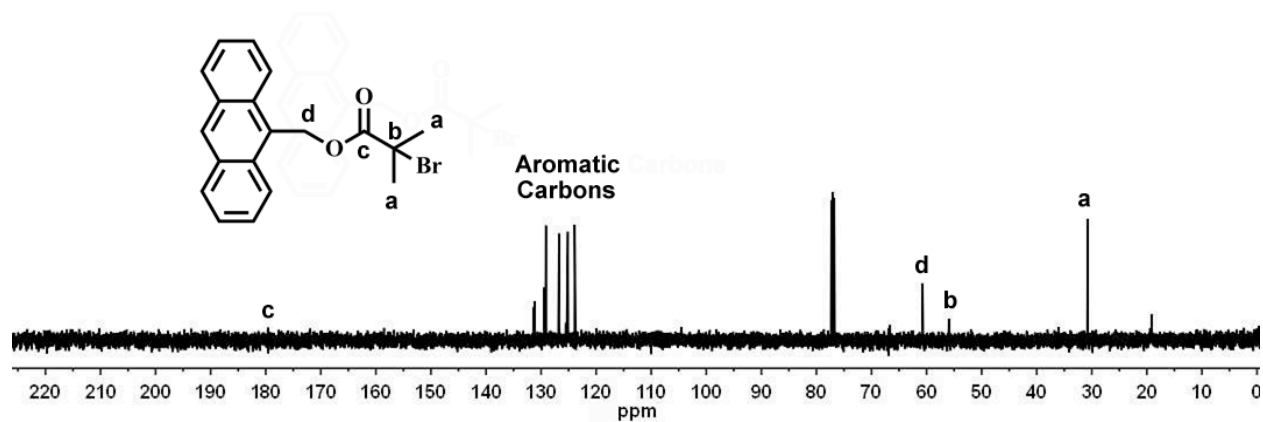**Figure S2.** ^{1}H NMR spectrum of anthracene functional ATRP initiator in CDCl$_3$.

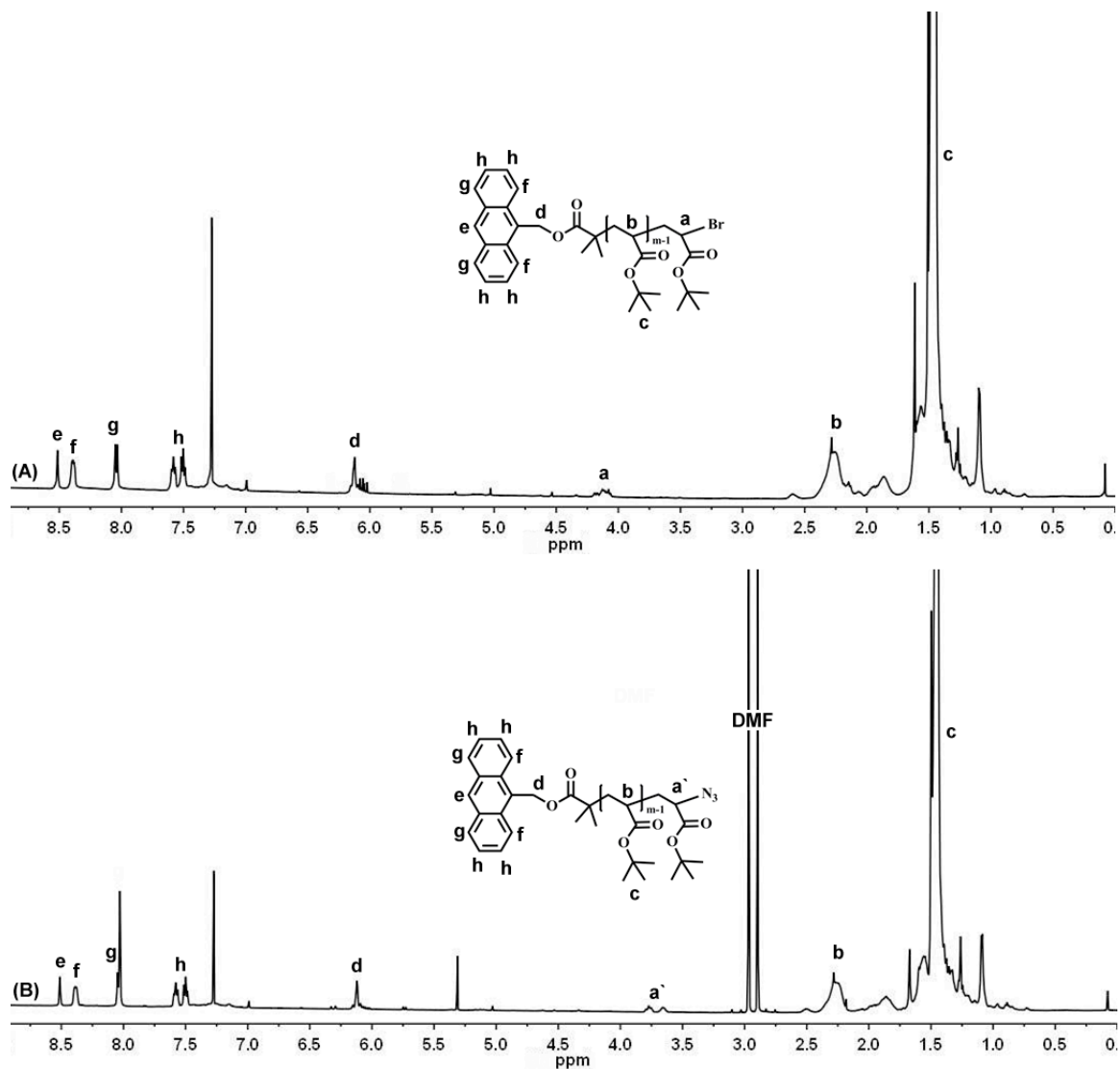**Figure S3.** ^{13}C NMR spectrum of anthracene functional ATRP initiator in CDCl$_3$.

Figure S4. ^{1}H NMR spectrum of Ant-P*t*BA-Br (A) and Ant-P*t*BA-N$_3$ (B) in CDCl$_3$.
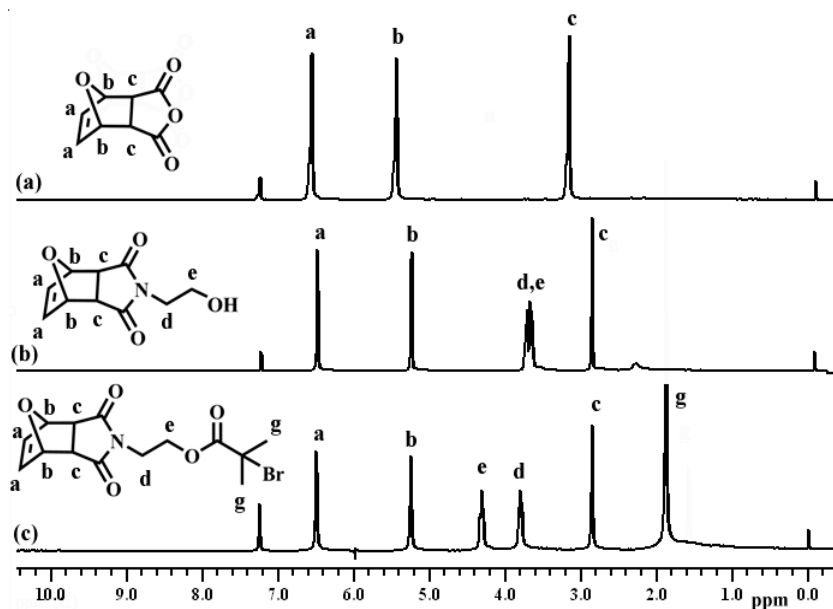
Figure S5. ^{1}H NMR spectrum of protected-maleimide functional ATRP initiator in CDCl$_3$.
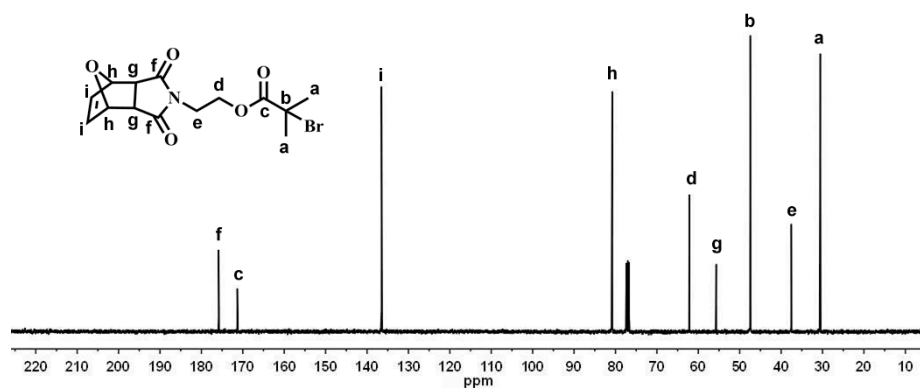

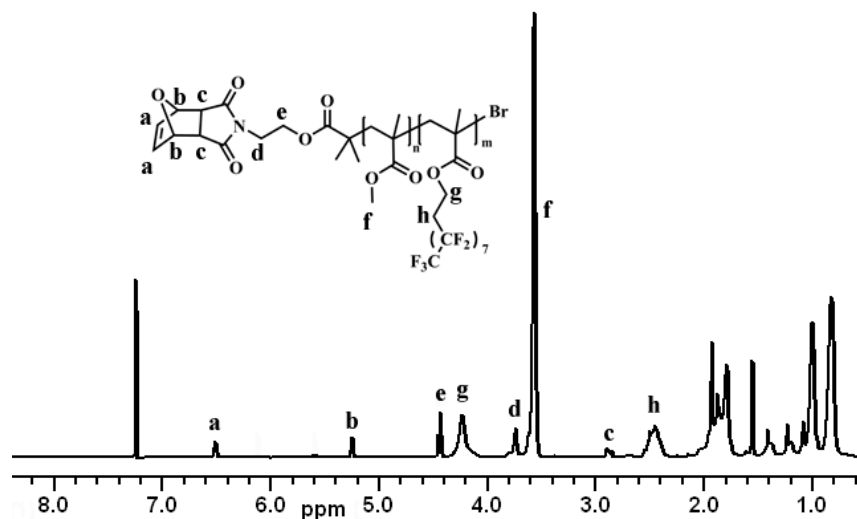**Figure S6.** ^{13}C NMR spectrum of protected-maleimide functional ATRP initiator in CDCl$_3$.

Figure S7. ^{1}H NMR spectrum of protected maleimide functional P(HDFMA-*co*-MMA) in CDCl$_3$.
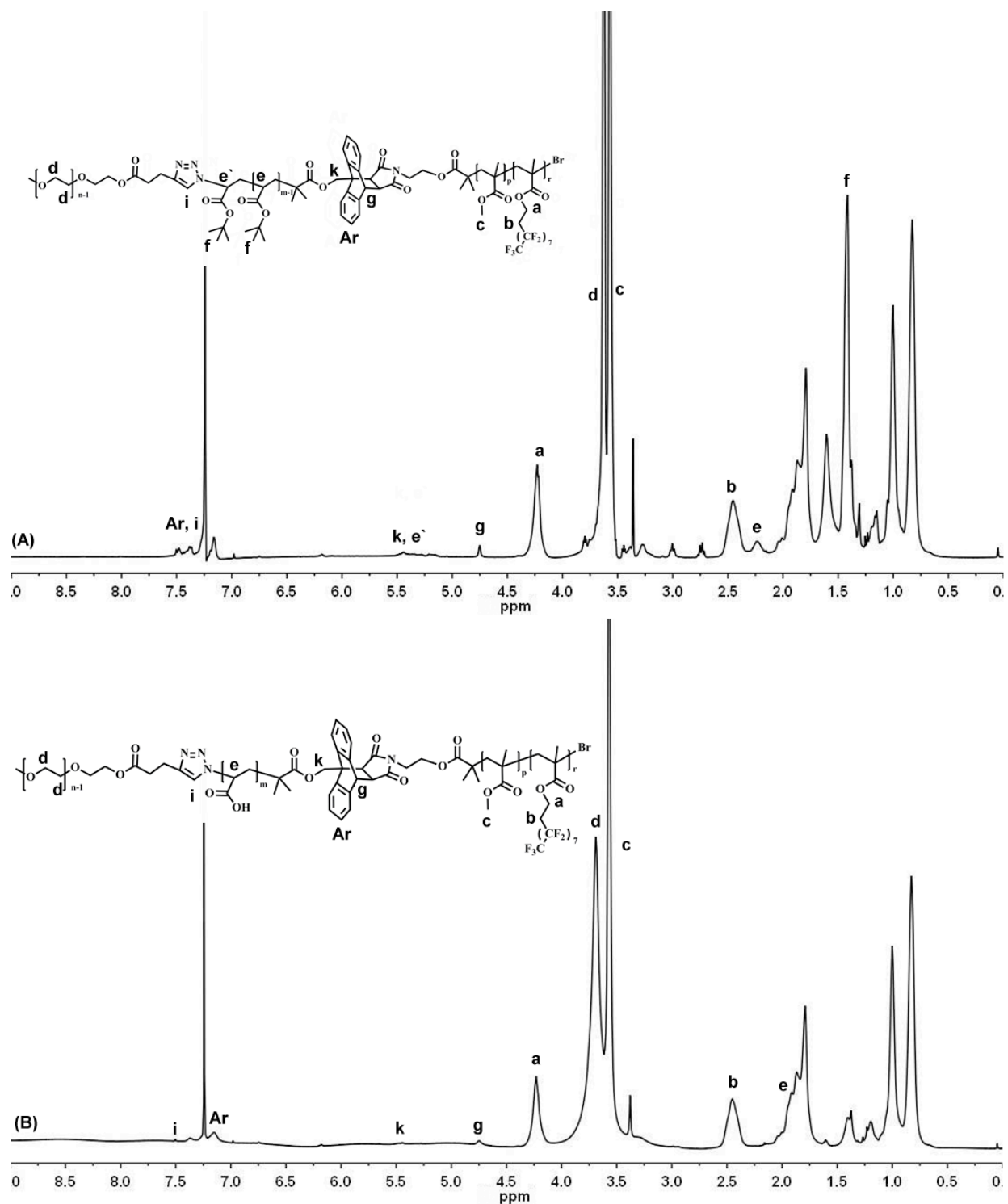
Figure S8. ^{1}H NMR spectrum of PEG-*b*-P*t*BA-*b*-P(HDFMA-*co*-MMA) (A) and PEG-*b*-PAA-*b*-P(HDFMA-*co*-MMA) (B) block copolymer (ABC-1) in CDCl$_3$.